To The Graduate Council:

I am submitting herewith a thesis written by Timothy E. McKnight entitled "An Improved Determination of Calibration Gas Corrections for a Typical Thermal Mass Flowmeter Design." I have examined the final copy of this thesis for form and content and recommend that it be accepted in partial fulfillment of the requirements for the degree of Master of Science, with a major in Engineering Science.

Joe Iannelli

J. Iannelli, Major Professor

We have read this thesis
and recommend its acceptance.

V. Tmi

A Baker

Majid Keyhani

Accepted for the Council:

C W Minkel

Associate Vice Chancellor and
Dean of The Graduate School

AN IMPROVED DETERMINATION OF CALIBRATION GAS CORRECTIONS FOR A TYPICAL THERMAL MASS FLOWMETER DESIGN

A Thesis
Presented for the
Master of Science Degree
The University of Tennessee, Knoxville

Timothy E. McKnight

August 1996

ACKNOWLEDGEMENTS

The author would like to express his appreciation to his wonderful wife for her support and patience during the development of this work. Also greatly appreciated are his parents, for their support, kindness, and assistance throughout his life. Many thanks to Dr. Joe Iannelli for the many hours of assistance, and for helping overcome all those hurdles. Thanks also to Dr. Protopopescu, for always having a moment to sit down and discuss things. Thanks to Jim Hardy and Jim Hylton for being there for all the questions. Thanks to David Holcomb for prodding me into activity. John Olin is much appreciated for his support and information regarding the specimens of this study.

ABSTRACT

The mass flow controller, or MFC, is a thermal flow device used extensively for the measurement and control of hazardous and corrosive process gases in the semiconductor industry. Calibration of the mass flow meter is conventionally performed using benign, non-hazardous surrogate gases, such as nitrogen, with correction of the calibration data to actual process gas indications by the use of linear correction factors. This conventional method is responsible for significant errors in the process gas measurement and control in the MFC's.

This project, which focuses on the mass flow meter (MFM) component of the MFC, was undertaken to develop a better understanding of gas correction factors of the MFM, which are actually not constant but *functions* dependent on the total flowrate of gas through the MFM. A finite element and analytical model was developed for a specific MFM and used to help determine better gas corrections for both helium and argon. The results of this modeling led to identifying some of the sources of non-linear functional dependence of the correction factors. The methodology for using the model is outlined for further studies using actual toxic and corrosive process gases.

TABLE OF CONTENTS

LIST OF FIGURES

LIST OF TABLES

NOMENCLATURE

Symbol	Description
Ac	Cross sectional area
C1	Integration constant
C2	Integration constant
C_p	Specific heat of a gas at constant pressure
C_v	Specific heat of a gas at constant volume
D	Characteristic dimensional diameter
$e^{h/2}$	Numerical solution approximation error
Gr	Grashof Number
h_m	Minor head loss
K, or K-factor	Gas correction factor
k	Thermal conductivity
Kl	Minor loss coefficient
Kr_b	Annular bypass insert radius
L1	MFM outer housing length
l_a	Aft annulus length
l_e	Annular bypass insert length
l_s	Overall capillary length
l_{s1}	Upstream feed length in capillary sensor
l_{s2}	Upstream sensor length in capillary sensor
l_{s3}	Inter-sensor gap length in capillary sensor
l_{s4}	Downstream sensor length in capillary sensor
l_{s5}	Downstream feed length in capillary sensor
l_{se}	Length to sensor tap in capillary sensor

l_{sf}	Sensor feed length in capillary sensor
l	Sensor length in capillary sensor
$\dot{m}$	Mass flow rate
M	Meshing descriptor
Ma	Mach Number
MFC	Mass Flow Controller, a thermal mass flow measurement and control device
MFM	Mass Flow Meter, a thermal mass flow measuring device
N	Molecular geometry factor
NIST	The National Institute of Science and Technology
Nu	Nusselt Number
ORNL	The Oak Ridge National Laboratory
p	Pressure
Pr	Prandtl Number
psi	Pressure unit, pounds per square inch
ρ	Density
Q	Volumetric flow rate
Q1	Numerical solution value
ΔQ1	Change in numerical solution value with refined meshing
q	Heat flux
$\vec{q}$	Heat flux vector
r	Radius
$\vec{r}$	Radial coordinate vector
r_b	Annular bypass outer radius
r_s	Capillary sensor tube inner radius
Re	Reynolds Number
RTD	Resistance Temperature Device, i.e. Platinum, Nickel

sccm, or SCCM	Flow unit, Standard Cubic Centimeters per Minute
slpm, or SLPM	Flow unit, Standard Liters Per Minute
SEMATECH	The Semiconductor Manufacturer's Consortium
ΔT	Temperature change
T_{exact}	Approximate numerical solution after error correction
$\bar{\bar{\tau}}$	Stress tensor
$\vec{\Theta}$	Angular coordinate vector
U	Free stream velocity
u_W	Wall slip velocity
μ	Absolute viscosity
V	Mean fluid velocity
$\vec{v}$	Velocity vector
VCR	A common vacuum connector fitting style
v_r	Radial velocity
v_θ	Angular velocity
v_z	Axial velocity
W1	MFM outer housing width
$\bar{z}$	Axial coordinate vector

1. INTRODUCTION

1.1 BACKGROUND

In 1993, researchers at the Oak Ridge National Laboratory, or ORNL, became involved with SEMATECH, the Semiconductor Manufacturer's Consortium, and NIST, the National Institute of Science and Technology, in an effort to improve the productivity of the domestic semiconductor industry. The formation of this collaboration was in response to the semiconductor community's request to advance the design and development of a single, yet fundamental, component of its manufacturing process. This component was the thermal mass flow controller, or MFC.

The MFC is a closed-loop flow metering device which typically measures and controls the rate of a flowstream by monitoring flow-dependent thermal transfer effects and adjusting a downstream proportional valve. With over twenty different manufacturers of the MFC in the United States alone, many variations of this thermal measurement device exist. The underlying principle in each of these variations is the sensing of flow rate by injecting heat into the flowstream and measuring the temperature change of the fluid caused by the heat input.

Although used for a wide variety of flow control applications, the MFC has become the method of choice for monitoring and controlling gas delivery in semiconductor fabrication processes. Its success within this market is evidenced by the fact that over 75% of all semiconductor fabrication process tools contain MFC's[1]. Perhaps due in part to its pervasive position within the semiconductor community, but also certainly due to the subtle complexities of its design, the MFC has recently been scrutinized for its impacts upon semiconductor manufacturing. In 1991, an industry-wide survey throughout the semiconductor community identified the MFC as the single greatest equipment problem facing fabrication process operators[2]. This finding prompted SEMATECH, a consortium of semiconductor manufacturers, and SEMI-SEMATECH, the semiconductor equipment manufacturers, to create an MFC testing, evaluation, and development program. Towards this end, a mass flow controller testing and development facility was created at ORNL. The goal of this facility was to develop and implement a set of standardized test methods which would allow the MFC to be fully evaluated and further developed to improve its performance.

A significant portion of the SEMATECH mass flow controller development program pertains to the issue of MFC accuracy and calibration. As flow metering devices, MFC's are responsible for the control of many crucial flow steps during the semiconductor fabrication process. Accuracy of the flowrate, and the ability of the MFC to repeatably perform the administration of this flowrate, are paramount. Failure to correctly perform a single task step can result in the failure of an entire wafer, comprised of several hundred chips and valued at thousands to hundreds of thousands of dollars. Typically, the inaccuracy of MFC's are specified by manufacturers to be 1% of full scale, with full scale flow ranging from 10 standard cubic centimeters per minute, or sccm, to several liters per minute. Preliminary work at the ORNL, conducted by the author, has demonstrated that, oftentimes, mass flow controllers do not achieve the accuracy specifications which their manufacturers quote. This is particularly true when an MFC has undergone a "surrogate gas calibration" in which the MFC is calibrated on a surrogate, benign gas instead of the actual nameplate gas for which the MFC is to be used. Surrogate gas calibrations are often employed when it is uneconomical or administratively unfeasible to perform a potentially hazardous calibration with toxic and corrosive nameplate gases. Instead, a benign, surrogate gas, which has properties similar to the intended gas, is used, and a multiplicative "gas factor" is employed to correct the benign calibration for actual process gas flow indications. MFC operation manuals typically feature several pages which list gases, the corresponding "surrogate" gas which may be used for calibration, and the respective multiplicative factor which must be employed to correct the measurement. ORNL and SEMATECH have demonstrated that flow measurement errors of typically 10%, but perhaps as large as 40%, can result from surrogate gas factor use.

1.2 STATEMENT OF THE PROBLEM

In the past, mass flow controller accuracy has only been given minor importance due, in part, to a tendency within the semiconductor industry to employ cookbook "tweak it 'til it works" process control methods. In this scenario, the important specification of a flow controller is its *repeatability*, not *accuracy*. If the process is adjusted until acceptable performance is reached, it is only required that the flow controller continue to perform consistently. However, there are problems associated with this philosophy. Most notable are the obvious problems of MFC replacement in the event of failure. If the replaced MFC does not match the flow performance of its replacer, the process will need costly readjustment and may not ever guarantee similar performances.

The current mode of thought within the semiconductor industry is that MFC accuracy is becoming more important. Cookbook process control is being replaced by highly engineered fabrication beds where the exact amount of necessary gas flow has been calculated and must be supplied accurately. In this emerging era, surrogate gas calibration correction factors, with associated accuracy errors orders of magnitude greater than the specifications of the flow devices themselves, can not be tolerated. MFC calibrations must either be done on the actual process gases, or the correction factors must be re-evaluated to decrease the inaccuracy they impart to the measurement. As the former solution is still impractical both economically and administratively, it is the intent of this thesis to address the latter.

1.3 OBJECTIVES OF THE STUDY

The ultimate intent of this thesis is to develop a better understanding of surrogate gas corrections in order to decrease the amount of inaccuracy their use imparts to the measurement of gas flows. Towards this end, this thesis has addressed the fluid dynamics involved within the elements of a thermal mass flow meter and the associated continuity, momentum, and energy equations that the fluid dynamics satisfy. As a tool towards a better understanding of calibration factors, an existing numerical modeling program has been employed to simulate the thermal hydrodynamic phenomena which occur within the mass flow controller. As opposed to conventional calibration *factors*, the numerical model was used to help predict the actual correction *functions* which must be employed when calibrating and using these flowmeters on different gases. Successful implementation of higher accuracy calibration *functions* will enable the semiconductor industry to continue performing lower cost surrogate gas calibrations on its mass flowmeters without the associated loss of accuracy which it currently must accept in using conventional calibration factors.

The methodology employed within this study to develop a better understanding of surrogate gas calibration corrections has been developed as follows:

- Perform a literature survey to understand the current level of understanding of the problem within the industrial and scientific community (Chapter 2).
- Obtain multiple copies of a single make and model MFC. Accurately measure the characteristics of these MFC's, including flow path geometry, heat input, and material makeup (Chapter 3).
- Develop appropriate forms of the equations of continuity, momentum, and energy for the thermal and hydrodynamic phenomena occurring within the MFC's (Chapter 4).
- Develop a numerical model of the thermal hydrodynamics of the MFC's using an existing finite element package as a research tool (Chapter 5).

- Validate the numerical model by actual calibration of the sample MFC's on a variety of gases (Chapter 6).
- Discussion of findings (Chapter 7).
- Conclusions and recommendations (Chapter 8).

1.4 LIMITATIONS

This thesis will focus on a specific make and model of MFC, the thermal- and hydro-dynamics of that MFC, and the relationships between gas properties and that MFC. MFC designs are all very similar in nature, however, each design features its own geometries and other individual characteristics. It should be realized that this study is focused on obtaining a better understanding of gas calibration functions from the viewpoint of a single, unique model of MFC. The results of this thesis are in no way intended to provide general calibration functionalities which might be used on any thermal mass flow controller. It is hoped, however, that the techniques employed within this thesis may indeed be employed to better understand the critical issues involved with surrogate gas calibration functionalities such that similar efforts may be undertaken for other MFC's with characteristics which differ from the specimens of this study.

2. LITERATURE REVIEW

A vast array of publications focus on the use of thermal mass flow controllers, specifically in their use within the semiconductor industry. Most manufacturers' operating manuals provide a good overview of the basic principles involved in thermal mass flow measurements and until the early '90s, the majority of trade literature available regarding the MFC also focused on these basic principles. By this time, the MFC had established itself as the flow measurement method of choice within the semiconductor community. The technique was fairly simple, and, due to a limited number of moving parts, fairly suited to the corrosive environment of semiconductor fabrication. Basically, thermal mass flow controllers operate by detecting the flow dependent transfer of thermal energy within a fluid stream. Figure 2-1 represents a typical MFC diagram which might be found in most MFC operating manuals. In this diagram, the flow sensor portion of the MFC is illustrated as a small flowpath which runs parallel to what is often referred to as a laminar bypass. Typically, this flow sensor is instrumented with two electrical resistance heaters in the form of two fine wire wraps. A constant current is used to power the two resistive elements, and heat is conducted through the sensor tubing and into the flow stream. Under zero flow conditions, a symmetrical thermal profile is developed within the capillary tubing, with the maximum temperature occurring at the midpoint between the two heaters. Under increasing flowrate conditions, convection skews this profile, causing the maximum temperature point to be located somewhere downstream of the midpoint between the heaters. The magnitude of this skewing is dependent on the flowrate, and may be measured by evaluating the overall temperature difference sensed between the upstream and downstream heaters, which also serve in dual agency as resistance thermometer elements. The temperature difference experienced by the fluid resulting from the amount of heat transferred is dependent on the thermal properties of the media and the mass flowrate of the fluid, and is generalized by

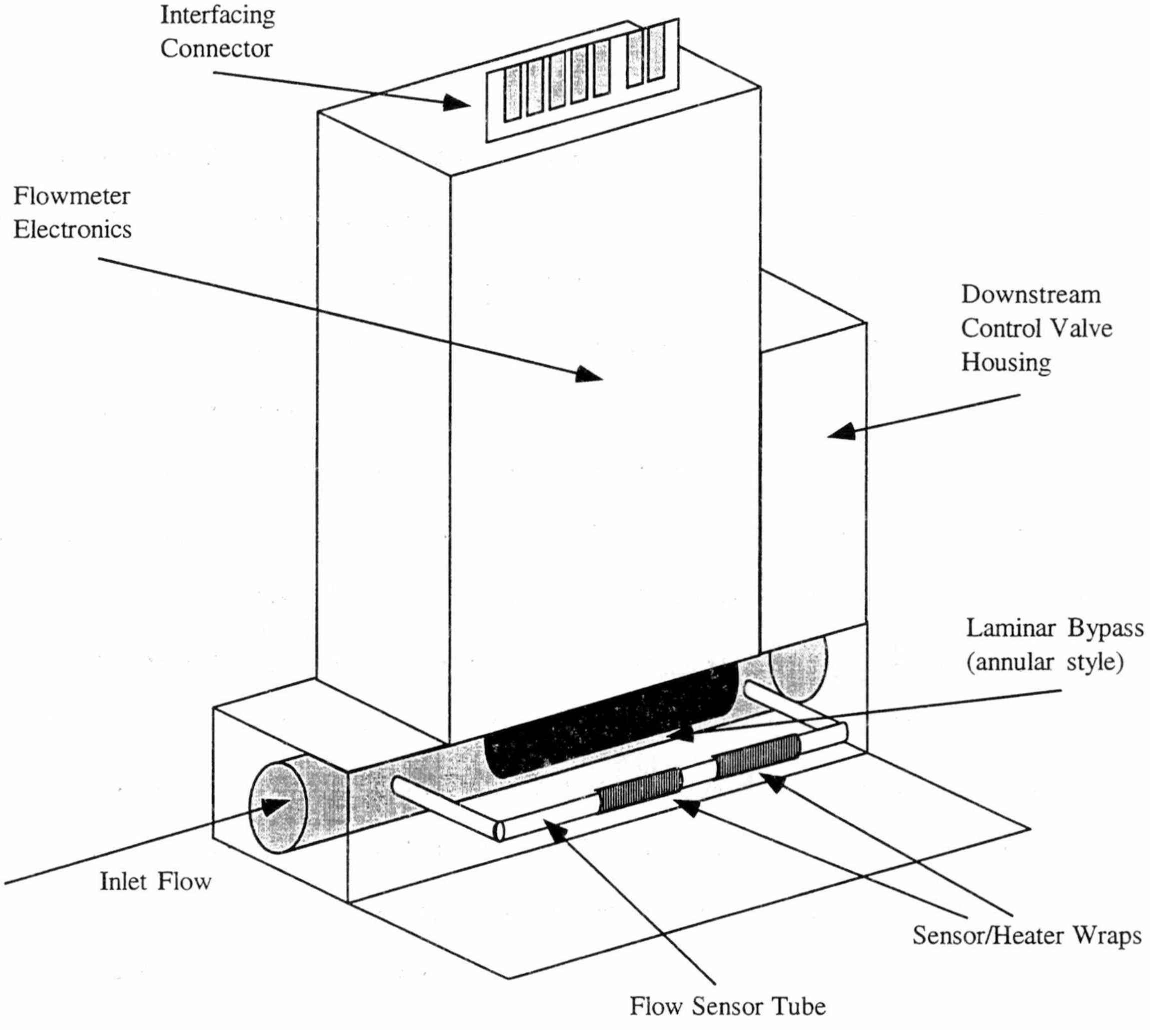

Figure 2-1. The Mass Flow Controller.

$$q = \dot{m}C_p\Delta T$$ **Equation 2.1**

In this expression, the ΔT indicates the temperature difference of the fluid between the unheated inlet condition, and the heated condition downstream of the heat input. This relationship is the basis for the flowrate dependent skewing of the thermal profile by convection. This thermal skewing, however, is often measured by observing not the temperature gain of the fluid at each heater, but rather the temperature difference between the two heaters.

Over a limited range of flows, the change in temperature between the upstream and downstream elements will linearly correlate with the flowrate of the fluid. However, the relationship is not inherently linear over a wide range of flows. Within the linear range of the device, the temperature difference between the upstream and downstream heating/sensor elements will increase with flowrate as the temperature profile becomes more and more skewed downstream. Eventually, however, the difference in temperature between the two reaches a maximum and additional flow actually reduces the temperature difference. In the limit as the flowrate increases to infinity, the temperature difference between the sensors will reduce back to the no-flow condition of zero difference. The general relationship between mass flowrate and temperature change may be summarized graphically as in Figure 2-2.

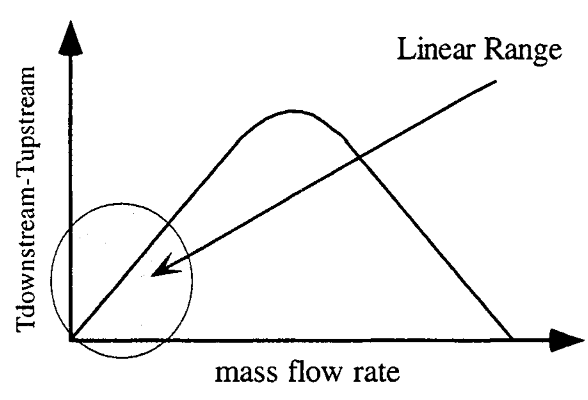

Figure 2-2. Temperature Difference Dependence on Flow Rate in a Mass Flow Controller.

Realizing the potential for inaccuracy, manufacturers carefully dimension the sensor geometry of their MFC's for specific gases at specific flowrates, so that the device will work within the linear operating regime for these conditions[3]. For most MFC designs, the sensor flowrate limitation is approximately 100 sccm[4]. To accommodate a larger range of flows and still maintain linearity within the sensor flowpath, laminar bypass elements are employed in parallel with the sensor tubing. In this configuration, the total flowrate through the device is the combined flowrates through the sensor and bypass portions. By maintaining laminar flow within each portion, the total flow through the device can be inferred by only measuring the flow through the sensor path and by assuming a Reynolds-number independent split ratio between the sensor and bypass flows. In operation, the laminar bypass element actually provides the major portion of the overall flow through the device, with typically less than 1% of the overall flow passing through the sensing element[3].

Manufacturers specify the accuracy of a thermal mass flow meter by indicating the non-linearity of the indication of flowrate for the device over its intended flow range. Most MFC's available on the market today are specified with accuracies of 1% of full scale. For example, a "1% of full scale" accuracy specification indicates that a 1000 sccm nitrogen MFC should be relied upon to deliver a desired flowrate of nitrogen with deviation from the intended flow not to exceed ±10 sccm. Obviously, the geometry and configuration of each individual MFC is going to be slightly different, and each MFC must be calibrated to meet this 1% specification for the gas with which it will be used. Usually, MFC's are calibrated to this specification by the manufacturer prior to delivery. Calibration methods are diverse, with each method having its own advantages and disadvantages. Perhaps the most common calibration setup is a standard *volume chamber*, also called a *piston-rate-of-rise assembly*. This technique employs a known variable volume, often in the form of a glass cylinder with a movable, mercury-sealed piston, into which a steady-state flow is collected. The volumetric flow rate is obtained by measuring the total volume of gas collected over a given time period, or by measuring the rate of change of the volume under the moving piston and thus the "piston-rate-of-rise". Corrections are made to standardize the volumetric flow to standardized, or conventionally accepted, conditions of pressure and temperature, and the result is compared to the MFC flow indication. In the event of discrepancy, electronic adjustments within the MFC may be made to correct the MFC to the standardized flow. Further, several adjustments over the intended flow range are typically provided to correct for some non-linearity of the MFC throughout its range. With appropriate use of standards, and by making enough adjustments to the device under test, an MFC can usually be corrected to meet manufacturer's accuracy specifications with the specific gas used for calibration.

Unfortunately, it is seldom economically or administratively feasible to calibrate a set of MFC's on the actual hazardous process gases for which they will be used. Such a calibration would entail costly gas handling equipment and costly safety precautions. Further, traditional calibration equipment capable of handling toxic and corrosive gases are often time consuming and difficult to use. For these reasons, the semiconductor community has relied heavily on surrogate gas calibrations, and the associated use of calibration gas correction factors.

Surrogate gas calibrations and surrogate gas correction factors are employed whenever it is not feasible or desirable to calibrate an MFC with the gas for which that MFC will actually be used, i.e. the nameplate gas. Such a calibration may be used when a corrosive, toxic, or flammable gas creates safety hazards which make the actual nameplate gas calibration costly and dangerous. Surrogate gas calibrations may also be employed when the actual nameplate gas *itself* is too costly to expend for a calibration, and when another, less costly gas may be chosen instead. As an accepted technique within the semiconductor community, most MFC operating manuals contain a section devoted entirely to the use of surrogate gas calibrations and the correction factors which must be applied. Traditional approaches to surrogate gas calibrations attempt to match gases with very similar thermodynamic properties, and to base the correction factors on ratios of these properties between the surrogate and actual nameplate gas. Taking the simplified bulk fluid relationship of heat transport with mass flowrate, Equation 2.1, and substituting in the volumetric flowrate, Q, for the mass flowrate, where

$$Q = \frac{\dot{m}}{\rho}$$ **Equation 2.2**

results in an expression for the volumetric flowrate as

$$Q = \frac{q}{\rho C_p \Delta T}$$ **Equation 2.3**

An expression may then be constructed to indicate the ratio of flowrates between two gases with different properties. Using subscript 1 to denote the actual gas of use, and subscript 2 to indicate the surrogate calibration gas, this expression becomes

$$\frac{Q_1}{Q_2} = \frac{\left[\dfrac{q}{\rho_1 C_{p_1} \Delta T}\right]}{\left[\dfrac{q}{\rho_2 C_{p_2} \Delta T}\right]}$$ **Equation 2.4**

In Equation 2.4, the subscripts on the heat input and the temperature difference have intentionally been left off to indicate operation of the MFC where, for a given heat input, q, the MFC sees a temperature difference of ΔT. For this temperature difference, the calibrated flow of gas 2 is Q_2. However, for the same temperature difference, and thus the same flow indication from the MFC, the actual flow of gas 1 is Q_1. Thus, the heat input term and temperature difference term may both be dropped, and the equation becomes,

$$\frac{Q_1}{Q_2} = \left[\frac{\rho_2 C_{p_2}}{\rho_1 C_{p_1}}\right]$$ **Equation 2.5**

This equation gives a fluid property-based multiplicative factor for correcting the MFC indication for the flow of gas 1 when the MFC has been calibrated with gas 2. Often, this equation will be adjusted by the addition of molecular geometry dependent factors, N, which take on different values for the number of atoms in a gas molecule,

$$\frac{Q_1}{Q_2} = \left[\frac{\rho_2 C_{p_2}}{\rho_1 C_{p_1}}\right]\left[\frac{N_1}{N_2}\right]$$ **Equation 2.6**

The values of N are 1.040 for a monatomic gas, 1.000 for a diatomic, 0.941 for a triatomic, and 0.880 for a polyatomic molecular geometry[5].

To simplify the use of correction factors, manufacturers lump the different physical parameters into an overall calibration factor, which is denoted K, and is assumed to be temperature independent.

$$K = \frac{N}{\rho C_p}$$ **Equation 2.7**

To measure a flow using this K factor, one simply employs Equation 2.6 with the appropriate K factors employed. An example from the Sierra Operating Manual reads[5] if the K factor for carbon dioxide is 0.74, and the K factor for nitrogen is 1.000; a full scale indication of 1000 sccm on an MFC calibrated on nitrogen but metering carbon dioxide would be equivalent to a flow of

$$Q_{CO_2} = Q_{N_2} \frac{K_{CO_2}}{K_{N_2}} = (1000sccm)\frac{0.74}{1.000} = 740sccm$$ **Equation 2.8**

For most gases, the experimental final factor is known to deviate significantly from the theoretical value. Therefore, when possible, the K-factor is determined experimentally for different gases for each model of MFC. Unfortunately, however, just as the calibration of MFC's with hazardous gases is typically impractical, so is the determination of calibration factors for these hazardous gases. Thus, manufacturers will compile a list of calibration factors, as best as they are known, for each gas which an MFC might meter, and include this list in the operating manual of each MFC. Some manufacturers freely admit that the use of these calibration factors should not be relied upon for accuracies better than 10% of full scale flow[5].

Realizing that surrogate gas calibration correction factors might be imparting significant inaccuracies to crucial semiconductor fabrication processes, the SEMATECH Technology Transfer Office published a report in 1991 on the non-linear behavior of mass flow controllers in the semiconductor fabrication arena of the diffusion furnace[6]. One of the first publications delving into the specific problems of MFC accuracy identified possible causes for the non-linear response of MFC's *in process* and identified surrogate gas calibration factors as potential deadfalls. Several different models of MFC's, from three major MFC vendors, were evaluated for response to dichlorosilane, a common non-ideal process gas. Indirectly measuring gas flowrate by monitoring furnace pressure, this study indicated that several of the test MFC's performed non-linearly for flowrates greater than 50% of full scale flow. Follow up work, conducted in the SEMATECH calibration laboratory, indicated similar non-linear behavior for these instruments using the gases R-12 and CF_4. These gases are typically employed as safe calibration substitutes for the hazardous dichlorosilane. Unlike their corrosive counterpart, both these gases may be evaluated using laboratory calibration standards, such as gas flow volume chambers, laminar flow elements, or pressure-rate-of-rise tests. However, non-linear deviations as great as 24.81% were observed for Freon-12, and 6.56% for CF_4, making them appear to be poor calibration substitutes for dichlorosilane. A most significant finding in these reports was that these errors were not scalar offsets from expected values, but were functionally dependent on flowrate. Thus, multiplicative calibration correction *factors* could not be relied upon to correct flowrate indications. In order to improve accuracy, calibration *functionalities,* dependent on flowrate, would have to be employed.

In a paper published in 1991, Dr. Luke Hinkle of MKS Instruments, a prominent MFC manufacturer, offered an explanation to the nonlinear behavior of MFC's[4]. Dr. Hinkle's article attributes the nonlinear behavior of MFC's to either of two sources; variation with flowrate of the flow splitting ratio between the sensor and the bypass, or non-linear behavior within the sensor tube itself. With the former, the sizing of the laminar/bypass geometries may be appropriate for nitrogen such that each path remains laminar and splitting between the paths is constant; however, for gases with significantly different properties, the flow in one or both the paths may deviate from the laminar regime, with flowrate-dependent splitting resulting. This becomes even more likely with an MFC which has been sized for a lower density gas such as nitrogen, but is used at higher flowrates with some of the higher density gases which are employed by the semiconductor community, i.e. tungsten hexafluoride. Non-linearity due to this variable flow splitting between the sensor and bypass paths may have indeed been a common source of error in the early days of MFC manufacture and use. However, as evidenced by current manufacturer manuals, much effort has been expended in recent years to develop better designed flowpaths such that the flow remains well within the laminar regime. Indeed, for most MFC geometries, fairly reliable approximate analytical solutions may be readily obtained to ensure the flow regime in which an MFC is working and to ensure that constant flow splitting is maintained. Thus, although variable flow splitting may indeed be a source of non-linearity within an MFC, it is more likely today that Dr. Hinkle's latter explanation, non-linearity in the sensor tube measurement itself, is often the major cause of gas correction non-linearity.

In further explanation of sensor tube measurement non-linearity, Dr. Hinkle considers helium gas. In many MFC's, helium gas presents significant flow non-linearity when referenced to nitrogen. Dr. Hinkle attributes this non-linearity to helium's high thermal diffusivity. Returning Figure 2-1, one can realize the significance thermal diffusivity would play in an MFC flow measurement. With a high thermal diffusivity, helium would conduct heat from the heated walls into the core of the fluid stream much faster than gases with lower thermal diffusivity, such as nitrogen. It is quite likely that this effect, combined with dependence on fluid velocity, would significantly impact the flow/temperature difference relationship upon which the measurement depends.

In follow up work pursuing this problem, Dr. Hinkle employed a numerical model of the MFC sensor tube to attempt to simulate the thermal hydrodynamics of this flowpath[7]. With this model, Dr. Hinkle was able to simulate very accurately the non-linear behavior of helium referenced to nitrogen. This preliminary work suggests that useful numerical models might indeed be employed to develop better functional surrogate gas correction factors, regardless of the gas, based on the geometry and design of an MFC and the properties of the gases involved. With this validation, this thesis has continued to pursue numerical methods to attempt to understand, and possibly predict, functional gas correction factors for a wider sampling of gases.

3. OVERVIEW OF TEST SPECIMENS

In developing a numerical simulation of the MFC, it is initially desirable to limit the scope of the test domain in order that a realistic endeavor regarding simulation and subsequent validation may be performed. If successful simulation, and a resultant reduction of inaccuracy due to the use of improved calibration functionalities, may be achieved on an initially limited scope, future work may implement the same methodology over a much wider domain. With over 20 manufacturers within the United States alone, the individual designs of MFC models vary considerably and represent a diverse domain. Fundamentally, however, the principles behind these designs, as discussed in the previous chapter, remain consistent. Therefore, successful numerical modeling on one particular MFC should provide an excellent framework for which other MFC's, with slightly varying designs, may also be evaluated.

Three mass flow meters from the California based Sierra Instruments, Inc. were chosen as the specimens of study for this thesis. A sample is represented in Figure 3-1. The selection of this brand by the author was made solely on the basis of availability and convenience, and in no way reflects endorsement nor preference for this brand on the part of the author.

The three mass flow meters chosen for this study represent a sampling of the Sierra model 830D-L-7-V1-OK, and are classic examples of the two path sensor and bypass thermal mass flow meter. It should be indicated that these instruments are not mass flow controllers, but thermal mass flow meters, which are unable to *control* process flow but *measure* the flow in the same manner as a mass flow controller. Indeed the only difference between a mass flow meter, and a mass flow controller, is that a controller utilizes the flow signal to control a downstream proportional valve which meters a desired flowrate. A mass flow meter merely indicates the measured flow, and does not host a downstream valve. The choice of using mass flow meters, as opposed to controllers, was made on the basis of availability. Nonetheless, one intent of this study, based on Dr. Hinkle's previous work, is to investigate the non-linearity of the sensor measurement

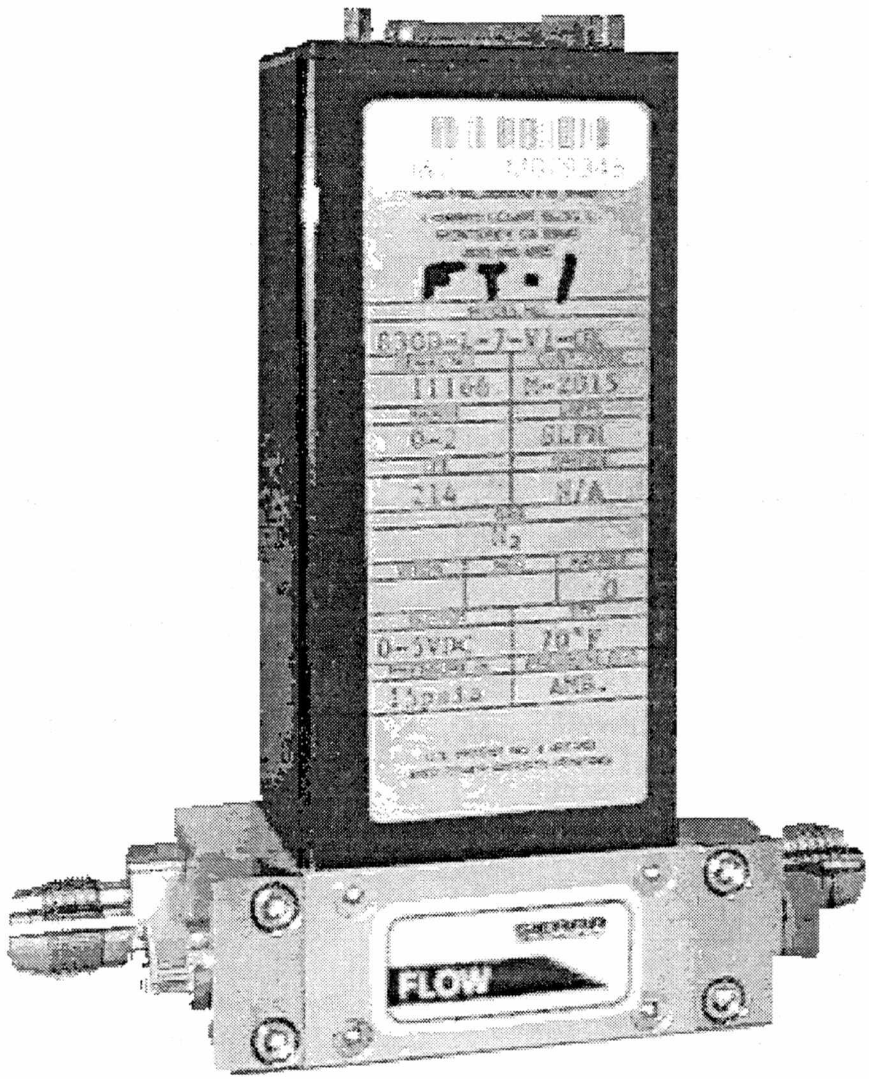

Figure 3-1. The Sierra Model 830D-L-7-V1-OK Thermal Mass Flow Meter.

itself. Decoupling the flow control from the overall measurement system is actually advantageous in order to isolate the actual thermo-hydrodynamics of the sensor measurement

The model 830D-L-7-V1-OK is a classic example of the two-path, sensor/bypass thermal mass flow meter. The laminar bypass is employed to handle a total flow span of 2 standard liters per minute of nitrogen, or 2000 sccm, while maintaining linear measurement dynamics within the sensor portion. The laminar bypass element is configured as a tubular annulus, with very little clearance between the inner and outer walls. In parallel with this bypass, in the same horizontal plane, is the sensor path. The two flowpaths are commonly connected to one another in large plenum areas upstream and downstream of the annular bypass, as indicated in Figure 3-2.

The sensor path is constructed of a capillary stainless steel tube, about which upstream and downstream heating elements/RTDs are wrapped. A constant current source drives these heating elements, generating heat fairly uniformly over the outer surface of the capillary sensor tubing. The sensor tube and heater wires are accessible for maintenance in an open region on the front face of the MFC. In operation,

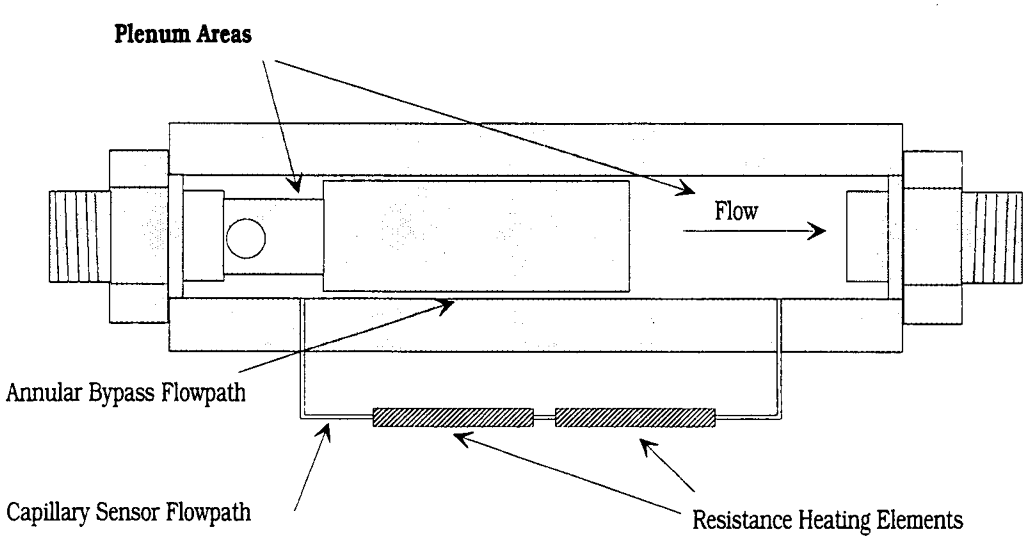

Figure 3-2. Plenum Detail of Horizontal Cross Sectional Area of Flowpaths.

this region is sealed off, and an insulative blanket sandwiches the capillary tube and its heating elements to minimize radiative and free convection cooling of the generated heat, Figure 3-3

Similar to the sensor, the bypass annulus is also constructed of 316 stainless steel. Unlike the sensor tubing, which is surrounded by free space and an insulative blanket, both the annular insert and surrounding outer annulus represent significant thermal bulk to the bypass flow, as indicated in Figure 3-4.

Gas fittings into and out of the meter are 1/4" VCR, a vacuum style fitting which employs a soft metal deformable gasket to create high integrity seals. Internal gas seals are constructed of Kalrez "O" rings. Processing electronics are located locally on a printed circuit board which resides above the flow paths inside the instrument. These electronics control the constant current heating source, and linearize the upstream and downstream temperature difference to an equivalent 0-5 volt flow indication level. A power supply and flow indication box is used in conjunction with the mass flow meter itself. This indication merely scales the 5-volt flow signal from the mass flow meter to a flow equivalent range of 0-2 SLPM.

Sierra Instruments specifies the accuracy of their thermal mass flow meters and controllers to ± 1.0% of full scale, or 20 sccm for this particular model[5]. The repeatability of the instrument is specified as ±0.2% of full scale, or 4 sccm. Pressure and temperature coefficients for variation of these parameters within the flowstream are indicated to be 0.1% of full scale per 1 psi, and 0.1% of full scale per 1 degree C. The response time is presented as the amount of time for the flow indication to stabilize to 2% of the steady state value and is indicated to be 1 second over the range of 25 to 100% of full scale. For flow rates less than 25% of full scale flow, the response time is assumed to be slower. The pressure drop across the instrument at full scale flow is specified to not exceed 0.08 psi, equivalent to 6 cm of water column.

Similar to most MFC manufacturers, Sierra Instruments provides details for the use of calibration factors when performing surrogate gas calibrations. The methodology employed by Sierra is

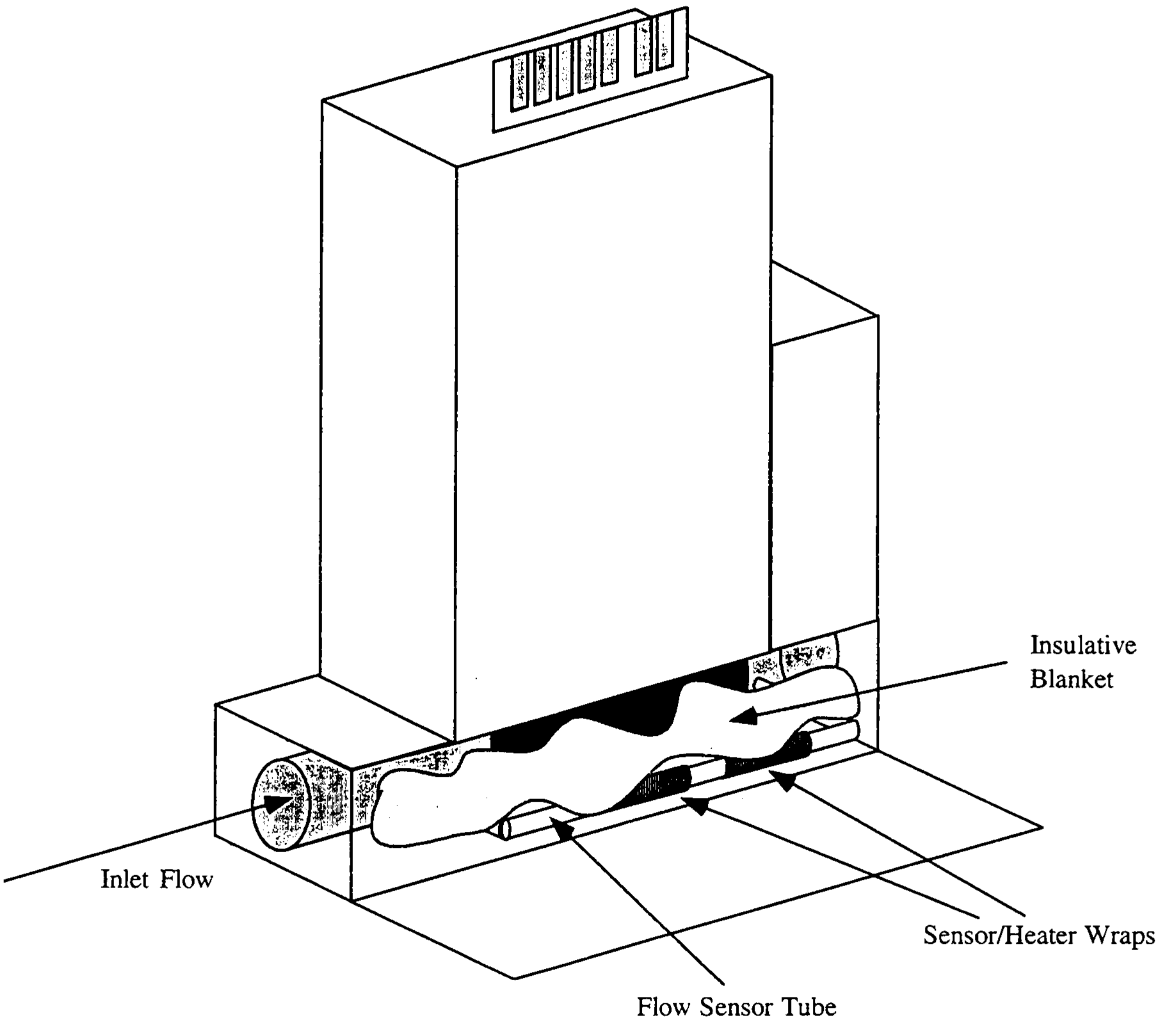

Figure 3-3. View of Sensor Access Area and Insulating Material.

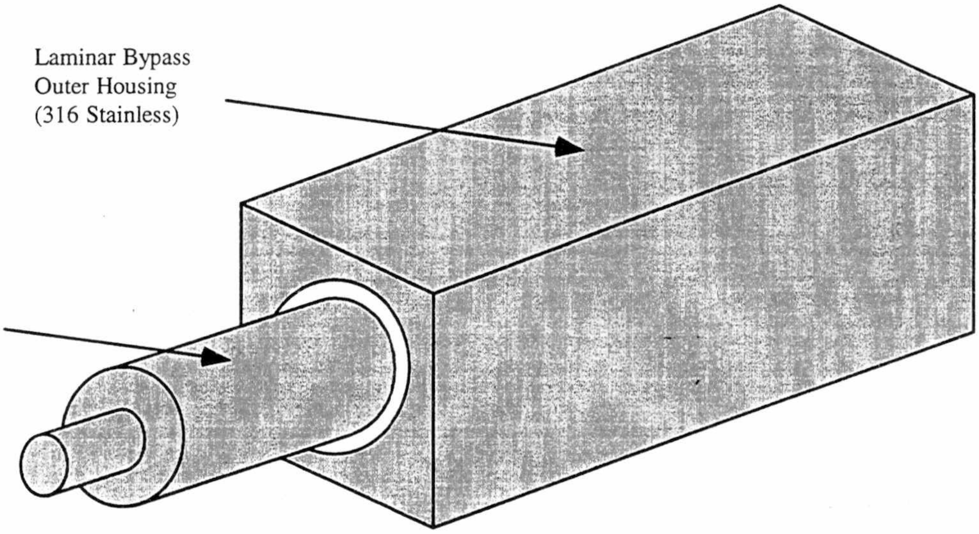

Figure 3-4. Bypass Annulus and Insert of Sierra Model 830D-L-7-V1-OK.

consistent with the surrogate gas K-factor derivation provided in Chapter 2. The manual supplied with Sierra Instruments MFC's provides several page listings of gases, references gases for which surrogate use is recommended, K-factors with respect to the reference gas, K-factors with respect to nitrogen, thermal heat capacities, and densities. The manual states that surrogate gas factors work better when gases of similar "families" are employed as surrogates, where *families* is taken to imply a group of gases with similar fluid properties. Sierra qualifies the use of surrogate gas factors, however, by clearly stating that their use should not be employed in any application which requires accuracies to better than ±10%[5].

The relevant manufacturer specifications for a Sierra Model 830D-L-7-V1-OK mass flow meter are summarized in Table 3-1.

In addition to tabulating manufacturer specifications, the geometry and essential parameters of the test specimens were carefully measured and tabulated for later use in first order analytical approximations, covered in Chapter 4, and the numerical modeling of Chapter 5. Figure 3-5 presents the housing detail of the annular bypass flowpath and the sensor flowpath. Corresponding to this figure, Table 3-2 tabulates the essential geometric details of these sections of the meter.

Figure 3-6 presents the annular insert detail of the annular bypass flowpath. Corresponding to this figure, Table 3-3 tabulates the vital geometric details of this section of the meter.

Figure 3-7 presents the capillary sensor tubing detail including heater dimensional layout. Corresponding to this figure, Table 3-4 tabulates the vital geometric details of this section of the meter. voltmeter in parallel with the sensor windings, and simultaneously measuring the current through and voltage across each sensor.

Surface temperatures were experimentally determined by placing thermistor thermometers on the outer surface of the MFM flowpath region. Thermal contact was enhanced using a thermally conductive paste between the thermistor and the stainless steel housing.

Inlet fluid temperatures were measured and determined to be consistent with prevailing ambient room temperatures due to significant gas piping lengths during which equilibration with the room temperature could be achieved.

Additional measurements were performed in order to obtain other essential parameters necessary for the accurate thermal hydrodynamic modeling of the mass flow meter. In addition to the dimensional

Table 3-1. Relevant Manufacturer Specifications for Sierra Model 830D-L-7-V1-OK MFM[5].

Description	*Value*
Flow Range	0-2 SLPM
Accuracy	±1.0% of full scale
Repeatability	±0.2% of full scale
Temperature coefficient	0.1% of full scale per 1°C
Pressure coefficient	0.1% of full scale per 1 psi
Response time	300 ms time constant
Pressure drop	0.08 psi differential max
Gas pressure	500 psi gauge max
Temperature range	5 to 50 °C, gas and ambient

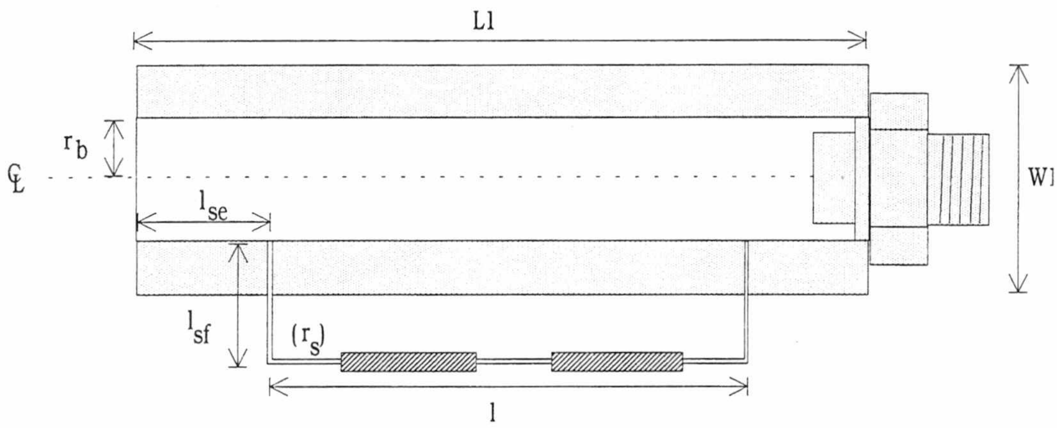

Figure 3-5. Dimensional Detail of Horizontal Cross Sectional Area of Bypass/Sensor.

Table 3-2. Bypass Housing/Sensor Tube Dimensional Summary.

Notation	*Description*	*Value (mm)*
L1	Outer Housing Length	76.16
W1	Outer Housing Width/Height	25.25
r_b	Annulus Outer Radius	6.35
r_s	Sensor Tube Inner Radius	.381
l_{se}	Length to Sensor Tap	12.5
l_{sf}	Sensor Feed Length	14.0
l	Sensor Length	63.18

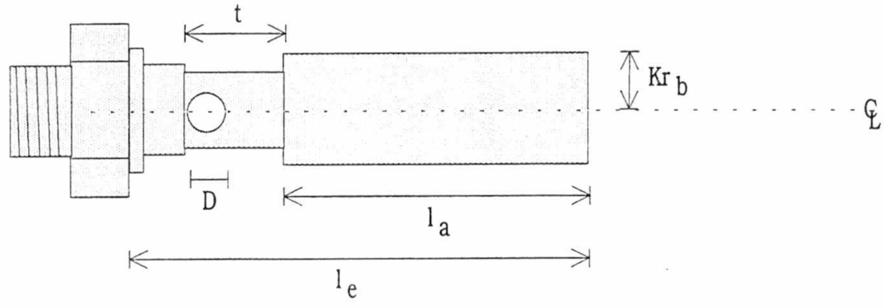

Figure 3-6. Dimensional Detail of Horizontal Cross Sectional Area of Bypass Insert.

Table 3-3. Bypass Insert Dimensional Summary.

Notation	*Description*	*Value (mm)*
t	Fore Annulus Length	10.5
l_a	Aft Annulus Length	32.00
l_e	Insert Element Length	48.75
D	Feed Hole Diameter	4.00
Kr_b	Annular Insert Radius	5.85

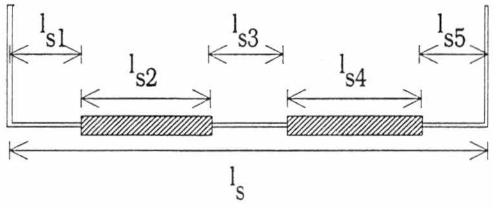

Figure 3-7. Dimensional Detail of Horizontal Cross Sectional Area of Capillary Sensor.

Table 3-4. Capillary Sensor Dimensional Summary.

Notation	*Description*	*Value (mm)*
l_s	Overall Capillary Length	63.18
l_{s1}	Upstream Feed Length	24.30
l_{s2}	Upstream Sensor Length	7.60
l_{s3}	Inter-Sensor Gap	.20
l_{s4}	Downstream Sensor Length	7.6
l_{s5}	Downstream Feed Length	23.48

information, it was required that an accurate knowledge of sensor heating power be obtained. This measurement was performed on each heater of each sensor by placing a current meter in series and a voltmeter in parallel with the element.

It was felt that an accurate measurement of the thermal conductivity of the insulative wrap around the sensors could not be obtained without significant error, due to the dependence of this quantity on the installation of the insulation. Removal of the insulation and subsequent measurement has a high likelihood of error due to compaction/expansion of the insulation during removal. Therefore, approximate thermal conductivity values were obtained from telephone conversations with John Olin, President of Sierra Instruments[3].

Table 3-5 presents a summary of additional necessary physical measurements which were performed on the Sierra Model 830D-L-7-V1-OK.

Table 3-5. Miscellaneous Attributes of MFM Specimen.

Description	*Value*
Inlet Fluid Temperature	293 K
Housing Surface Temperature	303 K
No-Flow Upstream Sensor Current	54.82 mA
No-Flow Upstream Sensor Voltage	3.24 V
No-Flow Downstream Sensor Current	54.82 mA
No-Flow Downstream Sensor Voltage	3.24 V
Sensor Power	0.1776 W
Insulation Thermal Conductivity	0.05 W/ms

4. GOVERNING THERMAL AND HYDRODYNAMIC PHENOMENA

4.1 PHYSICAL DESCRIPTION

Due to the existence of two separate and characteristically different flowpaths within an MFM, the physical thermal and hydrodynamic description of fluid flow through a thermal mass flow meter must be broken down into two separate situations; flow through the bypass and flow through the sensor. For each of these paths, extensive care is taken by manufacturers to ensure that the flow through each remains well within the laminar regime. This requirement is necessary to ensure that equal flow splitting is occurring between the two paths throughout the range of flows in which an MFM operates, such that the total flow through the device may be inferred from a single measurement within the sensor tube.

With the initial assumption that flow is indeed laminar, the flow condition within the annular bypass of a Sierra Model 830D-L-7-V1-OK thermal mass flowmeter may be described as laminar, compressible, viscous fluid flow with variable properties of density, viscosity, and thermal heat capacity dependent on temperature and pressure variations within the system. Under normal operation, the annular bypass temperature is several degrees Celsius above ambient, due to onboard electronics and inevitable losses from the higher temperature sensor region. Heat transfer between the fluid and boundaries of the annulus must be accounted for, as fluid temperatures entering the meter will seldom be equal to the temperature of the walls within the annulus. However, due to the large thermal bulk of the outer annulus walls, and the inner annular insert, this heat transfer will be governed by the assumption of an isothermal boundary with constant temperature. In addition to heat transfer, the flowpath within the bypass section of the meter presents significant abrupt transitions, therefore entrance and exit effects of the fluid to different spatial regions of the path must also be considered.

Flow through the capillary sensor flowpath may be described also as laminar, compressible, viscous fluid flow, with variable properties of density, viscosity, and thermal heat capacity dependent on temperature and pressure variations within the system. Again, heat transfer between the fluid and boundaries of the capillary wall must be accounted for as, again, incoming fluid temperatures into the meter will seldom match the temperature of the meter itself. More significantly, substantial amounts of energy are being introduced into the fluid stream within the capillary by the upstream and downstream sensor heater/RTDs. The heat transfer by the heaters may be evaluated as a variable heat source, based on a constant current source delivering an excitation to a temperature dependent resistance of the wire wrap heaters. Unlike the annular bypass, the condition of constant temperature at the boundary may not be assumed since the capillary tubing does not present itself as a significant thermal mass to this part of the system. Further, conductive heat transfer within the capillary walls away from the resistive heaters must be accounted for, as must inevitable conductive, perhaps free convective, and perhaps radiative losses which occur radially outward from the sensor heaters into the surrounding insulating blanket. In addition, similar to the restriction of the annular bypass, entrance, and exit effects of the fluid at the ends of the capillary sensor tube may also need accounted for.

The driving force creating fluid flow within the meter is a pressure gradient across the meter itself. An initial approximation of the magnitude of the pressure difference may be obtained from the manufacturer's specifications. Sierra Instruments specifies that this pressure drop will not exceed 0.08 psid across the meter[5]. As the sensor capillary tubing and annular bypass are situated in parallel to one another, with respect to the flow through the system, the only difference in total pressure drop through the annular bypass region and sensor tubing region will be due to entrance and exit losses. Further, as the geometry within these sections represents significantly more restriction to the flow than the plenum areas upstream and downstream of these sections, most of the total pressure drop within the system will occur within these restrictive sections.

It should be noted, at this point, that the situation is not being assumed to be axisymmetric two-dimensional flow. Furthermore, with a manufacturer specified maximum pressure drop of only 0.08 psid, compressibility issues based on changes in density with Mach number should be negligible. Indeed, operating the meter at a nominal pressure of 15 psia, Mach number dependent density changes within the meter should not exceed 0.3% based on this specification, which in itself is probably over-conservative on the part of the manufacturer for most gases. However, with variation in fluid properties dependent on temperature, it is quite probable that temperature-dependent changes in density, transport and thermodynamic properties, hence temperature dependent changes in Reynolds numbers, may affect the system substantially, particularly with density driven buoyancy effects within the heated regions.

4.2 MATHEMATICAL DESCRIPTION

Given the physical description of heat and fluid transfer within the thermal mass flow meter, it becomes essential to represent the system mathematically, so that these descriptions may be reliably analyzed quantitatively. This requirement may be pursued from two different methodologies namely: (i) by setting up a differential momentum balance on the system, or (ii) through presentation of the equations of continuity, motion, and energy. Following Bird, Stewart, and Lightfoot[8], the latter will be pursued for this thesis.

In order to present an adequate mathematical statement of the problem, it is first necessary to describe the problem in an appropriate reference frame. As the predominant driving forces of this problem are in the axial direction of tubular flow, the cylindrical coordinate system will be employed. In most circumstances, the orientation of the meter will be chosen such that the gravitational acceleration vector will be perpendicular to the axial coordinate vector, z, and downward from the horizontal plane of the sensor and bypass flowpaths. This coordinate configuration is presented in Figure 4-1.

The starting point of mathematical representation of the systems is the equation of continuity. In vector notation it reads

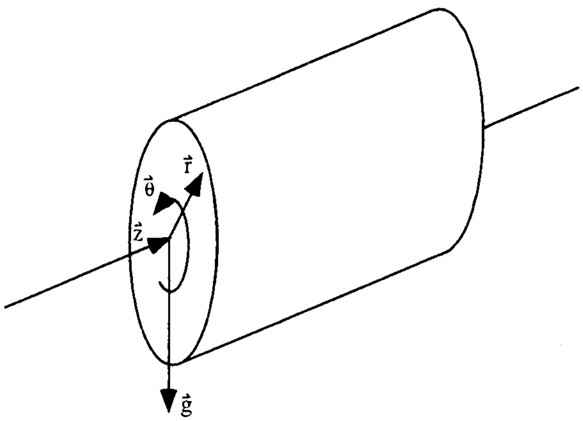

Figure 4-1. Cylindrical Coordinate System Including Gravity Vector.

$$\frac{\partial \rho}{\partial t} = -(\vec{\nabla} \cdot \rho \vec{v})$$ **Equation 4.1**

Represented in cylindrical coordinates, which are convenient to this problem, Equation 4.1 becomes

$$\frac{\partial \rho}{\partial t} + \frac{1}{r}\frac{\partial}{\partial r}(\rho r v_r) + \frac{1}{r}\frac{\partial}{\partial \theta}(\rho v_\theta) + \frac{\partial}{\partial z}(\rho v_z) = 0$$ **Equation 4.2**

For typical axisymmetric flow, assumptions would normally be made regarding the radial and angular velocity components, v_r and v_θ. However, due to the effect of property variations with temperature within the flow, specifically the temperature dependence of density and its associated buoyancy effects, these terms can not be discounted. Thus, Equation 4.2 will remain in its unsimplified form.

The next step in formulating a mathematical description of the systems is the equation of motion. In vector notation, the linear momentum equation is

$$\rho\frac{D\vec{v}}{Dt} = -\vec{\nabla}p - \left[\vec{\nabla}\cdot\vec{\vec{\tau}}\right] + \rho\vec{g}$$ **Equation 4.3**

where the first term corresponds to the mass per unit volume times acceleration and is equated with the sum of forces acting upon it; namely, pressure gradient, viscous, and gravitational forces, respectively. As fluid properties are variable within the system, the equation may be separated into coordinate components, but written in terms of the stress tensor,

$$r\text{:}\quad \rho\left(\frac{\partial v_r}{\partial t} + v_r\frac{\partial v_r}{\partial r} + \frac{v_\theta}{r}\frac{\partial v_r}{\partial \theta} - \frac{v_\theta^2}{r} + v_z\frac{\partial v_r}{\partial z}\right) = -\frac{\partial p}{\partial r} - \left(\frac{1}{r}\frac{\partial}{\partial r}(r\tau_{rr}) + \frac{1}{r}\frac{\partial \tau_{r\theta}}{\partial \theta} - \frac{\tau_{\theta\theta}}{r} + \frac{\partial \tau_{rz}}{\partial z}\right) + \rho g_r$$ **Equation 4.4**

$$\theta\text{:}\quad \rho\left(\frac{\partial v_\theta}{\partial t} + v_r\frac{\partial v_\theta}{\partial r} + \frac{v_\theta}{r}\frac{\partial v_\theta}{\partial \theta} + \frac{v_r v_\theta}{r} + v_z\frac{\partial v_\theta}{\partial z}\right) = -\frac{1}{r}\frac{\partial p}{\partial \theta} - \left(\frac{1}{r^2}\frac{\partial}{\partial r}(r^2\tau_{r\theta}) + \frac{1}{r}\frac{\partial \tau_{\theta\theta}}{\partial \theta} + \frac{\partial \tau_{\theta z}}{\partial z}\right) + \rho g_\theta$$ **Equation 4.5**

$$z:\quad \rho\left(\frac{\partial v_z}{\partial t}+v_r\frac{\partial v_z}{\partial r}+\frac{v_\theta}{r}\frac{\partial v_z}{\partial \theta}+v_z\frac{\partial v_z}{\partial z}\right)= -\frac{\partial p}{\partial z}-\left(\frac{1}{r}\frac{\partial}{\partial r}(r\tau_{rz})+\frac{1}{r}\frac{\partial \tau_{\theta z}}{\partial \theta}+\frac{\partial \tau_{zz}}{\partial z}\right)+\rho g_z$$

Equation 4.6

Following the Navier-Stokes stress/rate-of-strain constitutive law,

$$\tau_{rr}=-\mu\left[2\frac{\partial v_r}{\partial r}-\frac{2}{3}\left(\frac{1}{r}\frac{\partial}{\partial r}(rv_r)+\frac{1}{r}\frac{\partial v_\theta}{\partial \theta}+\frac{\partial v_z}{\partial z}\right)\right]$$

Equation 4.7

$$\tau_{\theta\theta}=-\mu\left[2\left(\frac{1}{r}\frac{\partial v_\theta}{\partial \theta}+\frac{v_r}{r}\right)-\frac{2}{3}\left(\frac{1}{r}\frac{\partial}{\partial r}(rv_r)+\frac{1}{r}\frac{\partial v_\theta}{\partial \theta}+\frac{\partial v_z}{\partial z}\right)\right]$$

Equation 4.8

$$\tau_{zz}=-\mu\left[2\frac{\partial v_z}{\partial z}-\frac{2}{3}\left(\frac{1}{r}\frac{\partial}{\partial r}(rv_r)+\frac{1}{r}\frac{\partial v_\theta}{\partial \theta}+\frac{\partial v_z}{\partial z}\right)\right]$$

Equation 4.9

$$\tau_{r\theta} = \tau_{\theta r} = -\mu\left[r\frac{\partial}{\partial r}\left(\frac{v_\theta}{r}\right) + \frac{1}{r}\frac{\partial v_r}{\partial \theta}\right]$$

Equation 4.10

$$\tau_{\theta z} = \tau_{z\theta} = -\mu\left[\frac{\partial v_\theta}{\partial z} + \frac{1}{r}\frac{\partial v_z}{\partial \theta}\right]$$

Equation 4.11

$$\tau_{zr} = \tau_{rz} = -\mu\left[\frac{\partial v_z}{\partial r} + \frac{\partial v_r}{\partial z}\right]$$

Equation 4.12

At this point, again due to the fact that axisymmetric two dimensional flow will not be assumed, it is not desirable to simplify the equations further. Indeed, even the component body forces will remain in the formulation to allow for evaluating the mass flow meter at various orientations, as the effect of gravitational body forces may be influential on different directions based on the gravitational normal force of each orientation.

It is also necessary to account for energy input and output of the system by considering the equation of energy, represented in vector notation as

$$\rho\frac{D\hat{U}}{Dt} = -\left(\vec{\nabla}\cdot\vec{q}\right) - p\left(\vec{\nabla}\cdot\vec{v}\right) - \left(\vec{\vec{\tau}}:\vec{\nabla}\vec{v}\right)$$

Equation 4.13

The terms in this equation represent the rate of gain of internal energy per unit volume of the system, the rate of internal energy input via conduction per unit volume, the reversible rate of internal energy increase per unit volume due to compression, and the irreversible rate of internal energy increase per unit volume by viscous dissipation, respectively. It is of more engineering value to evaluate this expression in terms of thermal properties and system temperatures as opposed to internal energy. Thus, in cylindrical coordinates, Equation 4.13 becomes

$$\rho\hat{C}_v\left(\frac{\partial T}{\partial t}+v_r\frac{\partial T}{\partial r}+\frac{v_\theta}{r}\frac{\partial T}{\partial \theta}+v_z\frac{\partial T}{\partial z}\right)=-\left[\frac{1}{r}\frac{\partial}{\partial r}(rq_r)+\frac{1}{r}\frac{\partial q_\theta}{\partial \theta}+\frac{\partial q_z}{\partial z}\right]-$$
$$T\left(\frac{\partial p}{\partial T}\right)_\rho\left(\frac{1}{r}\frac{\partial}{\partial r}(rv_r)+\frac{1}{r}\frac{\partial v_\theta}{\partial \theta}+\frac{\partial v_z}{\partial z}\right)-\left\{\tau_{rr}\frac{\partial v_r}{\partial r}+\tau_{\theta\theta}\frac{1}{r}\left(\frac{\partial v_\theta}{\partial \theta}+v_r\right)+\tau_{zz}\frac{\partial v_z}{\partial z}\right\}-$$
$$\left\{\tau_{r\theta}\left[r\frac{\partial}{\partial r}\left(\frac{v_\theta}{r}\right)+\frac{1}{r}\frac{\partial v_r}{\partial \theta}\right]+\tau_{rz}\left(\frac{\partial v_z}{\partial r}+\frac{\partial v_r}{\partial z}\right)+\tau_{\theta z}\left(\frac{1}{r}\frac{\partial v_z}{\partial \theta}+\frac{\partial v_\theta}{\partial z}\right)\right\}$$

Equation 4.14

The latter two terms in braces of Equation 4.14 are associated with viscous dissipation. These particular terms will be disregarded as viscous dissipation does not significantly affect the equation of thermal energy until very large velocity gradients are encountered in the flowstream, i.e. Mach numbers equal to or greater than one[9]. Within this system, the initial assumption, which will be validated later based on actual geometries, is that Mach << 1.

In addition to the equations of continuity, momentum, and energy, it is necessary to further define the problem by imposing initial and boundary conditions. Typically, the no-slip condition is applied to internal flow problems at the solid/fluid interfaces. Kays, however, cautions that significant slip may occur at low Reynolds numbers, provided the Mach number is high enough[10]. Within the laminar boundary layer, Kays expresses the wall slip velocity in comparison to the free stream velocity, U, as

$$\frac{u_w}{U} \approx 0.4 \frac{Ma}{\mathrm{Re}_x^{0.5}}$$ **Equation 4.15**

where, the Reynolds number, Re_X, is defined in terms of the characteristic distance from the leading edge of the flow surface. In order to evaluate whether slip velocities will require further consideration in the mass flow meter, it will be necessary to develop a first order approximation for the flow profile and free stream velocity for various gases. Based on initial, first order analytical solutions, it is possible to evaluate the Mach number and Reynolds number, Re_X, in the boundary layer region, and determine if slip velocities are significant. As detailed in section 4.3, wall velocities may be considered negligible.

Additional boundary conditions are derived from the requirement of equality of temperature or equality of heat flux at all material interfaces. Thus, when a boundary temperature is given and fixed, such as the large thermal mass of the annular bypass casings, the temperature boundary condition at the interface between materials is

$$T_{fluid} = T_{solid}$$ **Equation 4.16**

When the solid heat flux is known, as in the areas surrounding the electrical resistive heaters of the sensor, the corresponding boundary condition becomes

$$\left(k \frac{\partial T}{\partial \eta} \right)_{fluid} = q_{solid}$$ **Equation 4.17**

where η represents the generalized coordinate direction normal to the interfacial surface.

Oftentimes, for certain known thermal and hydrodynamic conditions, a non-dimensional parameter is employed to describe the thermal boundary condition of the flow. This parameter is the Nusselt number and is expressed as[10]

$$Nu = \frac{q_w L}{k_0 (T_w - T_0)}$$ **Equation 4.18**

where q_W represents the boundary heat flux at the fluid/solid interface, as in Equation 4.17, L is a characteristic flow dimension, and T_W and T_0 represent the wall and freestream temperatures, respectively. For typical MFC operation, Hinkle has shown that the Nusselt number within the sensor region of the MFC is typically between the values of 4 and 9.[7] Using numerical methods, however, equivalent film coefficient information will not be explicitly defined, but will be governed by the overall nodal thermal resistance resulting at a given interface.

From the formulations of this section, a full mathematical description of the thermal and hydrodynamics of the MFM system has been defined in general terms. Very little simplification has been performed in order not to neglect nonaxisymmetric effects and temperature-dependent transport properties. With these initial, generalized equations, appropriate formulations may be used to evaluate the systems with numerical methods. However, it is realized that, with the small number of simplifications which have been made, numerical evaluation based on these non simplified expressions may prove inefficient, and unrealistic within the scope of this thesis. As detailed in the following sections, further simplications to the governing equations have been introduced to reduce the mathematical operations which must be performed for simulation.

4.3 DEFENSE OF THE ASSUMPTION OF LAMINAR FLOW

At this time, adequate qualitative and mathematical descriptions of the system have been proposed. It is necessary to defend some of the assumptions of these initial descriptions. Perhaps most significant is to determine the flow regime in which the sensor and bypass flow paths are operating. The intent of MFM manufacturers, including Sierra, is to maintain all flow paths within the meter in the regime of laminar flow, i.e. $Re<2000$. By maintaining this stipulation, the ratio of flow splitting between the sensor flow path and the bypass flow path may remain fairly constant, and a direct measurement of the total flow through the MFM can be ascertained by only measuring the portion of the flow through the sensor.

To determine the Reynolds number of the flow through each path of the MFM, it is necessary to first develop the velocity profile through each path. From this velocity profile, an expression can be obtained for the mean fluid velocity, which will be dependent on the pressure gradient driving the fluid through this path.

As a first approximation for the velocity profile within a selected flow path, it is practical to employ the momentum equation for axisymmetric flow in a circular tube, assuming that all fluid properties are invariant with temperature and pressure. For the geometries involved in the MFMs of this test, this simplification results in the classical solutions of axisymmetric tubular flow and axisymmetric annular flow.

For axisymmetric tubular flow, with generalized variant fluid properties, the simplified steady-state momentum equation with no external body forces applies, often referred to as the *momentum equation of the boundary layer*[10]. From Kays[10], with notation adapted for consistency within this thesis,

Equation 4.19

$$\rho v_z \frac{\partial v_z}{\partial z} + \rho v_r \frac{\partial v_z}{\partial r} + g_c \frac{dP}{dz} = \frac{1}{r}\frac{\partial}{\partial r}\left(r\mu \frac{\partial v_z}{\partial r} \right)$$

Assuming fully developed flow, radial velocity is zero and the change in axial velocity with distance is invariant,

$$v_r = 0$$ **Equation 4.20**

$$\frac{\partial v_z}{\partial z} = 0$$ **Equation 4.21**

These conditions simplify the momentum equation to

$$g_c \frac{dP}{dz} = \frac{1}{r}\frac{\partial}{\partial r}\left(r\mu \frac{\partial v_z}{\partial r} \right)$$ **Equation 4.22**

Assuming (as first order approximation) constant fluid properties, we obtain

$$g_c \frac{dP}{dz} = \frac{\mu}{r}\frac{\partial}{\partial r}\left(r \frac{\partial v_z}{\partial r} \right)$$ **Equation 4.23**

Integrating once

$$\frac{g_c r^2}{2\mu}\frac{dP}{dz} + C_1 = r\frac{\partial v_z}{\partial r}$$ **Equation 4.24**

Integrating again

$$\frac{g_c r^2}{4\mu}\frac{dP}{dz} + C_1 \ln(r) + C_2 = v_z(r)$$

Equation 4.25

Application of the no-slip and axisymmetric-profile boundary conditions allows for determination of the integration constants,

$$\frac{\partial v_z}{\partial r}(r = 0) = 0 \rightarrow C_1 = 0$$

Equation 4.26

$$v_z(r = 0) = 0 \rightarrow C_2 = -\frac{g_c r_0^2}{4\mu}\frac{dP}{dz}$$

Equation 4.27

which, replaced in Equation 4.25, yields

$$\frac{g_c r^2}{4\mu}\frac{dP}{dz} - \frac{g_c r_0^2}{4\mu}\frac{dP}{dz} = v_z(r)$$

Equation 4.28

$$-\frac{g_c r_0^2}{4\mu}\frac{dP}{dz}\left(1 - \frac{r^2}{r_0^2}\right) = v_z(r)$$

Equation 4.29

Having determined this velocity profile, it is now possible to derive the mean fluid velocity within the selected flow path. The mean fluid velocity is related to the overall mass flow rate through the element,

$$V = \frac{\dot{m}}{A_c \rho}$$ **Equation 4.30**

$$\dot{m} = \int_{A_c} v_z(r) \rho \partial A_c$$ **Equation 4.31**

where, for a circular cross sectional area,

$$A_c = \pi r^2$$ **Equation 4.32**

Thus, with substitution of Equation 4.29, Equation 4.31, and Equation 4.32, Equation 4.30 becomes,

$$V = \frac{\int_r -\frac{g_c r_0^2}{4\mu} \frac{dP}{dz} \left(1 - \frac{r^2}{r_0^2}\right) \rho (2\pi r \partial r)}{\pi r_o^2 \rho}$$ **Equation 4.33**

Again assuming constant properties, Equation 4.33 simplifies to,

$$V = -\frac{g_c}{2\mu} \frac{dP}{dz} \int_r \left(1 - \frac{r^2}{r_0^2}\right) (r \partial r)$$ **Equation 4.34**

Performing the integration from r=0 to r=r_0,

$$V = \frac{g_c r_0^2}{8\mu}\left(-\frac{dP}{dz}\right)$$ **Equation 4.35**

Finally, the Reynolds number of the tubular flow may be calculated,

$$\mathrm{Re} = \frac{DV\rho}{\mu}$$ **Equation 4.36**

Inserting appropriate terms into Equation 4.36 results in

$$\mathrm{Re} = \frac{g_c r_0^3}{4\mu^2}\left|\frac{dP}{dz}\right|\rho$$ **Equation 4.37**

A similar procedure may be used to obtain the Reynolds number expression for axisymmetric flow through a concentric annulus Again, beginning with the steady-state momentum equation, with no external body forces and generalized variant fluid properties, Equation 4.19, and applying the steps described in Equation 4.20 through Equation 4.24, leads to the integrated expression for axial velocity with respect to radial distance from the tube centerline, Equation 4.25. Application of the no-slip boundary conditions imposed by both walls of the flow annulus, i.e.

$$v_z(r = \kappa r_0) = 0$$ **Equation 4.38**

where, κ indicates the ratio of the inner and outer radius of the annulus.

$$v_z(r = r_0) = 0$$ **Equation 4.39**

allows for solution of the integration constants C_1 and C_2,

$$C_2 = \frac{-(\kappa r_0)^2 g_c}{4\mu} \frac{dP}{dz} - C_1 \ln(\kappa r_0)$$ **Equation 4.40**

$$C_1 = \frac{\frac{g_c}{4\mu} \frac{dP}{dz} (\kappa^2 r_0^2 - r_0^2)}{\ln(r_0) - \ln(\kappa r_0)}$$ **Equation 4.41**

Substituting the integration constants into the expression for the axial velocity and simplifying,

$$\frac{g_c r^2}{4\mu} \frac{dP}{dz} - \frac{g_c}{4\mu} \frac{dP}{dz} r_0^2 \frac{(\kappa^2 - 1)}{\ln(\kappa r_0) - \ln(r_0)} \ln(r) + \frac{g_c}{4\mu} \frac{dP}{dz} r_0^2 \frac{\ln(r_0)\kappa^2 - \ln(\kappa r_0)}{\ln(\kappa r_0) - \ln(r_0)} = v_z(r)$$ **Equation 4.42**

Having obtained this velocity profile, it is now possible to derive the mean fluid velocity within the selected flow path as done with tubular flow. The same procedure is used as with the capillary formulation.

For annular cross sectional area,

$$A_c = \pi r_0^2 (1-\kappa^2)$$ **Equation 4.43**

With similar substitutions as conducted above, this becomes,

$$V = \frac{1}{(\pi r_0^2 (1-\kappa^2))\rho} \times \int_{\kappa r_0}^{r_0} \left[\begin{array}{l} \dfrac{g_c r^2}{4\mu}\dfrac{dP}{dz} - \dfrac{g_c}{4\mu}\dfrac{dP}{dz} r_0^2 \dfrac{(\kappa^2 - 1)}{\ln(\kappa r_0) - \ln(r_0)} \ln(r) \\ \quad + \dfrac{g_c}{4\mu}\dfrac{dP}{dz} r_0^2 \dfrac{\ln(r_0)\kappa^2 - \ln(\kappa r_0)}{\ln(\kappa r_0) - \ln(r_0)} \end{array} \right] \rho (2\pi r \partial r)$$ **Equation 4.44**

Performing the integration over the bounds indicated results in

$$V = \frac{g_c r_0^2}{8\mu}\left(-\frac{dP}{dz}\right)\left(\frac{\ln(\kappa) + 1 - 2\kappa^2 - \kappa^4 \ln(\kappa) + \kappa^4}{\ln(\kappa)(1-\kappa^2)}\right)$$ **Equation 4.45**

Finally, the Reynolds number of the annular flow may be calculated as

$$\mathrm{Re} = \frac{2r_0(1-\kappa)V\rho}{\mu}$$ **Equation 4.46**

Inserting appropriate terms into this equation results in:

$$\mathrm{Re} = \frac{2r_0(1-\kappa)\left(\dfrac{g_c r_0^2}{8\mu}\left(-\dfrac{dP}{dz}\right)\left(\dfrac{\ln(\kappa) + 1 - 2\kappa^2 - \kappa^4 \ln(\kappa) + \kappa^4}{\ln(\kappa)(1-\kappa^2)}\right)\right)\rho}{\mu}$$ **Equation 4.47**

At this point, expressions have been derived for the Reynolds number of both the bypass and capillary sensor elements of the MFMs used within this thesis. This parameter is dependent upon the fluid properties of density and viscosity, as well as the geometries of the flow paths within the MFM's. Additionally, due to the nature of the derivation, the Reynolds number is also dependent on the pressure gradient, as this gradient is responsible for generation of the velocity in the axial direction. For the first order approximation, this pressure gradient, and therefore velocity, may be obtained by realizing that, due to the parallel geometries of the flow paths, the total pressure drop across the capillary sensor tube will be equal to the pressure drop across the annular bypass element, except for the contribution of minor losses. Obtaining the overall pressure drop is complicated, however, by the fact that the capillary sensor tube is actually comprised of three separate regions; denoted in the dimensional tables as *capillary feedtubes* and the *capillary sensor*. The entire sensor flow path consists of capillary tubing, but the separate sections have different radii. The total pressure drop occurs over two equal length capillary feedtubes, and the capillary sensor tube itself. Since the MFM is operating in a steady state mode, the conservation of mass principle may be applied to find the pressure gradient which occurs in each of these three sections.

Conservation of mass in the presence of steady-state conditions demand that the mass flow rate remains unchanged through the entire sensor flow path, namely

$$\dot{m}_{sensor} = \dot{m}_{feedtube}$$ **Equation 4.48**

Rearranging Equation 4.30 for each portion of the sensor flow path,

$$V_{sensor} A_{csensor} \rho = V_{feedtube} A_{cfeedtube} \rho$$ **Equation 4.49**

Substituting velocities and areas based on each section's geometry,

$$\left[\frac{g_c r_s^2}{8\mu}\left(-\frac{dP}{dz}\right)_{sensor}\right]\left[\pi r_s^2\right]\rho = \left[\frac{g_c r_{sf}^2}{8\mu}\left(-\frac{dP}{dz}\right)_{feed}\right]\left[\pi r_{sf}^2\right]\rho$$ **Equation 4.50**

Rearranging and simplifying,

$$\left(\frac{dP}{dz}\right)_{sensor} = \left[\frac{r_{sf}^4}{r_s^4}\right]\left(\frac{dP}{dz}\right)_{feedtube}$$ **Equation 4.51**

Since the geometries are constant within each region, this may actually be written as

$$\left(\frac{\Delta P}{l_s}\right)_{sensor} = \left[\frac{r_{sf}^4}{r_s^4}\right]\left(\frac{\Delta P}{l_{sf}}\right)_{feedtube}$$ **Equation 4.52**

Further, the sum of the individual pressure drops across each section must total the overall drop across the annular bypass element,

$$\Delta P_{feedtube-upstream} + \Delta P_{sensor} + \Delta P_{feedtube-downstream} = \tau \Delta P_{bypass}$$ **Equation 4.53**

Where, τ may be evaluated as one if there are no minor losses, or less than 1 to account for minor pressure losses. Substituting Equation 4.52 into Equation 4.53 we obtain

$$\Delta P_{sensor}\left[\frac{r_s^4 l_{sf}}{r_{sf}^4 l_s}\right] + \Delta P_{sensor} + \Delta P_{sensor}\left[\frac{r_s^4 l_{sf}}{r_{sf}^4 l_s}\right] = \tau \Delta P_{bypass}$$ **Equation 4.54**

Simplifying,

$$\Delta P_{sensor}\left[\frac{2r_s^4 l_{sf}}{r_{sf}^4 l_s}+1\right]=\tau\Delta P_{bypass}$$ **Equation 4.55**

The pressure gradients across all components may now be written in terms of a single quantity, i.e. ΔP_{bypass},

$$\left(\frac{dP}{dz}\right)_{bypass}=\frac{\tau\Delta P_{bypass}}{l_a}$$ **Equation 4.56**

$$\left(\frac{dP}{dz}\right)_{sensor}=\frac{\Delta P_{sensor}}{l_s}=\frac{\tau\Delta P_{bypass}}{\left[\frac{2r_s^4 l_{sf}}{r_{sf}^4 l_s}+1\right]l_s}$$ **Equation 4.57**

These commonly defined pressure gradients in terms of the pressure drop across the annular bypass can now be employed to obtain this pressure drop. Since conservation of mass requires that the overall mass flow rate through the MFM be the sum of the mass flow rates through the sensor and bypass, the total mass flowrate into the sensor and bypass portions may be separated into components,

$$\dot{m}_{total}=\dot{m}_{sensor}+\dot{m}_{bypass}$$ **Equation 4.58**

Rearranging and substituting Equation 4.30 into Equation 4.58,

$$\dot{m}_{total} = V_{sensor} A_{csensor} \rho + V_{bypass} A_{cbypass} \rho$$ **Equation 4.59**

Substituting the cross sectional area {Equation 4.32 & Equation 4.43} and velocity {Equation 4.35 & Equation 4.45} equations,

Equation 4.60

$$\dot{m}_{total} = \left[\frac{g_c r_s^2}{8\mu}\left(-\frac{dP}{dz}\right)_s\right]\left[\pi r_s^2\right]\rho$$
$$+\left[\frac{g_c r_b^2}{8\mu}\left(-\frac{dP}{dz}\right)_b\left(\frac{\ln(\kappa)+1-2\kappa^2-\kappa^4\ln(\kappa)+\kappa^4}{\ln(\kappa)(1-\kappa^2)}\right)\right]\times$$
$$\left[\pi r_b^2(1-\kappa^2)\right]\rho$$

Substituting in the derived expressions for the pressure gradients, Equation 4.56 and Equation 4.57,

Equation 4.61

$$\dot{m}_{total} = \left[\frac{g_c r_s^2}{8\mu}\left(-\frac{\tau\Delta P_{bypass}}{\left[\frac{2r_s^4 l_{sf}}{r_{sf}^4 l_s}+1\right]l_s}\right)\right]\left[\pi r_s^2\right]\rho$$
$$+\left[\frac{g_c r_b^2}{8\mu}\left(\frac{-\tau\Delta P_{bypass}}{l_a}\right)\left(\frac{\ln(\kappa)+1-2\kappa^2-\kappa^4\ln(\kappa)+\kappa^4}{\ln(\kappa)(1-\kappa^2)}\right)\right]\left[\pi r_b^2(1-\kappa^2)\right]\rho$$

Rearranging terms, the pressure drop across the bypass annulus can finally be evaluated as

Equation 4.62

$$\tau\Delta P_{bypass} = \frac{-\frac{8\mu\dot{m}_{total}}{g_c\rho}}{\frac{\left[\pi r_s^4\right]}{\left[\frac{2r_s^4 l_{sf}}{r_{sf}^4 l_s}+1\right]l_s}+\left[\left(\frac{\ln(\kappa)+1-2\kappa^2-\kappa^4\ln(\kappa)+\kappa^4}{\ln(\kappa)(1-\kappa^2)}\right)\right]\frac{\left[\pi r_b^4(1-\kappa^2)\right]}{l_a}}$$

Sufficient preliminary evaluations have now been performed to acquire the Reynolds number parameters for each sample MFC. In so doing, the Reynolds number is evaluated at maximum flow conditions specified for each MFM and entrance and exit losses are assumed negligible, thus τ=1. Equation 4.62 is used to generated the annular bypass pressure drop for the given flow rate, MFC geometries, and gas properties of viscosity and density. Equation 4.56 and Equation 4.57 are then evaluated to provide the pressure gradient across the bypass and capillary sensor tubing, respectively. Equation 4.35 and Equation 4.45 are then evaluated to indicate the mean velocities within the two sections. Finally, Equation 4.37 and Equation 4.46 are employed to determine the Reynolds number in each section. The results of these calculations are presented in the Table 4-1, and clearly indicate that the MFC's will be operating well within the laminar region of Reynolds numbers (Re<2000), as demonstrated by the barchart of Figure 4-2.

Table 4-1. Reynolds Number Approximations for Various Gases.

Gas	ρ (g/l)	μ (upoise)	ΔP (Pa)	Q max (sccm)	m' (mg/sec)	$(dP/dx)_b$ (Pa/cm)	$(dP/dx)_s$ (Pa/cm)	V_b (cm/sec)	V_s (cm/sec)	Re_b	Re_s
Ar	1.782	226.5	-59.5	2000	59.41	-18.72	-9.27	172.17	74.23	135.49	44.51
CO_2	1.975	149.6	-39.3	2000	65.83	-12.36	-6.12	172.17	74.23	227.30	74.67
Cl_2	2.980	134.2	-35.3	2000	99.33	-11.09	-5.49	172.17	74.23	382.32	125.59
He	0.178	381.8	-100.4	2000	5.95	-31.55	-15.62	172.17	74.23	8.05	2.64
N_2	1.165	177.5	-46.7	2000	38.83	-14.67	-7.26	172.17	74.23	113.00	37.12
NO_2	1.843	147.0	-38.6	2000	61.44	-12.15	-6.01	172.17	74.23	215.90	70.92
SF_6	1.880	151.1	-39.7	2000	62.67	-12.49	-6.18	172.17	74.23	214.22	70.37

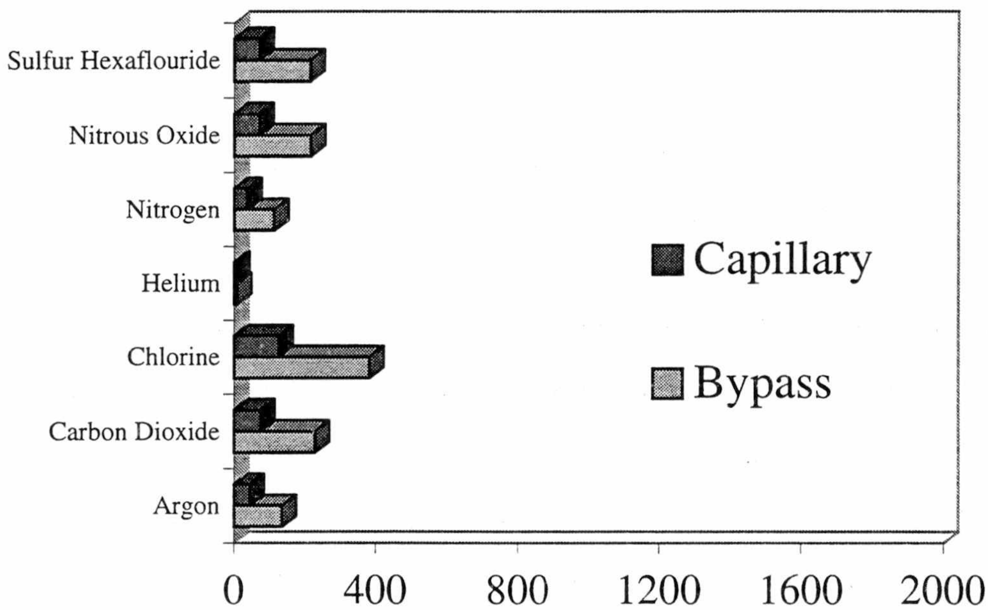

Figure 4-2. Reynolds Numbers of Bypass and Capillary for Various Gases.

4.4 COMPRESSIBILITY ISSUES

From the initial, first order approximations for determining the flow regime in which the flowpaths of an MFC are operating, it becomes evident that the pressure drop across the MFC is very small. Indeed, even with a large factor of safety, the ratio of the change in pressure to the total system pressure is $<< 0.1\%$. This low pressure drop corresponds well with manufacturer provided specifications which indicate the maximum pressure drop across an MFC should not exceed 0.08 psid.

Confirmation of the manufacturer's specified maximum pressure drop allows for a great simplification; indeed, the fluid dynamics within the system may be regarded as that of incompressible flow. Further, in addition to density, all other property variations with respect to pressure do not need to be taken into account. This includes viscosity, thermal conductivity, and the thermal heat capacity, which may now be evaluated as C_p.

4.5 VISCOUS DISSIPATION AND SLIP CONDITIONS

In addition to indicating a very low overall pressure drop across the MFC, Table 4-1 also indicates very low fluid velocities throughout the system. These approximated velocities validate the initial assumption that velocities correspond to a Mach number $<< 1$, and therefore support discarding the viscous dissipation terms in the energy equation, Equation 4.14. Further, evaluating Equation 4.15 with the data of Table 4-1, it shows that Kays' slip-velocity expression at low Reynolds Numbers yields negligible wall velocities. Taking helium as the limiting case, i.e. with the lowest sensor Reynolds number, the wall slip velocity can be shown to be approximately 0.05% of the free stream velocity. With this low value, no-slip conditions may be assumed.

4.6 THERMAL AND HYDRODYNAMIC ENTRANCE LENGTH

In addition to the simplification of constant properties with respect to pressure, the incompressible flow simplification allows the use of many conventionally accepted fluid dynamic approximations. These approximations may be useful in understanding and describing the thermal and hydrodynamics of the problem. One relevant approximation has been derived for the hydrodynamic entry length[11]. This parameter, which indicates the length of tube necessary for the full development of a laminar velocity profile, is useful in predicting if a flow profile is still undergoing change at a critical process point in the instrument. The non-linearity of an MFC with different gases may be somewhat dependent upon inadequate hydrodynamic entrance lengths. If a velocity profile has not yet been established in the area where the capillary sensor heaters are both heating and sensing the flow, measurement may be affected differently than if the velocity profile were established. Thus different gases, with different hydrodynamic entrance lengths would exhibit different non-linear measurement behavior at the sensor based on the full or partial development of their velocity profiles.

Kays provides an approximation for the hydrodynamic entrance length of a capillary based on procedures first implemented by Langhaar[10,11],

$$\frac{x}{D} = \frac{\text{Re}}{20}$$ **Equation 4.63**

where x represents the hydrodynamic entrance length. This approximation may be applied directly to the sensor capillary tube of an MFC. Table 4-2 and Figure 4-3 present the hydrodynamic entrance length for various gases for the test MFC's based on the approximate Reynolds numbers obtained in Table 4-1. For reference, the actual dimensionless entrance length, based on the straight path length upstream of the upstream heater/RTD sensor has also been indicated for comparison with the calculated hydrodynamic entrance length. As evidenced by these results, it is clear that a sufficient hydrodynamic entrance length has been allowed for all gases, such that a fully developed profile is instated well before the flow enters the heat input/measurement area.

Having obtained an approximate expression for the hydrodynamic entrance length, the Prandtl number allows for a quick approximation of the thermal entrance length. Similar to the hydrodynamic entrance length, the thermal entrance length indicates the amount of distance a flow must travel until a fully developed thermal profile is achieved. The Prandtl number may be represented as

$$\Pr = \frac{\mu C_p}{k}$$ **Equation 4.64**

Evaluation of the terms of this expression indicates that the Prandtl number is a ratio of the viscous diffusion rate to the thermal diffusion rate. At pressures and temperatures within the operating range of an MFC, gases typically have Prandtl numbers ranging from 0.6 to 0.9 [10]. Therefore, as the thermal diffusion rate is more significant than the viscous diffusion rate, it can be expected that the thermal entrance length for gases will be smaller than the hydrodynamic entrance length.

Table 4-2. Hydrodynamic Entrance Length for Various Gases.

Gas	*Calculated Hydrodynamic Entrance Length*	*Actual Entrance Length (x/D)*
Argon	2.225	50.3
Carbon Dioxide	3.733	50.3
Chlorine	6.280	50.3
Helium	0.132	50.3
Nitrogen	1.856	50.3
Nitrous Oxide	3.546	50.3
Sulfur Hexaflouride	3.519	50.3

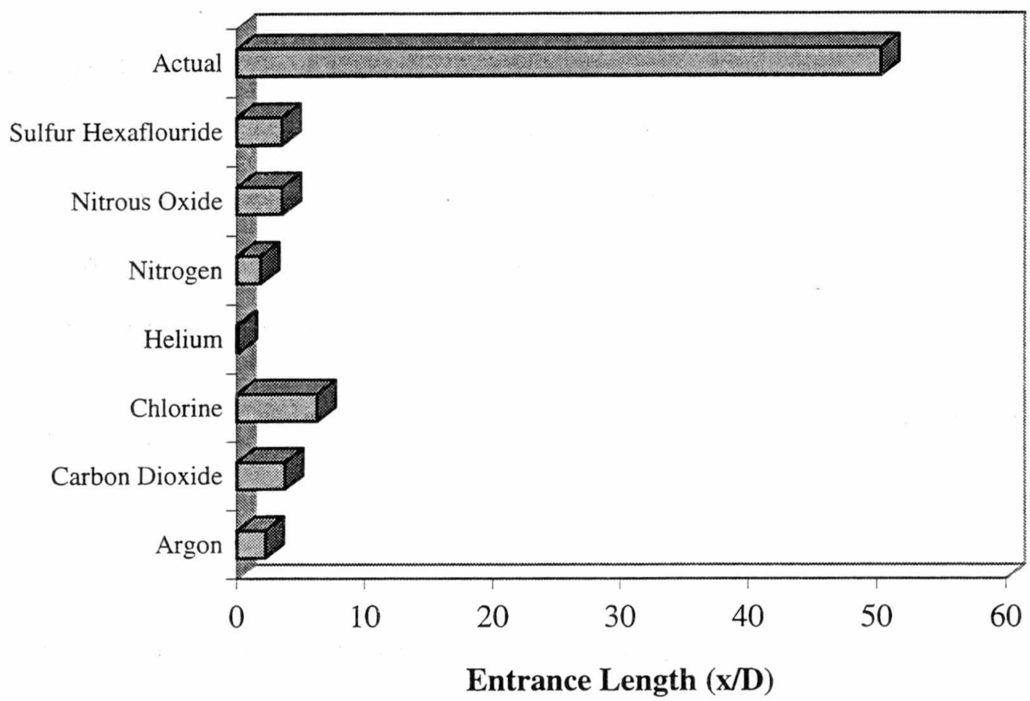

Figure 4-3. Actual and Calculated Hydrodynamic Entrance Length.

4.7 BUOYANCY ISSUES

The overall pressure drop across the MFC has been shown to be insignificant with respect to the variation of fluid properties based on local pressures. Unfortunately, temperature gradients within the system are not as small. Indeed, from initial discussions with Dr. John Olin, President of Sierra Instruments, it is not unlikely that a fluid may see localized temperature increases within the capillary sensor in excess of 100 degree Celsius[3]. Using an ideal gas as a reference, and evaluating the ratio of temperature change to the overall system temperature, this magnitude of temperature change can affect fluid densities by almost 40%. These density changes, coupled with the approximations of Table 4-1, which indicate that axial flow velocities are very small, may have significant buoyancy induced effects on the thermal and hydrodynamic profiles of the flow.

The Grashof number is an important dimensionless parameter used to relate the effect of buoyancy on a system[8]. Coupled with the Reynolds number, it is an excellent indicator for determining how significant buoyancy forces are with respect to inertial forces, and, thus, how much buoyancy forces will affect the overall pattern of a flow. The Grashof number is calculated as

$$Gr = \left[\frac{\bar{\rho}^2\bar{\beta}gb^3\Delta T}{\mu^2}\right]$$ **Equation 4.65**

where barred terms indicate evaluation at the localized mean fluid temperature. Using the Grashof number with the Reynolds number, a ratio of the buoyancy forces to inertial forces may be related, as

$$\frac{Gr}{\mathrm{Re}^2} = \left[\frac{\bar{\rho}\bar{\beta}gD\Delta T}{\rho V^2}\right]$$ **Equation 4.66**

This equation may be simplified, however, by removing similar terms,

$$\frac{Gr}{\mathrm{Re}^2} = \left[\frac{gD}{V^2}\right]$$ **Equation 4.67**

This simplification allows for the very quick evaluation of the degree of buoyancy induced effects based on the dimensions and velocities of a given system It may quickly be seen, based on the diameter of the sensor tube as presented in Chapter 3, i.e. .381 mm, and the velocities within this tube, as presented in Table 4-1, that the ratio of buoyancy induced forces to inertial forces is very small, and much less than unity. Thus, buoyancy induced forces may be disregarded for this system.

5. NUMERICAL MODELING

5.1 SELECTION OF A MODELING PACKAGE

In developing a numerical simulation of the mass flow meters of this thesis, three selection criteria were employed to choose an appropriate existing simulation package. The first, and obvious criterion, is that the package had to be able to efficiently address, either readily, or with simple modification, the governing thermal and hydrodynamic phenomena involved with the test specimens specific to this thesis. The second criterion was that the package should be readily available to the author for use both during this thesis work, and afterwards during the remainder of his engineering career. Obviously, the time spent upon the initial learning curve of any tool is time well spent if that tool can be used far beyond the time when the work initially demanding the tool is complete. Finally, the package had to be in a form which would allow future revisions in order that it might present flexibility for the coverage of a broader range of problems than might have originally been intended.

Two modeling packages were evaluated as candidates for this study. The first package was TEMPEST Version N, created by D.S. Trent and L.L. Eyler of Pacific Northwest Laboratory (PNL), administered by Battelle[12]. The TEMPEST package is a FORTRAN based finite difference package which was initially developed for the Department of Energy (DOE) PNL facility for the simulation and evaluation of waste transport. The TEMPEST package has been employed by other ORNL researchers for various studies, including a number of simulations which evaluated predominantly buoyancy driven flows. In evaluating the merits of the package, a personal interview was conducted with a TEMPEST user which indicated that the package should indeed be capable of handling the present problem efficiently[13]. Further, being developed at a DOE sponsored national laboratory, the package was freely available to all government institutions and thus adequately met requirement 2 of the selection criteria. Finally, TEMPEST is a FORTRAN based application complete with all source files, all of which are clearly commented and can be readily modified to offer excellent flexibility.

The TEMPEST package is able to handle a diverse array of thermal and mass transport problems. Derived from a waste remediation background, the package is specifically suited to handling multicomponent mixtures and buoyancy driven transport phenomena. The base governing equations used in the package are the conservation laws which supports any transport problem; mass, momentum, and energy. In addition, in order to handle the buoyancy driven transport of many waste remediation situations, TEMPEST makes use of thermodynamic state relationships in which density may be evaluated as a function of temperature. Other material properties may also be defined as temperature dependent including viscosity, thermal heat capacity, and thermal conductivity. Although not necessary for the modeling required within this thesis, TEMPEST has excellent constituent component handling abilities including formulations for molecular diffusivity and thermal diffusivity of these components. Also not necessary, but handled well within the application are flow turbulence issues including turbulent kinetic energy formulations, dissipation of turbulent kinetic energy, and associated effective turbulent viscosity derivations.

The second package evaluated as a candidate for this study was the COSMOS/M package, published by the Structural Engineering Design Corporation. COSMOS/M is a finite element modeling system which includes a structural CAD development application in addition to many modules which offer capabilities throughout the structural, thermal, and fluid dynamics fields. As with TEMPEST, an interview was conducted with a COSMOS/M user to determine if the application was suitable to the requirements of this study. From this initial interview, and study of the COSMOS/M documentation, it appeared that this package was quite suitable to the problem at hand. Further, COSMOS/M is a finite element package as opposed to TEMPEST, which is a finite difference package. Whereas TEMPEST must "time march" to a final steady state solution, COSMOS/M is capable of explicitly solving the steady-state thermal and hydrodynamics of a flow analysis problem. Further, the application was readily available to the author, both on a personal computer workstation, and on a higher speed Silicon Graphics multiprocessor system.

Perhaps most significant in COSMOS/M is its high quality mesh generation abilities. Upon graphically creating the geometry of the problem, one can readily denote various surfaces and regions, or macros, which can be discretely meshed and receive the appropriate boundary conditions. Unlike TEMPEST, which has no graphical interface and requires difficult integer data entry into defined input fields, the graphical interface of COSMOS/M makes the meshing and boundary condition specifications of finite element analysis very easy to implement and understand. Finally, although COSMOS/M is not available in source code format, the flexibility of the package and the fulfilling of the third selection criterion is still very good due to its implementation of various "discipline" packages which allow it to be expanded for virtually any engineering analysis endeavor.

One limitation of both packages is that the applications are unable to handle viscous compressible flow. There is no allowance in either package for functional variation of density with localized pressure of viscous flows. Although this limitation would have impact on many gaseous flow problems, preliminary first order approximations presented in Chapter 4 indicate that, due to the extremely small pressure changes that occur within an MFM, incompressible flow is a valid assumption for these devices. Thus, the inability to handle compressible flow was not a significant problem. In evaluating thermodynamic state relations and material properties, a constant system pressure of 15 psia, as presented in Chapter 4, will be assumed.

After substantial debate, a decision was made to select COSMOS/M as the candidate of choice for this study. Although both applications are excellent tools for numerical analysis of fluid flow and heat transfer, COSMOS/M was chosen primarily on the bases of its ability to explicitly perform a steady state analysis and its excellent meshing capabilities.

5.2 APPLICATION-IMPOSED PRINCIPAL ASSUMPTIONS

Several other restrictions were applied by the author to the finite element model, namely:

1. The fluid is in single phase.
2. Body forces other than gravity are not considered.
3. The fluid is Newtonian and, for laminar situations, the Navier-Stokes equations apply.
4. Flow remains laminar for all flowpaths.
5. The viscous dissipation is eliminated.

The assumption of a single phase fluid, assumption 1, is required by both COSMOS/M and the thermal mass flow meter itself. Mass flow meters and controllers are, by nature, unable to accurately handle two-phase flow, such as might be encountered by condensing vapors of low vapor pressure gases. The condensation process greatly affects overall volumetric flowrate, as the condensed fluid represents a significant portion of the overall flow. With unknown and unequal condensation or other two-phase flow effects within the separate flowpaths of the MFC, accurate measurement is impossible. Further, in the semiconductor industry, condensing corrosive gases can have disastrous results from both the flowrate accuracy and facility safety viewpoints. Thus, extensive practices are employed to keep this scenario from occurring. Several of the common process gases used in the semiconductor etch process are low vapor pressure gases, such as boron trichloride and tungsten hexaflouride. These gases are susceptible to condensing out at cooler locations and elbows within the high pressure side of process gas lines. As most of these processes are flow metered at the control valve on the downstream side of an MFC, this puts the MFC in a prime location for condensation induced failure. Thus, engineering practices are employed to ensure that all lines up to and including the MFC are appropriately heated in order to ensure that two-phase flow effects are not likely to occur. Therefore, COSMOS/M's requirement of single phase flow does not detract from the validity of simulation from the MFC viewpoint.

The second assumption that no other body forces other than gravity are considered is also valid from the viewpoint of MFC modeling. Due to the fact that most, if not all, MFC's and MFMs feature local electronics adjacent to the flow path, these instruments cannot be implemented in areas with high EMF which would be required to create electromagnetically induced body forces on the fluid.

Although similar investigations could be conducted on non-Newtonian fluids, the scope of this thesis is limited to Newtonian fluids, which the very wide majority of applications utilize. Therefore, assumption 3 is valid within the scope of this thesis.

Initial approximations presented in Chapter 4 indicate that the Sierra thermal mass flow meters investigated in this study clearly subscribe to laminar flow conditions throughout their operating range for the variety of gases chosen within this study. For this reason, turbulent flow considerations do not pertain to this system and assumption 4 is valid. Also, as indicated in Chapter 4, velocity gradients within the system are not significant enough to demand the evaluation of the viscous dissipation terms of the energy equation and assumption 5 is also valid.

5.3 NUMERICAL VALIDATION

Prior to the use of any scientific tool, it is essential to validate the tool's performance within the bounds of a given problem. This validation process is particularly important when dealing with numerical techniques in engineering, as application of erroneous methods may yield convincingly consistent data, which might in fact be completely unreliable. COSMOS/M is a very well documented finite element package, and features a catalog of validation studies for each engineering endeavor for which the package may be employed. Pertinent to the issues involved within this thesis, the COSMOS/M manual presents numerical validation studies for the following topics[14]:

- Developing flow in an axisymmetric duct.
- Flow through the annulus of two cylinders.
- Natural convection in a two dimensional square cavity.

- Heat conduction in a solid with temperature dependent conductivity.
- Transient heat conduction in a long cylinder.

From these studies, a specific appreciation of the validity of COSMOS/M for common heat and flow modeling processes may be developed. However, it is still understood that the potential for error exists for problems not specifically addressing these validated examples . The sources of these errors are numerous, including undiscovered programmatic errors within the software itself, convergence errors due to improperly or poorly meshed regions, and input errors resulting from improper engineering unit consistency, inaccurate or inconsistent boundary conditions, or simply from inaccurate user data.

Because of the high potential for error, it is essential that a specific validation procedure be implemented in order to validate the simulation as developed for the entire heat/flow problem. Upon developing a numerical model, the validation procedure should initially consist of a mesh convergence study for each discretized portion of the model in order to determine that a mathematically stable solution results. Upon the completion of a mesh convergence study, the validation study should collect simulation data for comparison against experimental data. If the simulation data agrees well with independently generated experimental data, the simulation may be used with a good degree of confidence provided that the simulation is not employed beyond the scope of parameters tested within the experimental validation.

5.4 MODELING APPROACH

The dual flowpaths of the Sierra mass flow meter present a difficult problem with respect to developing a single, all encompassing, numerical model. Taken as one complete system, the asymmetric nature of the bypass and sensor flowpaths would require the development of a three dimensional model which would not have the convenience of symmetry. It would, furthermore, pose significant complexity in using a traditional drawing design package to adequately join surfaces and contours. The complexity of this design is further complicated by the fact that the required three dimensional configuration, demanded by the asymmetry of the problem, immediately makes the numerical problem more memory intensive, and much slower to converge.

The complexity of the problem can be greatly simplified by treating the dual flowpaths of the mass flow meter as two completely separate entities, each of which may be analyzed independent of the other. In so doing, the annular bypass flowpath and the capillary sensor tube are studied separately. Numerical simulation may then be performed individually on each entity, or concurrently by realizing the common pressure drop between the flowpaths. Decoupling the two flowpaths in this manner allows for several simplifications. Primarily, it removes the asymmetrical nature of the entire system, and allows each flowpath component to be evaluated using symmetry and two dimensional discrete elements. This simplification allows for much more efficient memory usage, and allows for the use of a much more refined grid by freeing up memory which otherwise would have been required in the asymmetric three-dimensional model. This simplification also allows for a much simpler representation of the problem from the computer aided design viewpoint. As opposed to a three-dimensional structure which must be extruded from various two dimensional parts, a simpler two-dimensional slice of each of the two components may be utilized.

In order to evaluate the mass flow meter system as two, separate, two-dimensional components, several assumptions must be applied. The first assumption is that each of the two components is subjected to the same overall pressure drop across its entirety. This assumption was discussed previously in Chapter 4 and is revisited here for clarity. Under this assumption, the upstream and downstream plenums are large areas before and after the annular bypass insert. These regions represent common nodes to each of the two flowpaths and therefore each path experiences approximately the same pressure drop. In order to model the MFM in this manner, the entire flowpath is not evaluated but only the portions which experience the same pressure drop, as indicated in Figure 5-1. As all flow through the MFM must pass through this region, continuity insures that all flow through the MFM is being considered.

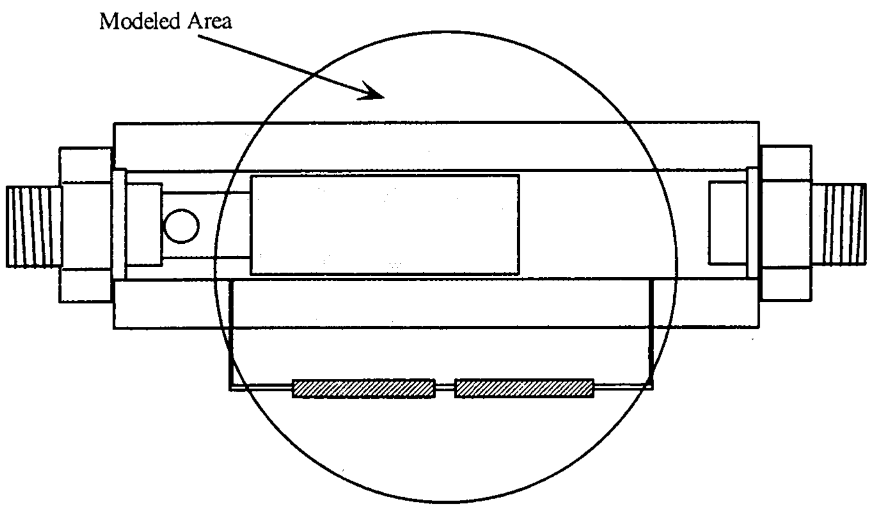

Figure 5-1. Modeled Portion of the Mass Flow Meter.

It is realized that by modeling the MFM in this manner, some inaccuracy will develop from neglecting the effects which the unmodeled upstream and downstream areas have on the flow. For instance, minor pressure losses will be encountered at the entrance and exit of the capillary sensor flowpath. It can be shown, however, that these minor pressure losses are insignificant in comparison to the pressure drop which occurs due to Hagen-Poiseuille flow within the capillary sensor tube. This caution is discussed further in the results sections of Chapter 7.

The common plenum areas upstream and downstream of the two flow components allow for the decoupling of each component from the velocity viewpoint, even though sizable recirculation zones may develop in the downstream plenum. Maintaining the requirement of continuity of mass throughout each region, the velocities within each section are inversely related to the cross sectional area through which the flow must pass. As the plenum area presents a cross sectional area several orders of magnitude greater than the critical dimensions of the annulus and the sensor flowpath, the velocity effects of each section upon the other may be disregarded at the common plenum nodes, essentially treating this region as a velocity stagnation area.

Given these assumptions, the Sierra annulus and sensor flowpaths will thus be modeled as two completely separate entities. For each of the two entities, the relationship between the driving pressure force and the flow will be established by employing the simulation for a variety of different pressure drops across each flowpath. In addition to the pressure/flow relationship of each flowpath, the temperature gradient experienced by the capillary tube heater/sensing elements will be quantified for each flow rate. From this information, a temperature to flow relationship can be determined for the entire system by assigning a temperature gradient to the addition of the flow contribution from both the sensor and bypass for a given driving pressure force. As the temperature gradient is directly proportional to the output indication of the mass flow meter, the overall indicated flow may thus be described by stating the temperature gradient experienced by the sensors within the capillary flow sensor. Since the ultimate goal of this modeling is the determination of the gas correction functions of various gases with respect to nitrogen, a convenient simplification is to reference all flow indications to a standardized nitrogen flow. Thus, a meter's indicated output will be designated equivalent to a corresponding actual nitrogen flow. As the sensor's temperature gradient is directly related to the actual nitrogen flow, this allows for all sensor temperature gradients, and thus flow indications, to correlate directly with a reference nitrogen flowrate. When running a gas other than nitrogen, the gas flowrate which results in this same temperature gradient may then simply be divided by the corresponding reference nitrogen flowrate to obtain the gas correction factor, k, at that specific flowpoint. The set of gas correction factors obtained throughout a domain of flowrates will then be defined as the gas correction *function* for the evaluated gas with respect to nitrogen.

5.5 MODELING OF THE BYPASS ANNULUS

Basically, the flow bypass may be described as a flow path with an annular plenum input, a forward facing step restricting the flow to a thin annular skin, and a rearward facing step which opens the flow up to a large downstream tubular plenum output. The surrounding stainless steel housing and the stainless steel annular insert present substantial thermal bulk to the system, and may be modeled as solid surfaces with constant thermal conductivity with the outer surface maintained at a constant temperature, as determined experimentally. Entering gas temperatures are also set at a constant temperature, as the flow equilibrates with the prevailing ambient temperature in the long piping lengths upstream of the mass flow controller, where the length to inner diameter ratio is larger than three orders of magnitude.

The fluid flow within the bypass annulus is modeled by imposing the no-slip, zero-velocity, condition on all solid wall surfaces of the outer housing and the annular insert. A symmetrical boundary condition of zero radial flow is imposed on the downstream plenum area at the axisymmetric boundary of the centerline of the flow. As the annulus is modeled using two-dimensional symmetry, the angular velocity component of the flow is set to zero for all discrete nodal positions. The driving pressure boundary conditions are imposed by setting a constant upstream pressure at the flow inlet to the annulus, and a constant downstream pressure at the flow outlet. Fluid properties are established as temperature dependent curves, and include the properties of density, viscosity, thermal heat capacity, and thermal conductivity. The volumetric expansion coefficient, and beta values for a fluid are also defined, but are set to constant values since they do not vary significantly over the temperature range experienced within the annulus.

To efficiently generate numerical data from the finite element model, it was necessary to non-uniformly mesh the flow elements of the discretized annulus. A relatively course mesh was utilized within the upstream and downstream plenum areas, with recognition that fluid velocities and properties will not experience significant gradients within these regions. In contrast, near the boundary layers, as developed due to the no-slip condition at solid surfaces, and near flow shaping surfaces, i.e. corners, etc., a more refined mesh was imposed. Due to the very large length to width ratio of the annular bypass region, it is not feasible to diagram the meshing beyond this verbal description of refinement near the boundary layers. Figure 5-2 presents an overview of the boundary conditions implemented for the annular bypass component of the finite element model. The COSMOS/M code used to create this model is included as Appendix A, COSMOS/M Batch File Code for Annular Bypass Model.

COSMOS/M utilizes a bilinear quadrilateral finite element, FLOW2D, for two-dimensional axisymmetric flow modeling. COSMOS/M fully couples heat transfer with mass transfer using this element. In order to do this, a requirement of COSMOS/M is that all elements within a heat/flow transfer

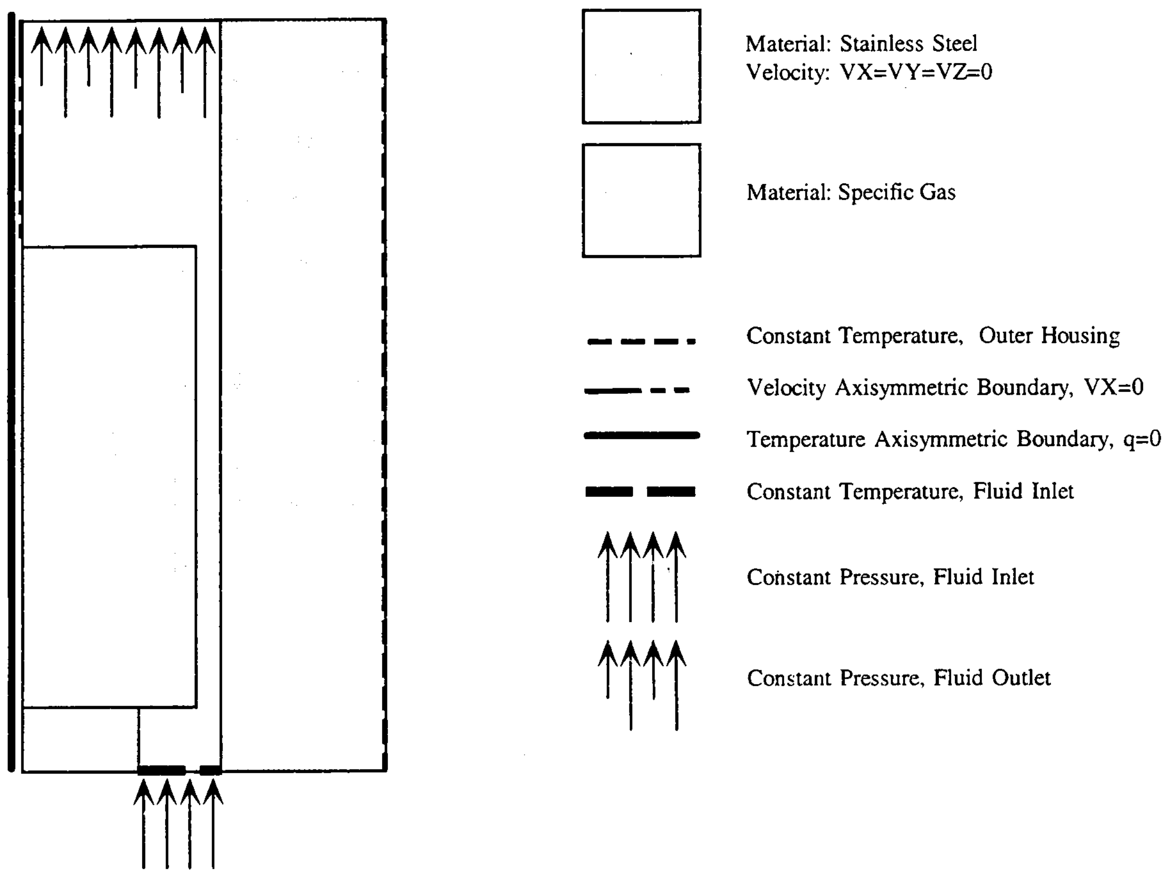

Figure 5-2. Boundary Conditions of Annular Flow Bypass.

model be the FLOW2D element. Obviously, it is desirable that a model contains non-fluid entities, such as tube walls, etc. Using the FLOW2D element for all entities therefore requires the constraint of all velocities of all solid elements of a model to zero[14].

5.6 MODELING OF THE CAPILLARY SENSOR FLOWPATH

The capillary sensor portion of the MFC model may be described as a flow path with a tubular input, a forward facing step restricting the flow to a smaller diameter capillary tube, and a rearward facing step which increases the diameter of the flow path. The upstream and downstream inlet and outlet sections are surrounded by a considerable mass of stainless steel housing. The forward and rearward facing steps, which respectively constrict and enlarge the flowpath, are located within this housing section in close proximity to the actual sensing portion of the path. In this sensing portion, the gas flows within a thin-walled stainless steel capillary tube which is in turn surrounded by an insulative blanket. The actual sensors are modeled as axisymmetric surfaces with a constant current driven heat source, located between the stainless steel capillary tube outer wall and the insulating wrap. Similar to the annulus bypass portion, the overall outer surface is specified at a constant temperature, as determined experimentally, as is the inlet fluid temperature.The fluid flow within the capillary tubing is modeled by imposing the no-slip, zero-velocity, condition on all solid wall surfaces of the inner wall of the capillary tubing and the upstream and downstream step regions. A symmetrical boundary condition of zero radial flow is imposed along the entire flow path at the axisymmetric boundary of the centerline of the flow. As the capillary is modeled using two-dimensional symmetry, the angular velocity component of the flow is set to zero for all discrete nodal positions. The driving pressure boundary conditions are imposed by setting a constant upstream pressure at the flow inlet to the annulus, and a constant downstream pressure at the flow outlet. Fluid properties are established as temperature dependent curves, and include the properties of density, viscosity, thermal heat capacity, and thermal conductivity. The volumetric expansion coefficient, and beta values for a fluid are also defined, but since they do not vary significantly over the temperature range experienced within the annulus, are set to constant values.

To generate numerical data efficiently from the finite element model, it was necessary to non-uniformly mesh the zones of the discretized capillary sensor region. A relatively coarse mesh was utilized within the upstream and downstream stainless steel outer housing, as the relatively high thermal conductivity decreases the magnitude of thermal gradients. A more refined mesh was employed within the flow path, as velocity gradients and temperature gradients are greater within this region. Due to the significant length to width ratio of the capillary sensor region, it is not feasible to diagram the meshing to the scale actually used. However, Figure 5-3 presents an overview of the boundary conditions implemented for the capillary sensor component of the finite element model. The COSMOS/M code used to create this model is included as Appendix B, COSMOS/M Batch File Code for Capillary Sensor Model.

5.7 TEMPERATURE DEPENDENT PROPERTIES

A key feature of the numerical modeling conducted for this thesis is the inclusion of the temperature dependency of gas material properties. COSMOS/M is able to handle a wide array of thermally dependent parameters by utilizing temperature curves. To employ a temperature curve, a curve is defined with multiplicative scalar factors at each respective temperature value. This curve may then be activated when defining material properties and boundary conditions. Upon activating the curve, all subsequent value definitions are multiplied by the corresponding multiplicative scalar factor, depending on the run-time temperature of the corresponding nodal element. For instance, when defining the density of a material, a temperature curve is generated which contains a density value at temperature points from ambient, 270K, to the maximum temperature the system will experience, i.e. 450 K. This curve is then activated, and the density of the material is defined as unity. Therefore, during runtime, the density of each

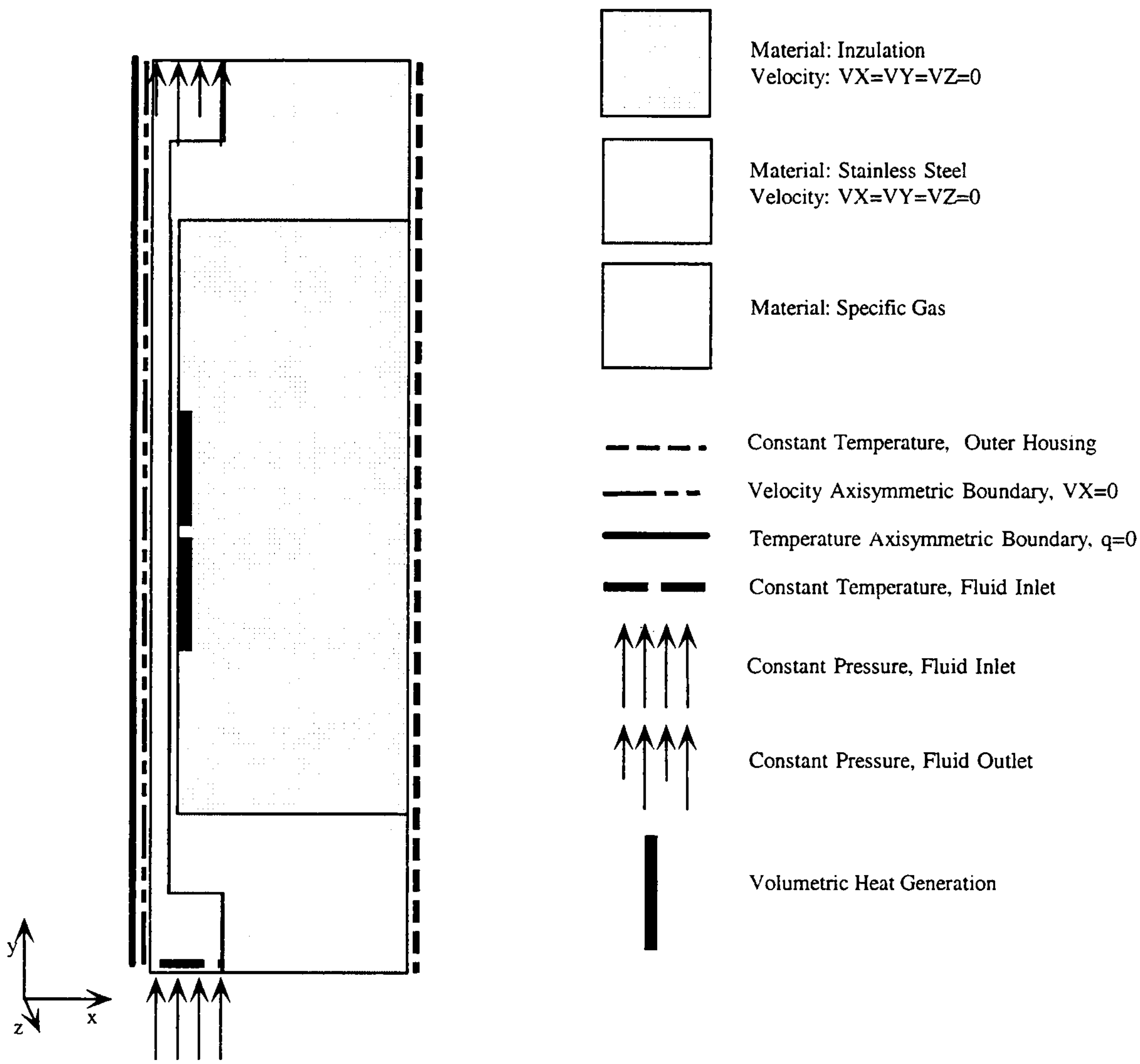

Figure 5-3. Boundary Conditions of Capillary Sensor Flowpath.

element of the corresponding material will be defined based on the value obtained from the activated temperature curve. Linear interpolation is used for nodal temperatures which do not correspond to exact defined points on the temperature curve. Using this methodology, the density, viscosity, thermal conductivity, and thermal heat capacity of gases are all defined as temperature dependent. Temperature dependent gas property data was obtained from publications by the National Standard Reference Data Service of the former USSR, which produced a series of property tables for various gases in 1988. The thermophysical properties of nitrogen are presented in Table 5-1. Table 5-2 and Table 5-3 presents the data for argon and helium respectively. Figure 5-4 through Figure 5-7 graph the temperature dependence of the density, specific heat, viscosity, and thermal conductivity of argon, helium, and nitrogen.

In addition to temperature dependent material properties of gases, it is also necessary to simulate the temperature dependence of the resistivity of the platinum sensor/heaters. The Sierra MFM uses a constant current source to provide heat to the heater/sensor wire wraps. These wire wraps are comprised of platinum. The resistivity of platinum is very dependent on temperature, with a temperature coefficient of resistivity of typically 0.00385 or 0.00391 per deg C[15]. Thus, as the heater/sensor wrap is heated, its overall resistance will change, in turn changing the power input into the flowstream. In order to model this temperature dependent power input, it is necessary to place the elemental heat input boundary condition on a defined temperature curve, similar to the material property curves. This curve is simply defined using the temperature coefficient of resistance of platinum, 0.385/deg C, and linearly increasing the elemental heat input with the subsequent increase in temperature. In order to map this dependence, it was first necessary to fix the elemental heat input, based on experimental determinations of the current and voltage drop across each heater, as presented in Chapter 3. Finite element modeling was then conducted at the no-flow condition, to determine the temperature of the heater elements based on this constant power loading. A temperature dependent curve could then be defined, based on the no-flow temperature condition, the temperature coefficient of resistance of platinum, and the experimental determination of no-flow heater power consumption.

Table 5-1. Thermophysical Properties of Nitrogen[16].

Temperature (K)	*Density* (kg/m^3)	*Specific Heat* (J/kg*K)	*Viscosity* (uPoise)	*Temperature* (K)	*Thermal Conductivity* (w/m*K)
270	1.25	1041	165.18	**223.15**	.02052
280	1.20	1041	169.72	**273.15**	.02386
290	1.16	1041	174.26	**293.15**	.02554
300	1.12	1041	178.80	**323.15**	.02763
350	0.96	1042	201.50	**373.15**	.03056
400	0.84	1045	224.20	**423.15**	.03315
450	0.75	1050	246.90		

Table 5-2. Thermophysical Properties of Argon[17].

Temperature (K)	*Density* (kg/m^3)	*Specific Heat* (J/kg*K)	*Viscosity* (uPoise)	*Temperature* (K)	*Thermal Conductivity* (w/m*K)
270	1.78	521	206.56	**223.15**	.0134
280	1.72	521	213.60	**273.15**	.01633
290	1.66	521	220.64	**293.15**	.01758
300	1.60	521	227.68	**323.15**	.01884
350	1.37	521	262.88	**373.15**	.02177
400	1.20	521	298.08		
450	1.07	521	333.28		

Table 5-3. Thermophysical Properties of Helium[18].

Temperature (K)	*Density* (kg/m^3)	*Specific Heat* (J/kg*K)	*Viscosity* (uPoise)	*Temperature* (K)	*Thermal Conductivity* (w/m*K)
270	0.18	5193	185.40	**223.15**	.12386
280	0.17	5193	190.04	**273.15**	.14363
290	0.17	5193	194.68	**293.15**	.15119
300	0.16	5193	199.32	**323.15**	.16049
400	0.12	5193	245.72	**373.15**	.17038
500	0.10	5193	292.12		

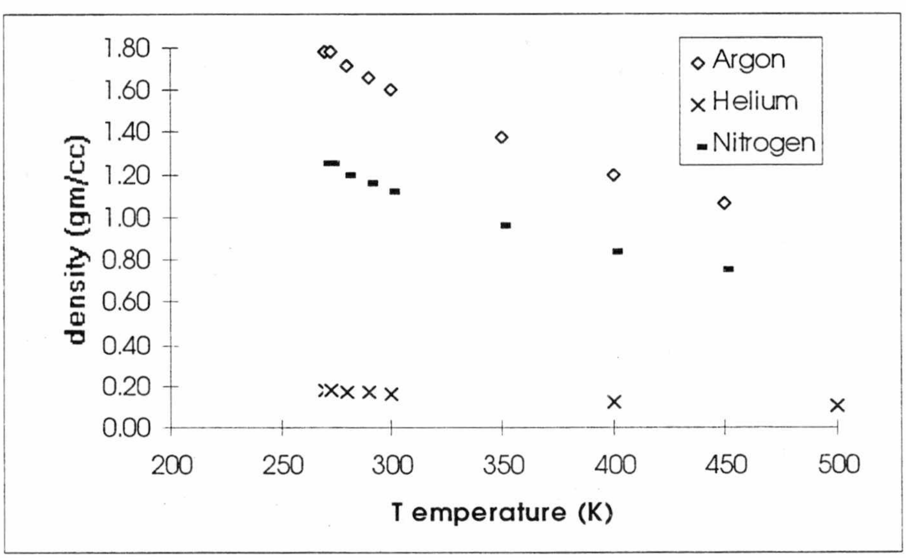

Figure 5-4. Temperature Dependence of Density for Test Gases.

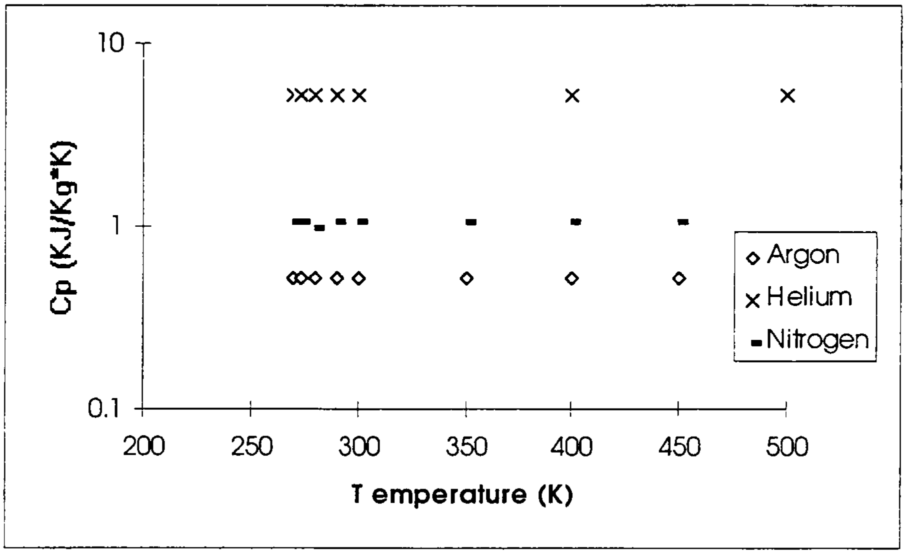

Figure 5-5. Temperature Dependence of Thermal Heat Capacity of Test Gases.

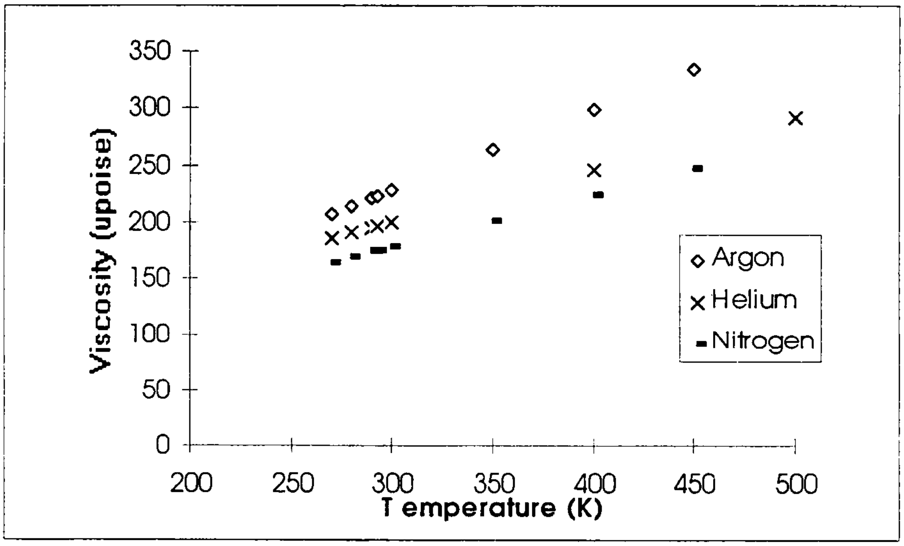

Figure 5-6. Temperature Dependence of Viscosity for Test Gases.

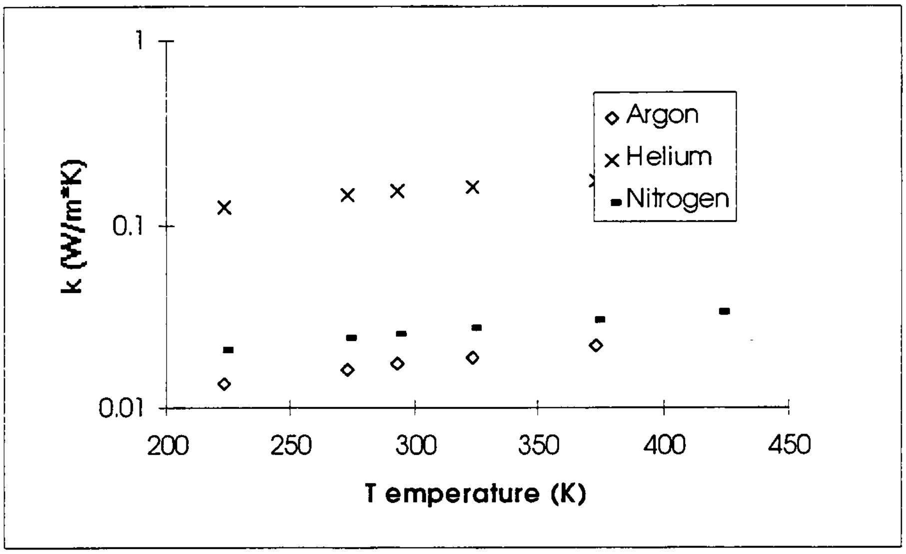

Figure 5-7. Temperature Dependence of Thermal Conductivity of Test Gases.

5.8 MESH CONVERGENCE STUDIES

As discussed in Section 3, it is necessary to conduct a mesh convergence study on both components of the finite element model of the MFM in order to determine if numerically valid results are being obtained for each portion of the model.

In order to determine whether an adequately refined mesh is being used, it is necessary to look at the quantitative error estimate of the approximated solution, and evaluate the change in this error estimate with subsequently refined meshes. It can be shown that, for an adequately meshed problem of bilinear basis, the slope of the log of the error estimate with respect to the log of the measure of the decreasing mesh is 2. [19]

Given two subsequently doubled mesh refinements, Baker provides a formulation for the approximate error in the finer grid solution as[19]

$$e^{h/2} = \frac{\Delta T^{h/2}}{2^{2k} - 1}$$

Equation 5.1

where $\Delta T^{h/2}$ denotes the computed difference in the approximate solutions of the subsequently doubled mesh refinement, and k denotes the basis of the elements of the mesh. For the bilinear element employed in the two-dimensional axisymmetric models of this thesis, k is equal to 1.

Equation 5.1 may be used to verify if a mesh is adequately refined to place the solution data on the convergence curve which corresponds to the model basis. To do this, the volumetric flowrate through the capillary sensor is determined for subsequently doubled mesh refinements, and tabulated as Q1. The difference between subsequently refined solutions is then computed and tabulated as ΔQ1. From this information, the error for the respective mesh refinement is determined and added to the solution data to obtain T_{exact}. When the mesh refinement is adequate, a fairly consistent exact solution will be calculated and that specific meshing will give valid solution data, for which the error may be correctly estimated. Table 5-4 presents this data for nitrogen convergence of the capillary sensor flowpath, in a format consistent with Baker and Pepper[19]. As demonstrated, by the M=4, and M=8 meshing, an adequate mesh has been refined, to place the finite element data on the convergence curve for bilinear elements. Data may be employed using these refinements for accuracies better than 0.01% of reading, as indicated by the error with respect to the finite element estimated Q1.

Unlike the fairly straight path of the capillary sensor flowtube, the annular bypass flowpath proved much more difficult to model using finite element analysis. For helium, acceptable mesh refinement was achieved which indicated acceptable convergence to a useful solution. However, for the higher flowrates of argon and nitrogen, acceptable numerical convergence was not acquired even upon reaching mesh refinements requiring several hours to simulate. The probable cause of this convergence problem is that

Table 5-4. Mesh Convergence for Capillary Sensor Flowpath.

Mesh	*M*	l_e	*Q1*	*ΔQ1*	$e^{h/2}$	$T_{exact}(est)$
Ω^h	1	1	19.6057	1.755884	0.484689	20.09039
$\Omega^{h/2}$	2	0.5	17.84982	0.301818	0.094804	17.94462
$\Omega^{h/4}$	4	0.25	17.548	0.017406	-0.01284	17.53516
$\Omega^{h/8}$	8	0.125	17.53059	0.055921	0.019291	17.54988

adequate downstream distance is not employed within the bypass model to validate the assumption of a constant pressure boundary condition at the downstream surface. This, with an invalid boundary condition, the model data is unable to meet all the specified conditions and convergence is not achieved.

In response to the difficulty in achieving mesh convergence for the annular bypass flowpath, this investigator decided to analytically determine the flowrate within the bypass with given pressure drops across this flowpath. Temperature distribution within this portion of the flowmeter is relatively uniform, with inlet flows at approximately 290 degrees Celsius and the outer walls of the device being only 10 degrees warmer. Runs with helium, which did achieve convergence, readily indicated that the flow temperatures readily came into equilibrium with the prevailing wall temperatures, which approached the values of the outer walls of the meter. Further, significant property variations do not occur within this limited temperature range for the gases being studied.

Due to the relative invariance in properties at the given fluid temperatures of the annular bypass, it was decided to model bypass flow verses pressure using fundamental pressure/flow relationships of fluid mechanics.

5.9 ANALYTICAL MODELING OF THE BYPASS ANNULUS

Due to its simple geometry, and relatively invariant fluid properties, the bypass annulus may be modeled quite simply using fundamental pressure/flow relationships. The portion of the bypass which runs parallel to the capillary sensor flowtube, and thus experiences the same overall pressure drop can be subdivided into 5 individual pressure reducing sections. The first section is an annular bypass which is defined by the outer walls of the annular bypass flowpath, and the inner walls of the upstream portion of the annular plug, which has a smaller radius than the main flow reducing portion of the plug. Following this section, a minor pressure reducing region is comprised of a constriction in the flow from the upstream annulus to the more restricted downstream annulus. This downstream annulus is the primary pressure reducing component of the bypass flowpath; it was described and given a preliminary evaluation in Chapter 4. Following this annulus, another minor pressure loss is caused by the sudden expansion of the flowpath out of the annulus and into a tube flow region. These five sections are presented in Figure 5-8.

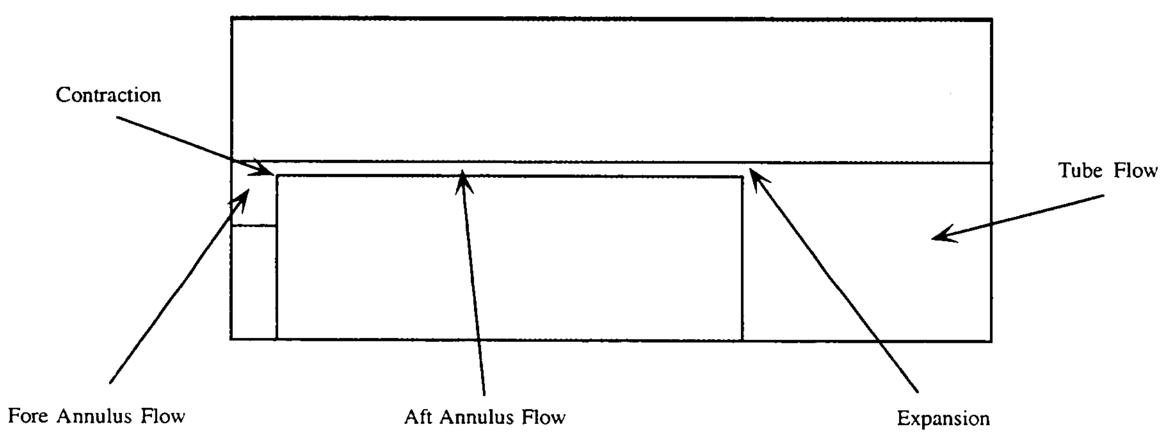

Figure 5-8. Pressure Reducing Components of Bypass Annulus.

White presents a good overview of the analytical determination of pressure drop for these regions[20]. As developed in Chapter 4, for the annular regions, the pressure drop can be expressed in terms of the volumetric flowrate, viscosity, and geometry of the flowpath, and is written as

$$\Delta P_{annulus} = \frac{8\mu LQ}{\pi(R^4 - (\kappa R)^4 - \frac{(R^2 - (\kappa R)^2)^2}{\ln(R/\kappa R)})} \qquad \textbf{Equation 5.2}$$

where the L corresponds to the axial length of the section being evaluated as annular flow.

Similarly, the pressure drop in the tube portion of the flow is represented as

$$\Delta P_{tube} = \frac{8\mu LQ}{\pi R^4} \qquad \textbf{Equation 5.3}$$

The pressure drops due to flow contraction and expansion are considered minor losses, since they typically do not represent a significant amount of pressure drop to the overall total in the system. Commonly, they are evaluated in terms of a loss coefficient, K. In keeping with the notation consistently used throughout this thesis, the loss coefficient will be represented as K_L. The loss coefficient is a dimensionless parameter, which expresses the head loss of the flow in ratio to the velocity component, or

$$K_L = \frac{h_m}{V^2/2g}$$ **Equation 5.4**

Rewriting this in terms of the pressure drop caused by the change in flow and the volumetric flowrate gives

$$\Delta P_{\text{constrict/expand}} = \frac{K_L \rho (\frac{Q}{A})^2}{2}$$ **Equation 5.5**

where the loss coefficient may be determined either through experimentation or by previously published data. White tabulates loss coefficients for several scenarios, including sudden entrance and exit loss effects, where the coefficient ranges from 0 to 1, as well as valves, elbows, and tees where the loss coefficient can be very large, i.e. up to 120 in a partially opened globe valve.

Through summation of each individual pressure reducing component of the annular bypass, an overall expression relating the pressure drop across the annulus and the volumetric flowrate through the annulus can be derived,

$$\Delta P = \Delta P_{\text{foreannulus}} + \Delta P_{\text{constrict}} + \Delta P_{\text{aftannulus}} + \Delta P_{\text{expansion}} + \Delta P_{\text{tube}}$$ **Equation 5.6**

where individual expressions for each component's pressure drop based on section geometry and flowrate may be substituted.

In order to employ this analytical solution, it is necessary to determine the appropriate loss coefficients for the sudden contraction and sudden expansion components of the overall pressure drop.

Although some published data exists regarding loss coefficients for different geometries, it is difficult to correlate this data specifically with the problem at hand. The loss coefficient, however, can be initially estimated by realizing that the annular insert acts very much like a partially opened needle valve in the flow path. White's tabulation of valve loss coefficients place typical valves in the regime of one to ten[20]. Unfortunately, this is a significant variation, and further data is required to narrow in on the actual loss coefficients present in this system.

Fortunately, although mesh convergence was not good for the general case of flow modeling within the bypass, the finite element modeling of the annular bypass yielded numerically reliable data for the single case of helium flow. This successful modeling allows for the development of a relationship between the pressure drop across the annular bypass flowpath, and the volumetric flowrate through this path. Using this numerically generated data, the known pressure drop and volumetric flow variables may be used in a set of equations based upon Equation 5.6 to determine a best-fit loss coefficient for the contraction and expansion components of the flowpath. This same loss coefficient may then be employed in analytical modeling, using Equation 5.6, to determine the pressure drop/flow relationship for other gases.

5.10 SUMMARY OF MODELING DATA

Using the finite element modeling strategy presented above, the pressure drop to flow relationship in the annular bypass was determined for helium gas. In addition, the pressure to flow and temperature relationship was also determined for helium within the capillary sensor tube. This data is summarized in Table 5-5 for discrete overall pressure drops across the system.

As a preliminary cross-check, it is interesting to compare the temperature/flow relationship in the capillary flowtube sensors. Figure 5-9 presents the axial temperature profile beginning at the start of the upstream sensor and ending at the end of the downstream sensor. Temperature profiles are presented for a variety of flowrates through the capillary tubing to indicate the skewing of the thermal profile due to the convection of heat downstream in the flowstream. The data presented correlates well with expected temperature profiles as provided by John Olin, President of Sierra Instruments, in a telephone conversation[3]. Similar data is obtained with other gases, at the full range of flow rates which occur through the MFM.

With this corroborating information regarding the temperature profiles within the flow sensor, the finite element generated data was viewed with heightened confidence. Returning to the evaluation of the analytical solution of the bypass, the finite element data for helium allowed for the determination of an overall loss coefficient for the contraction and expansion effects within the annular bypass. This was determined by least squares fitting of the finite element generated pressure and flow relationship in the bypass section, with variation of the loss coefficient parameters for a best fit. Using this procedure, the loss coefficient was determined to be 2.75. Utilizing this coefficient, the analytical solution matched the finite element generated pressure to flow relationship to better than 1% throughout the flow range.

Knowing the loss coefficient for minor loss effects in the annular bypass, analytical solutions for the pressure to flow relationship within the annular bypass was determined for nitrogen and argon, based on fluid properties of these gases at 300 degrees Celsius. Finite element modeling was used to provide the respective pressure to flow and temperature relationship for these gases within the capillary sensor flowpath. This data is summarized for nitrogen in Table 5-6. Table 5-7 summarizes this data for argon. Figure 5-10 presents the Reynolds Number within the sensor tube for the test gases at various average system pressures referenced to the total system pressure.

Table 5-5. Finite Element Model Generated Data For Helium.

Pressure (*Pa*)	Q_{bypass} (*sccm*)	Q_{sensor} (*sccm*)	ΔT_{sensor} (*deg C*)
10.00	373.14	3.49	1.534
20.00	742.88	6.99	3.053
30.00	1109.29	10.49	4.564
40.00	1472.48	13.99	6.060
50.00	1832.51	17.49	7.539
60.00	2189.48	20.99	8.996
70.00	2543.45	24.49	10.427
80.00	2894.51	27.99	11.828

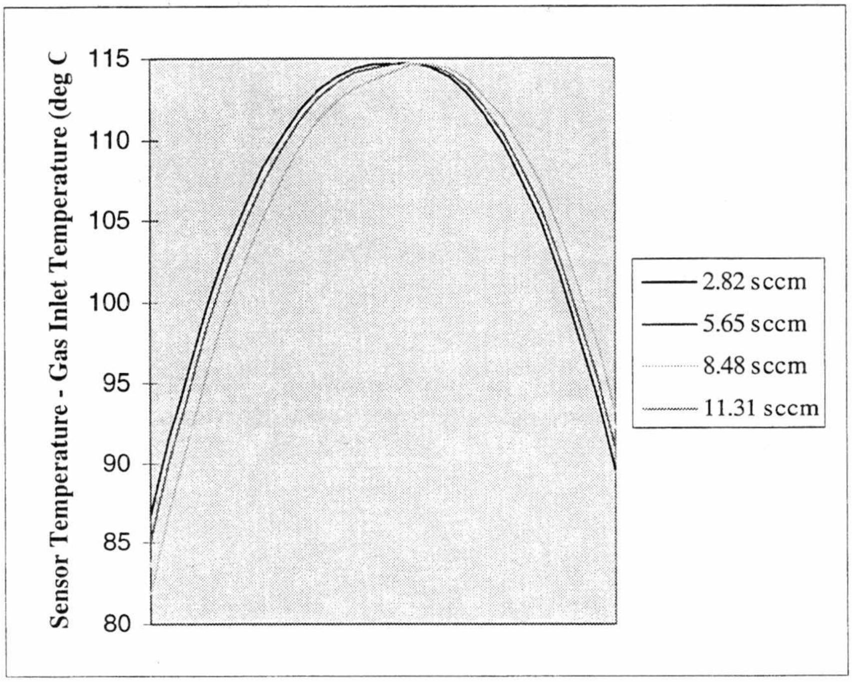

Figure 5-9. Axial Thermal Profile in Capillary Sensor at Various Helium Flowrates.

Table 5-6. Finite Element and Analytical Data For Nitrogen.

Pressure *(Pa)*	Q_{bypass} *analytical* *(sccm)*	Q_{sensor} *FE* *(sccm)*	ΔT_{sensor} *FE* *(deg C)*
5.00	204.87	1.93	1.20
10.00	402.16	3.86	2.38
20.00	777.06	7.73	4.72
30.00	1129.51	11.59	6.99
40.00	1463.19	15.44	9.16
50.00	1780.78	19.27	11.20

Table 5-7. Finite Element and Analytical Data for Argon.

Pressure *(Pa)*	Q_{bypass} *analytical* *(sccm)*	Q_{sensor} *FE* *(sccm)*	ΔT_{sensor} *FE* *(deg C)*
10.00	317.20	2.97	1.32
20.00	615.05	5.95	2.64
30.00	896.72	8.92	3.93
40.00	1164.60	11.89	5.19
50.00	1420.53	14.85	6.43
60.00	1665.97	17.79	7.63
70.00	1902.13	20.73	8.78
80.00	2129.97	23.67	9.87

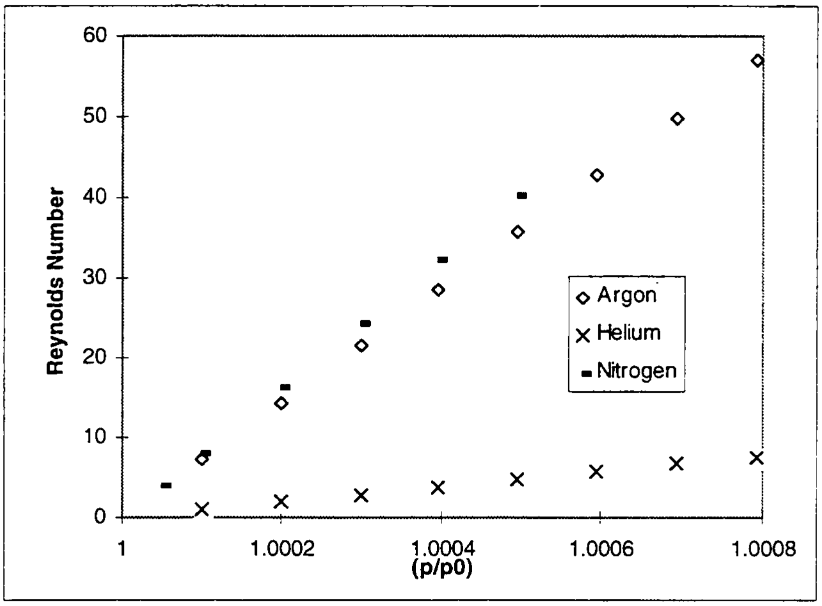

Figure 5-10. Reynolds Number vs Pressure/Ref. Pressure for Test Gases.

6. EXPERIMENTAL VALIDATION

6.1 AN OVERVIEW OF CALIBRATION METHODOLOGIES

Validation of the finite element/analytical model of the Sierra Model 830D-L-7-V1-OK mass flow meter, as developed for this thesis, was performed by actual experimental determination of the gas correction function for various gases. In order to perform this determination, it is necessary to compare the flow indication of a test flowmeter against a known calibration standard, obtaining calibration curves for the reference gas, i.e. nitrogen, and for the gas whose correction function is to be determined. With this information, it is possible to determine the indication of the flowmeter for a known flow of the reference gas, nitrogen. The calibration data for the test gas then allows for the determination of the actual amount of test gas which flows for the same indication by the test flowmeter. Thus, the ratio of test gas flow to nitrogen flow, or the k-factor, may then be determined throughout the test meter's range of indicated flows.

ORNL maintains a diverse array of flow calibration systems which may be utilized to determine the gas correction function. In the flow regime of typical mass flow meters and controllers, i.e. up to 5 standard cubic feet per minute, calibration systems for bulk fluid flowrate determination are typically based on timed collection techniques[21]. Examples of these techniques include mercury-sealed piston devices, pressure-rate-of-rise systems, and direct gravimetric techniques. Perhaps easiest to employ is the mercury-sealed, piston-rate-of-rise test, as presented in Figure 6-1. In this calibration methodology, a variable volume piston chamber is connected downstream of the device-under-test in order to collect the gas which flows through the system. By accurately measuring the change in volume of collected gas over a measured time interval, the actual volumetric flowrate of gas may be determined. Pressure and temperature corrections may then be applied to standardize the actual flowrate to a standard flowrate, based upon conventionally accepted reference pressure and temperature conditions. In theory, flow calibrations of

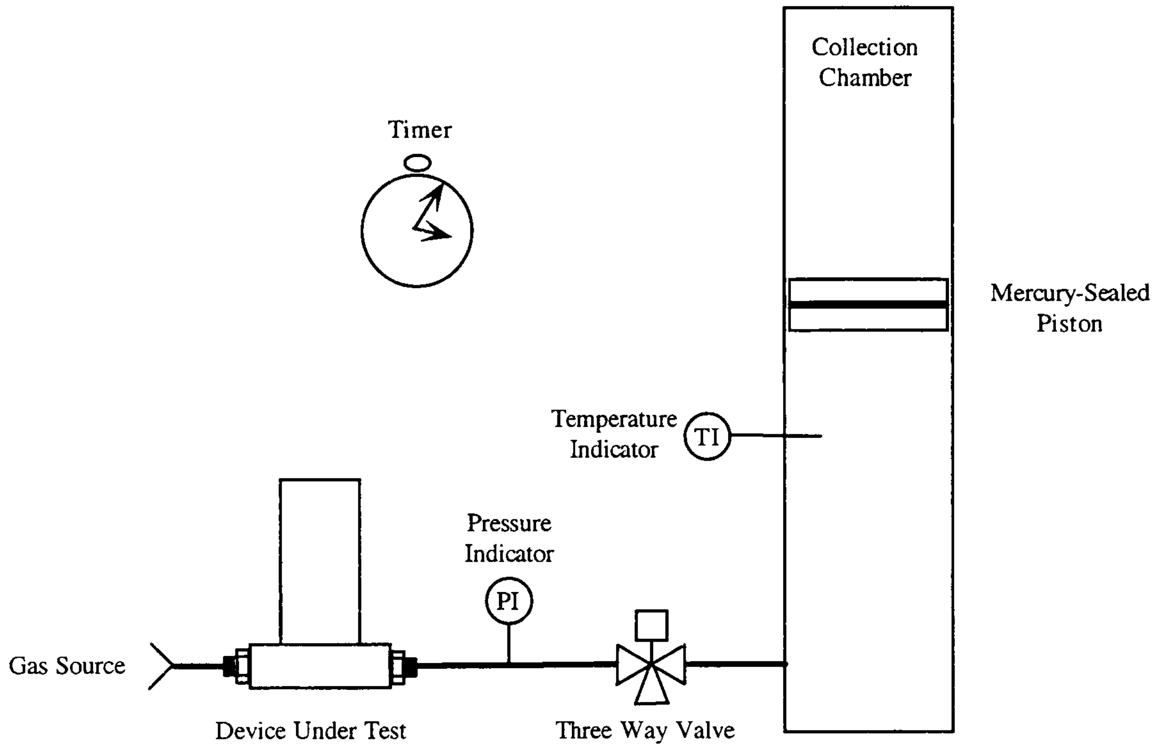

Figure 6-1. The Piston Rate-of-Rise Calibrator.

accuracies approaching 0.15% of reading may be obtained using piston-rate-of-rise systems[21], with the sources of uncertainty being dominated by inaccurate knowledge of cylinder volume, operator error in timing actuation, and inaccurate pressure and temperature corrections. Typical implementations, however, do not perform to this level of accuracy and the general technique is normally accepted to a level of ~0.50% of reading accuracy[22].

The piston rate-of-rise system offers a convenient means of performing flow calibrations, and thus determining gas correction functionalities, at a fairly high level of accuracy. However, the use of this calibration technique is limited to those gases which do not pose significant health or safety risks, i.e. those gases which are often referred to as "benign". As the potential exists for gas release past the mercury seal, the inherent nature of the piston rate-of-rise assembly and its mercury-sealed piston make it a device which is unsafe for toxic, corrosive gas calibrations. For these potentially dangerous calibration scenarios, systems capable of safely handling toxic, corrosive gases must be employed.

One calibration methodology suitable for use with toxic and corrosive process gases is the pressure rate-of-rise, or pressure-rate-of-decay technique. Using this technique, process gas is either discharged or collected into a pressure cylinder of known volume. To perform a mass flow measurement, the change in system pressure within the volume and the temperature change of the system are evaluated over a measured period of time. A mean rate of gas flow for the test period may then be computed. Unlike the variable-volume, piston chamber method, the pressure-rate-of-rise test may be implemented such that it may safely handle toxic, corrosive gases. The cylinder must be made strong enough such that the known volume of the vessel does not change due to the significant pressure changes required to obtain reasonable levels of accuracy. In turn, the strength of the vessel is typically adequate for the safety issues involved in process gas collection. Further, provided all required temperature and pressure instruments are implemented into the vessel, the system lends itself to safe gas handling since the piping of the system may be completely contained without the requirement for "make-and-breaks" during the measurement. Nonetheless, although the pressure-rate-of-rise methodology is conducive to process gas handling, it is by no means the method of choice for mass flow controller accuracy evaluation. In general, this methodology is prone to significant inaccuracy. As the method requires the measurement of pressure, temperature, and volume, uncertainties of each of these parameters cumulatively adds to the overall uncertainty budget. Two of these parameters, temperature and volume, are particularly prone to error. The former is prone to error due to significant thermal gradients which develop in the system during rapid filling or discharging of the pressure vessel. The latter is prone to error due to unaccounted changes in system volume due to process gas induced corrosion or deposition build-up of the vessel walls.

Another methodology suitable for process gas calibrations is the gravimetric technique. As their name implies, gravimetric techniques measure mass flow by directly accounting for the change in mass of a control volume over a given time period. Similar to the pressure-rate-of-rise system, gravimetric systems employ a collection or discharge vessel. However, unlike the pressure method, the gravimetric system does not directly require the monitoring of volume, temperature, or pressure. Instead, it is only required to weigh the vessel in order to determine the mass of gas collected into or discharged from the vessel over a known time period. From this simplification, it becomes apparent that the gravimetric technique has the potential to be very accurate; much more so than the pressure method, as it is no longer constrained by the cumulative inaccuracies of the pressure, temperature, and volume measurements. In practice, however, the gravimetric technique may present many difficulties. Similar to the pressure method, the collection vessel must be very strong in order to safely handle corrosive process gases. Even with new, emerging materials, strength in today's world implies weight. From this arises the primary difficulty of the gravimetric method, i.e. the necessity to measure small changes of mass due to gas collection/discharge against a relatively massive "tare" weight of the collection vessel itself. In the past, this difficulty has caused the gravimetric technique to be laborious to implement. Within this method, very accurate mass flow rates may indeed be determined, however calibration run times must be very long, in order to collect enough gas to determine an accurate level of mass change above the large "tare" weight of the vessel. The measurement is further aggravated by the typical requirement of disconnection of the vessel from the system piping in order to isolate its mass during the weighing process.

Dr. Carl Remenyik, a senior staff researcher at the Oak Ridge National Laboratory, has developed a new style of gravimetric calibrator which addresses many of the limitations of previous gravimetric setups[23]. This instrument, simply called the "gravimetric calibrator", is depicted in Figure 6-2. It is comprised of a large, 20 liter collection vessel made of corrosion resistant inconel. The vessel is rigidly suspended from a mass-measuring load cell at the center of mass of the system. Gas enters and exits the collection vessel from a single torsional capillary tube at one end of the collection vessel. To address the issue of large vessel tare weight, Dr. Remenyik virtually removed the large vessel weight by submerging the entire collection vessel in a water bath. By careful adjustment, the collection system may be made to be only slightly heavier than neutral buoyancy, such that the percentage change in mass of the system due to gas collection is a much more significant portion of the overall mass of the system. This change allows accurate mass flow calibrations to be conducted virtually "on the fly", no longer requiring long collection times in order to collect measurable amounts of gas. In addition to this major improvement to the gravimetric methodology, Dr. Remenyik also designed the weighing system of the calibrator such that the collection vessel does not require disconnection from the system in order to determine the collected mass. This improvement, highly advantageous for process gas work, is realized by connecting the collection vessel to the process gas piping via a torsional capillary tube. In comparison to the collection vessel's stiff suspension system, which is directly connected to the weighing system, the torsional capillary imparts negligible moment arm to the system, and thus does not significantly affect the weighing process.

Although the gravimetric calibrator sounds like a fairly simple calibration methodology, implementation of the system requires overcoming several hurdles. First, the buoyancy of the system has a significant impact on the measurement process. If the buoyancy of the vessel changes during the measurement process, it will have an affect unaccounted for on the measurement, generating errors. By submerging the collection vessel in water, the buoyancy of the system is coupled to the density of the water bath, which is dependent upon the temperature of the bath. Density variations within the bath are reflected as variations in the overall vessel weight, as provided by the load cell indication of the system. Thus, the system requires fairly consistent environmental control, in order to maintain a stable fluid density.

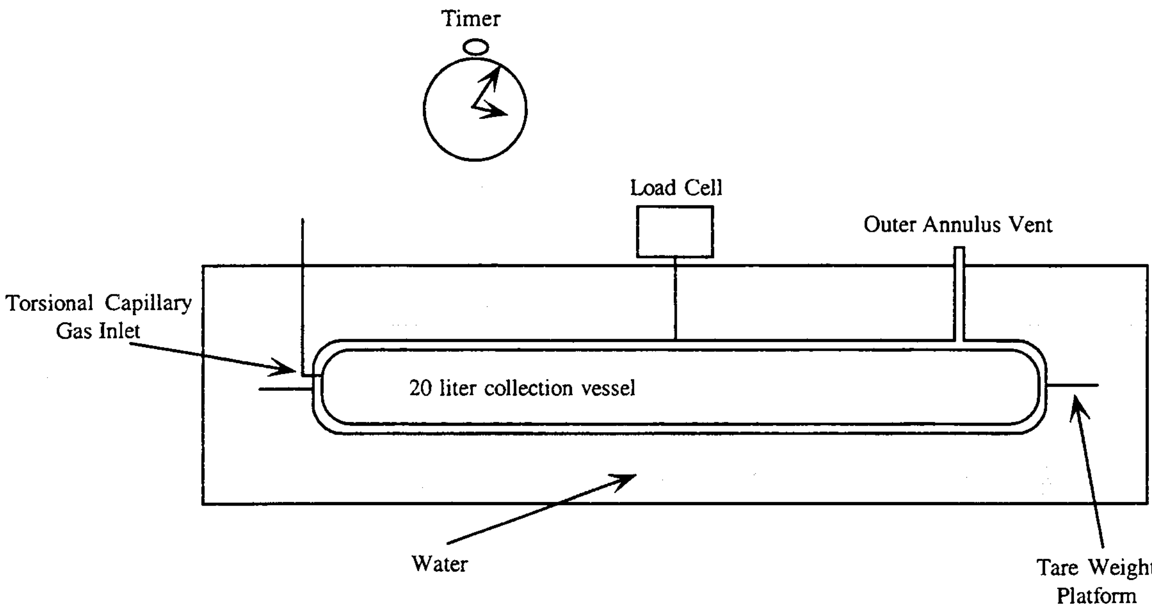

Figure 6-2. The Gravimetric Calibrator.

Ideally, environmental temperature control would be based around the temperature of ~4 degrees Celsius, where the density of water is at a maximum, and the change in density per unit temperature is minimized. At this control point, the stability of the system with respect to temperature variations is maximized. Unfortunately, the current configuration of the system does not allow operation at this ideal control point. Instead, the system is currently operated at a nominal temperature of 20 degrees Celsius, with approximately 1 degree of drift about this setpoint. To compensate for the resultant buoyancy-induced drifting, a no-flow "background" study is conducted prior to each calibration run. By determining the background drift of the system under no-flow conditions due to temperature induced buoyancy effects, and provided this "background correction" does not significantly change during a collection run, the drift may be corrected out of the resultant mass flow indication of the system. Under normal operating conditions, this correction can usually be achieved, as the system has a tendency to slowly follow the long term drift of the surrounding laboratory temperature.

In addition to temperature-induced buoyancy fluctuations of the system, the buoyancy of the gravimetric calibrator initially had a significant pressure dependence. During typical calibration runs lasting from 60 to 300 seconds, approximately 1 to 10 grams of gas are collected over the measured time interval. With the wide range of gases used, pressure change within the vessel during a collection run is typically from 1 to 10 kPa. It was initially felt, due to the strength of the collection vessel, that these pressure changes would not be enough to cause significant deformation of the vessel. In early experiments, however, it was quickly realized that the buoyancy change of the vessel during gas collection was very significant due to deformation of the vessel and the resultant displacement of water. To address this problem, Dr. Remenyik surrounded the collection vessel with an annular shroud which was vented to the atmosphere. This shroud isolates the dimensional variations of the inner collection vessel from the surrounding water bath and thus removes the buoyancy effect caused by pressure deformation of the vessel. As the outer shroud remains at a fairly constant pressure during a timed collection interval, the pressure dependence of the buoyancy is negligible. It is often comically cautioned, however, that the gravimetric system should not be used during periods of tornado and hurricane activity, as the ambient barometric pressure, and thus the pressure within the annular shroud, may experience sudden and violent changes.

6.2 CALIBRATION METHODOLOGY

Although the Oak Ridge National Laboratory maintains the capability of evaluating process gases with its gravimetric calibrator, the gases evaluated for this thesis were specifically chosen to be benign in order to run tests without expensive process gas handling precautions. For this reason, the piston-rate-of-rise device was chosen as the calibrator of choice for this thesis. Configuration of the system, as used for this test, is diagrammed in Figure 6-3.

To conduct a piston-rate-of-rise calibration, the device under test is connected to a gas source of known constituency. Within the semiconductor industry, gases are described in terms of purity as 3-, 4-, or 5-nines purity, which pertain to 99.9%, 99.99%, and 99.999% purity levels. Typically, the purity level of gases are described by the gas supplier with a certification sheet which is packaged with the gas bottle. 4-

nines purity gases where employed during the calibrations of this thesis. A dual-stage regulator at the bottle source was employed to control the delivery pressure of the gas, which was maintained at 15.00 psia, as measured by an absolute pressure gauge which was connected between the gas source and the MFM.

As the devices-under-test for this thesis were mass flow meters, and not mass flow controllers, a means of controlling the flowrate of gas was required. A vernier actuated needle valve was used to regulate gas flowrate, and was located downstream of the MFM. The needle valve provided a consistent flowrate as indicated by the signal output of the MFM, and as verified by repeatability tests against the piston-rate-of-rise flow standard.

The piston-rate-of-rise chamber was located at the end of the calibration system piping, downstream of the MFM and the flow-metering needle valve. A three-way valve is utilized to either vent the gas, or route the gas into the collection vessel during a timed collection interval. This allows for bypassing the collection chamber while the flow is allowed to stabilize through the device under test. Upon stabilization, the three-way valve is actuated to begin gas collection below the mercury-sealed piston. The collection vessel is demarcated with scribed lines which indicate liter-sized incremental volumes. During collection, the piston rises with accumulated gas. For consistency, it is commonly practiced to begin timing of the collection when the upper surface of the mercury-seal passes one of these demarcation lines. Timing is then stopped when this same position passes another demarcation point, upon which a known incremental volume of gas has been collected. In order to minimize the uncertainty due to operator error in actuation of the timing device, it is common practice to run the collection interval for at least 100 seconds. By collecting for at least 100 seconds, operator timer actuation errors, on the order of .1 seconds, are minimized to a timing uncertainty to 0.1%, which is an acceptable uncertainty level for an overall flow uncertainty of 0.5%.

In order to standardize the actual volumetric flowrate of gas, as determined by dividing the total volume collected by the collection time interval, it is necessary to perform pressure and temperature corrections to conventionally accepted reference conditions. For the Sierra mass flow meter, these conventionally accepted conditions are specified by the manufacturer to be a pressure of 14.7 psia and a

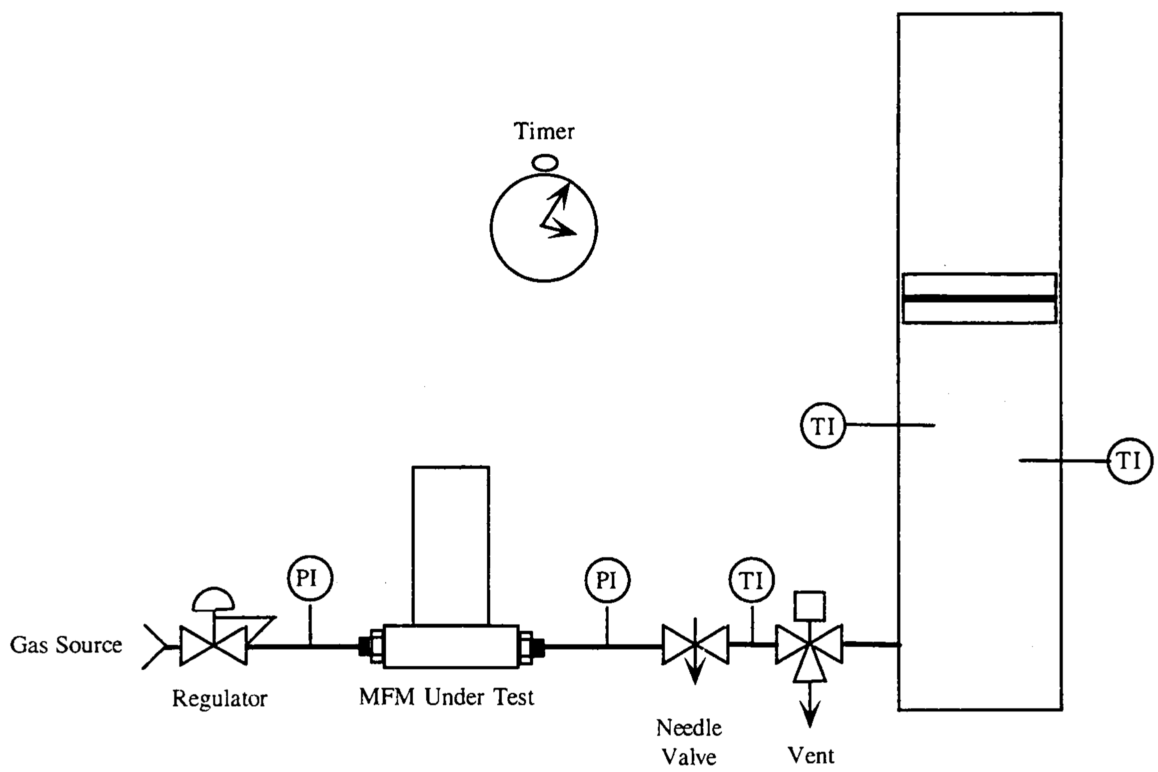

Figure 6-3. Calibration Configuration for MFM Gas Correction Function Determination.

temperature of 70 deg. F. In order to correct to these conditions, the actual operating pressure and temperature must be known. The operating pressure is determined by flowing an amount of gas into the piston chamber, shutting off gas flow from the source, and allowing the piston to "hang" above the collected amount of gas. By measuring the pressure in the gas delivery line, downstream of the MFM and upstream of the collection chamber, the overall pressure within the chamber can be measured. By performing the measurement in this manner, both the prevailing ambient barometric pressure and the pressure added by the weight of the piston upon the collected gas, may be determined. The operating temperature is obtained by measuring the temperature of the walls of the piston chamber, in addition to the fluid temperature of the flowing gas. Data should only be considered valid if there are no significant deviations present between these temperatures, as significant deviations indicate a difference between the gas inlet temperature, and the walls of the piston chamber, and thus an unknown temperature distribution within the collection chamber.

Knowing the prevailing operating conditions, corrections may be applied to adjust the actual gas flowrate to standard conditions. This correction is nothing more than a density correction process, and relates the actual flow at prevailing operating conditions to flow which would be obtained due to the density of the gas at standard conditions. This correction is calculated as

$$Q_s = Q_a \left[\frac{T_s}{T_a}\right]\left[\frac{P_a}{P_s}\right]$$

Equation 6.1

where the subscript, s, corresponds to values at standard conditions, and the subscript, a, corresponds to values at actual test conditions.

One precaution which must always be addressed when performing calibrations with a piston-rate-of-rise system is a pre-testing leak check of the system. If a leak check is not performed, an unknown leak could introduce errors into the measurement by causing the volume of collected gas to be less than is actually flowing through the test device. Fortunately, a leak check is a very trivial procedure with a piston-rate-of-rise assembly. The operator simply fills the collection vessel with an amount of gas which positions the piston in proximity of an incremental volume demarcation. The gas flow is then stopped at the source and the piston is allowed to "float" at the demarcated position. The operator then waits for a time interval equal to the amount of time a normal calibration run would take and insures that the piston does not drop from the marked position. If the piston does not drop, one concludes that the system is leak-proof. If the piston does drop, a leak is present in the piping of the system and must be located. In this event, it is typically easier to plug the vent port of the three-way valve, and slightly pressurize the system upstream of this valve. Without pressurizing the system, it is difficult to identify a leak due to the small pressure difference which exists between the piping and the prevailing barometric pressure of the laboratory. Upon pressurizing the piping, a detergent-based leak detection fluid may be wiped on the piping connections. A leak will be evident by bubbling of the solution in the vicinity of the leak. Connections may then be improved and the piston-float process repeated until the leakless condition is obtained.

7. DISCUSSION OF RESULTS

7.1 EXPERIMENTAL DATA

Using the calibration methodology discussed in Chapter 6, data was collected on the three test Sierra specimens for a variety of safe, non-toxic, non-corrosive gases. These gases, which were chosen mainly for their availability to the author, include nitrogen, helium, carbon dioxide, and argon.

To avoid the potential for contamination by mixing of gases between runs, the system was purged by running the current calibration gas for a period of 1 hour before the collection of any data. Leak checks, as described in the previous chapter, were also performed after making any connection changes to the system piping.

In order to express the data in a form most consistent with the goals of this thesis, data was manipulated to indicate the gas correction factor, or K-Factor, for each gas with respect to nitrogen at each indicated flowrate. Towards this end, nitrogen calibration data was first used to normalize the indication of MFM. In order to normalize the data in this fashion, the nitrogen flow indication of each MFM was mathematically corrected to the actual standard nitrogen flowrate using a least squares fit algorithm. This allows each MFM to be compared with the other test specimens by correcting the calibration error of that MFM as provided by the nitrogen calibration data. As discussed in previous chapters, mass flow meters are typically specified by manufacturers to have inaccuracies of 1% of full scale. However, MFMs are susceptible to change through handling, contamination, and aging of the electronics. As most MFMs are connected into distributed process controllers, and other forms of extensive signal conditioning, it is not uncommon for mathematical calibration corrections to be used to remove the error from the indication of the flowmeter such that actual standard flowrates are known.

Using the correction algorithm, the nitrogen flow indication of each MFM is driven to correspond with the actual standard nitrogen flow, within the uncertainty bounds of the fit. The K-Factor for each MFM, as calculated with respect to the actual nitrogen flow, should then be equal to one. This is indeed the case, as presented in Figure 7-1. In this Figure, the K-Factor is presented at various flowrates, for each of the test specimens. As a reference, the manufacturer published K-Factor is also presented. Error bars are included to indicate the uncertainty of the calibration, which is approximated at 0.5% of reading as previously discussed.

Similar data is presented for argon, carbon dioxide, and helium in Figures 7-2 to 7-4. In each of these cases, the actual flowrate of each of the test gases is divided by the indication of the MFM as corrected to standard nitrogen flow. Thus, the standard flow of the test gas is compared to the standard flow of nitrogen.

As shown in these figures, the experimentally determined K-factors vary with increasing volumetric flow rate, in contrast to the manufacturer's published constant K-factors.

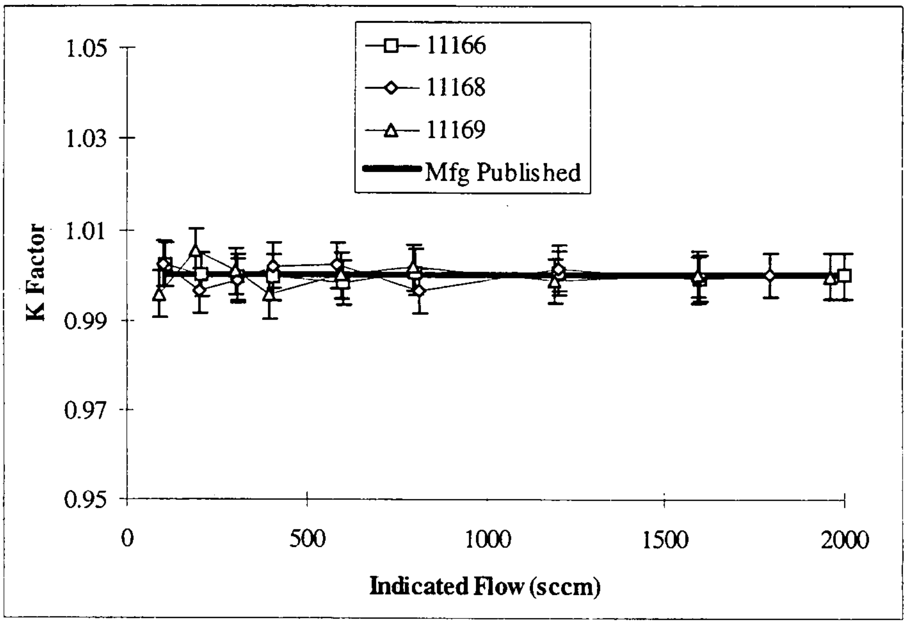

Figure 7-1. Experimentally Determined Nitrogen Gas Correction Functions.

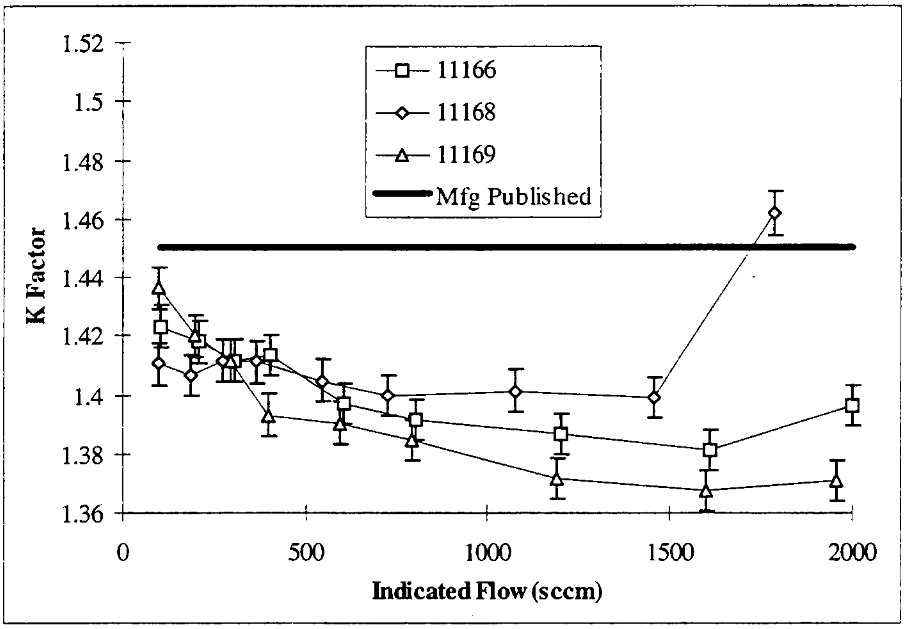

Figure 7-2. Experimentally Determined Argon Gas Corrections Functions.

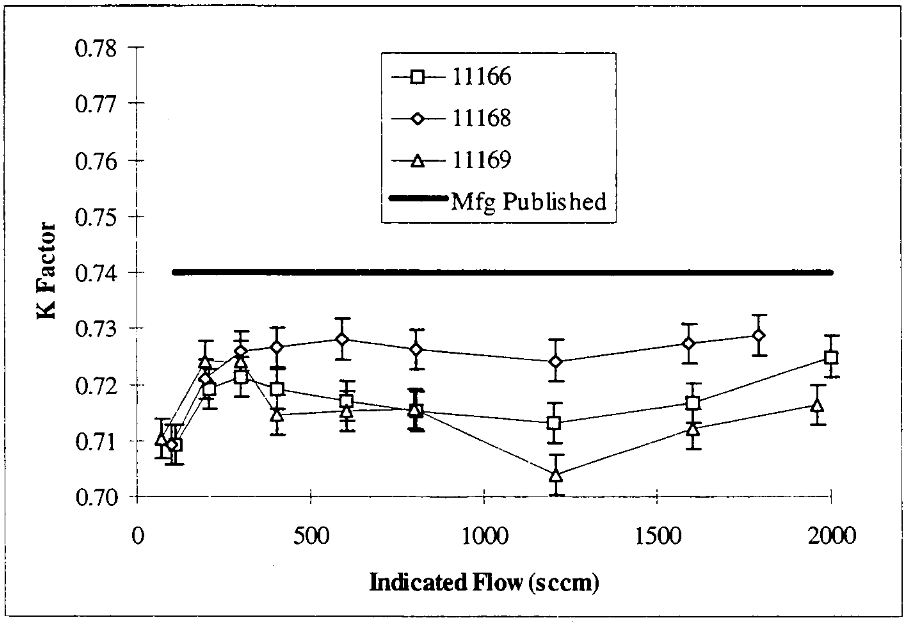

Figure 7-3. Experimentally Determined Carbon Dioxide Gas Correction Functions.

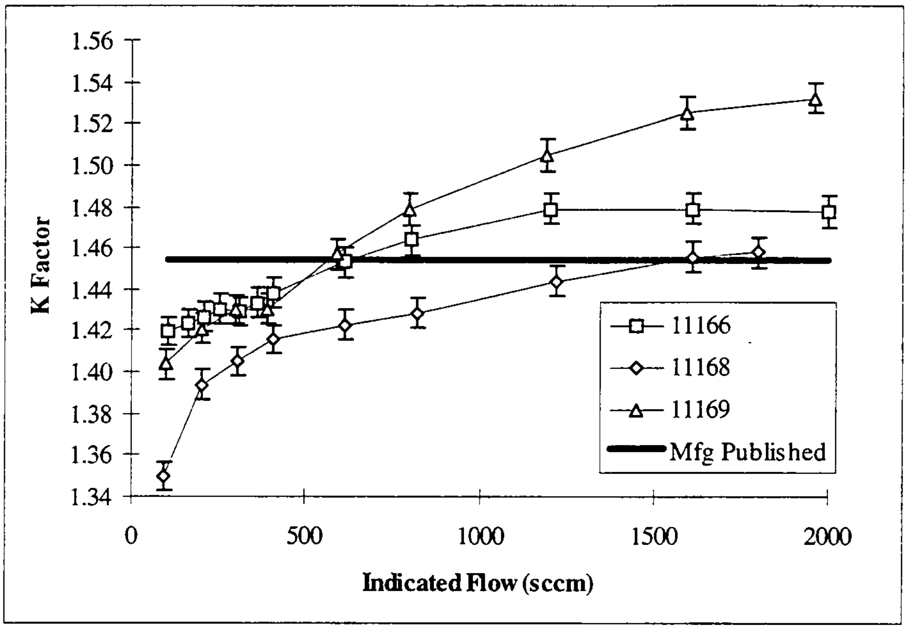

Figure 7-4. Experimentally Determined Helium Gas Correction Functions.

7.2 COMPARISON OF MODEL WITH EXPERIMENTAL DATA

The ultimate validation of a model is to directly compare model generated results with experimental data. Towards the goal of understanding gas correction functions for the Sierra MFM, this comparison is best made by evaluating the resultant modeled gas correction functions with those experimentally determined and presented in the previous section.

Following the discussion in Chapter 5, the model generated gas correction functions are determined by dividing the total volumetric flow through the MFM of the test gas, by the equivalent flow of nitrogen which would generate the same temperature difference within the sensor capillary tube. This can be done by utilizing the model generated nitrogen data, and fitting the total nitrogen flow to the respective temperature difference developed in the capillary flow tube, as tabulated in Table 5-6. This same curve fit may then be employed to calculate the corresponding nitrogen flow for each temperature difference of each test gas flow condition, as tabulated in Table 5-5 and Table 5-7. By dividing this corresponding nitrogen flow into the modeled total flowrate of test gas, a gas correction value is determined at each corresponding nitrogen flowrate. This gas correction value may then be plotted, as in Figure 7-1 through Figure 7-4.

The gas correction functionality was determined for both helium and argon and the results were superimposed to the experimental data. Figure 7-5 presents this information for argon. Figure 7-6 presents the information for helium.

7.3 SENSITIVITY OF MFM TO VARIATION OF PARAMETERS

Although not a perfect fit for all test samples, it is evident from the figures that the model provides a significant improvement to manufacturer suggested values in estimating the gas correction function behavior throughout the MFM operating range. Using the suggested correction factor results in a greater than 5% error in determining the volumetric flowrate of argon in test sample 11169, and approximately 8% error in determining the helium flowrate of test 11168 at the low end of its operating range. Using the model, errors are maintained below 2% for argon for all test specimens, discounting the outlying point of test sample 11168. For helium, the model data fits test sample 11169 to better than 0.5%. Unfortunately, it does not model the behavior of the other two specimens as well, and would result in flow errors of approximately 8% if employed to correct for MFM 11168.

The significant deviation between samples demands some attention to attempt to understand the source or sources of the deviant behavior. Towards this understanding, the model may be employed to evaluate the effect of parameter variation on the performance of the MFM. Using the gas correction factors presented in Figure 7-5 and Figure 7-6 as base references, parameter variation was conducted on the properties of the MFM most sensitive to measurement error. Most susceptible to error and uncertainty, is the measurement of the inner diameter of the capillary sensor flowpath. The measurement employed for the base reference correction factors was an inner diameter of 0.762 mm. In order to make this measurement, a

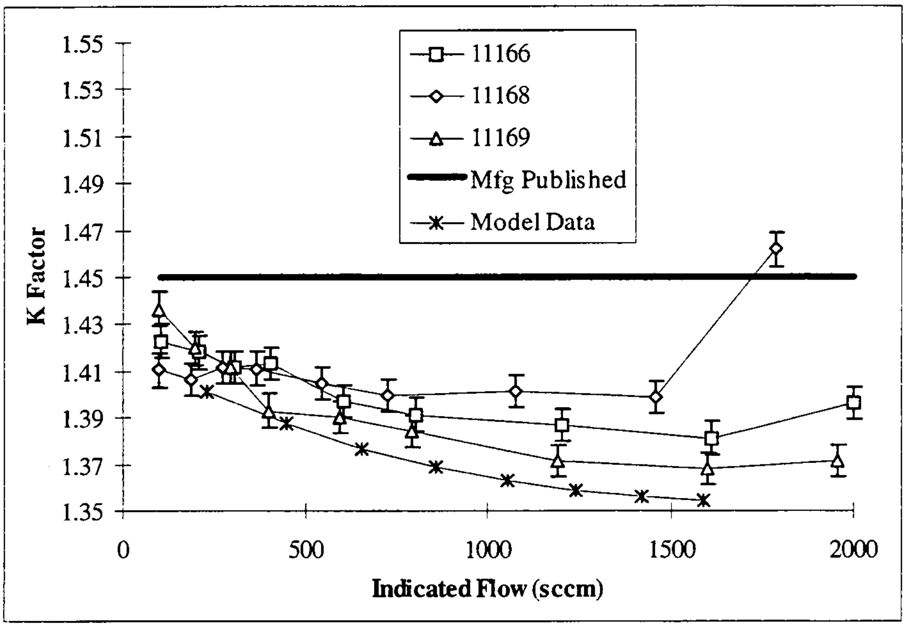

Figure 7-5. Comparison or Argon Model Data with Experimental.

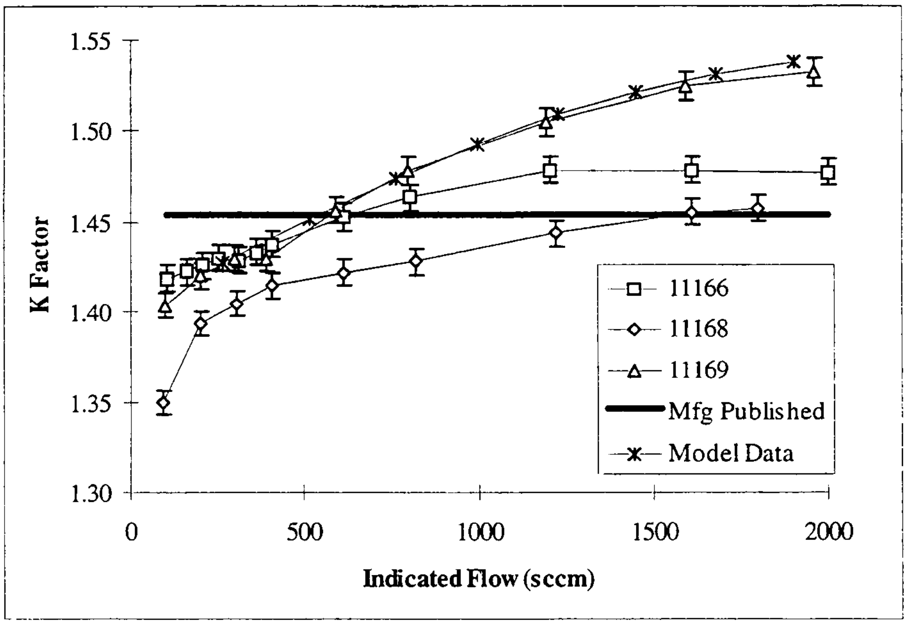

Figure 7-6. Comparison of Helium Model Data with Experimental.

trial and error routine was used in which subsequently larger and larger diameter wires were inserted into the capillary tube, until the wire diameter could no longer fit into the capillary tube. Using this methodology, it is not inconceivable that errors of several hundredths of a millimeter are possible. Further, at this level of machining, it is quite likely that this much variation exists between capillary tubes of test specimens. To evaluate the effect of this error, a 5% reduction in capillary tube inner diameter was modeled.

Another dimensional measurement which was difficult to accurately obtain, was the outer diameter of the annular bypass. The bypass itself could be completely removed from its housing and measured quite accurately, however, to measure the diameter of the outer annulus diameter required placing calipers into the housing, with interference from piping threads at each end of the housing. It is not unlikely that errors as great as 0.1 mm could be realized in measuring the outer diameter of the annular bypass. Manufacturing deviations could also quite likely fall within this level of accuracy, particularly since MFM paths are traditionally electropolished. Electropolishing generates a very smooth surface, with the intent of minimizing surfaces which could be attacked by corrosive process gases. Unfortunately, although electropolishing develops excellent smooth surfaces, the overall thickness of the surface may be highly variable due to the length of the electropolishing process.

Another variable for which a large uncertainty exists is the thermal conductivity of the insulative blanket which wraps the capillary sensor flowtube. As mentioned in Chapter 3, it is difficult to obtain an accurate measurement of this value, as the thermal conductivity of insulation is very dependent on its particular installation, i.e. how tightly the insulation is packed into its housing, etc. It is not unlikely that variations of as great as 10-20% could result in the thermal conductivity of insulation as driven by its particular installation.

Figure 7-7 and Figure 7-8 present the sensitivity of the gas correction curves of the MFMs to variation of the sensor capillary outer diameter, the annular bypass outer diameter and the thermal conductivity of the insulative blanket. As evidenced from these figures, the MFM is fairly insensitive to geometric and thermal variations of the capillary sensor, but is extremely sensitive to variations in the

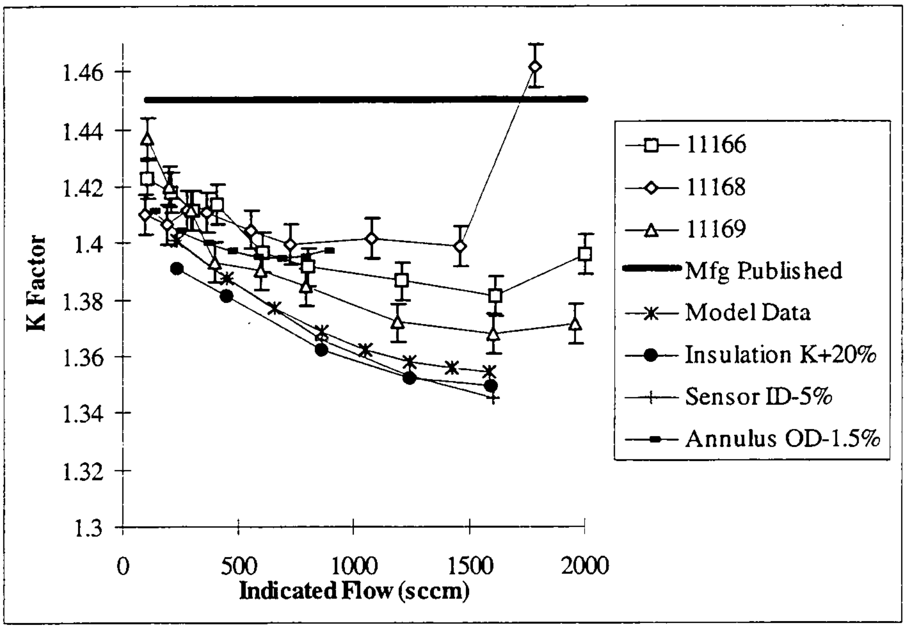

Figure 7-7. Argon Sensitivity of MFM to Variation of Selected Parameters.

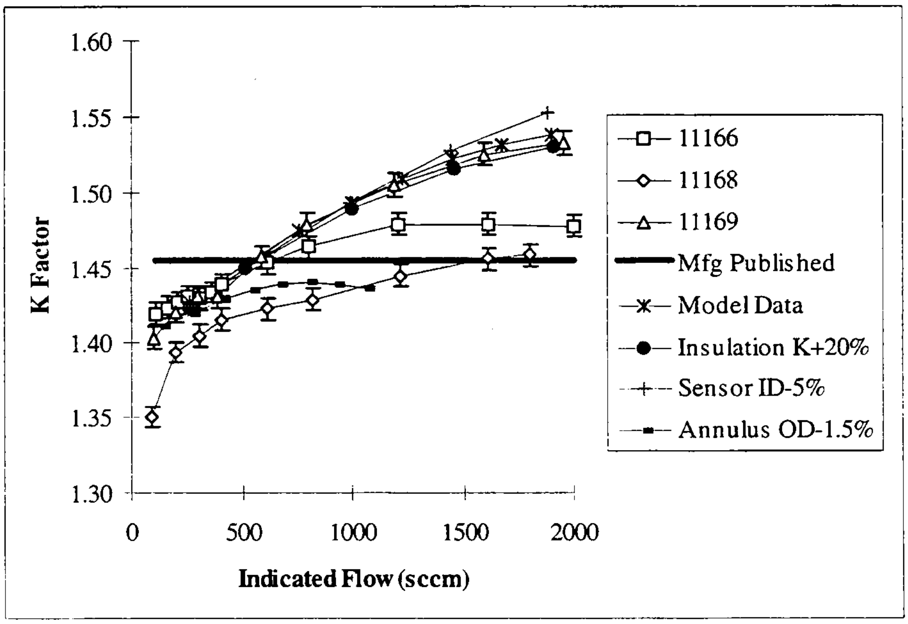

Figure 7-8. Helium Sensitivity of MFM to Variation of Selected Parameters.

geometry of the annular flow bypass. From this information, it is most likely that deviations between the three sample specimens are due to manufacturing variations of the geometry of the annular flow bypass.

7.4 THE SIGNIFICANCE OF MINOR LOSS EFFECTS

In the review of the literature, the source of gas correction function non-linearity was suggested to arise from either of two sources; (i.) from non-linearity behavior within the capillary flow sensor, or (ii.) from variability of the flow splitting ratio between the annular bypass and the capillary flow sensor. It is interesting to evaluate the splitting ratio between the two flow paths, as indicated by results obtained from the model.

Figure 7-9 and Figure 7-10 present the split ratio between the bypass and the capillary sensor flows for the test gases of nitrogen, argon, and helium. For each gas a plot is included where the model either incorporated minor losses due to expansion and contraction in the annular flow bypass, w/ML, or did not incorporate these losses by setting the minor loss coefficient to zero. As evidenced by this graph, minor losses play a significant role in causing unequal flow splitting between the bypass and sensor flowpaths. Indeed, if minor losses were not a factor, flow splitting would remain constant to better than 1% throughout the flow range of the MFMs.

Returning back to our comparison charts of gas correction factors for each of the test gases, it is evident how significant the minor losses of the bypass are upon the gas correction functionality. Figure 7-11 presents the gas correction factor for argon as predicted by the model with and without evaluation of minor losses within the annular flow bypass. Figure 7-12 presents this same data for helium. From these graphs, it appears that by not evaluating minor losses of the annular flow bypass, the gas correction functionality approaches the information provided by the manufacturer, with a bias offset which likely arises from determination of the correction function at different temperatures, and thus differing gas properties.

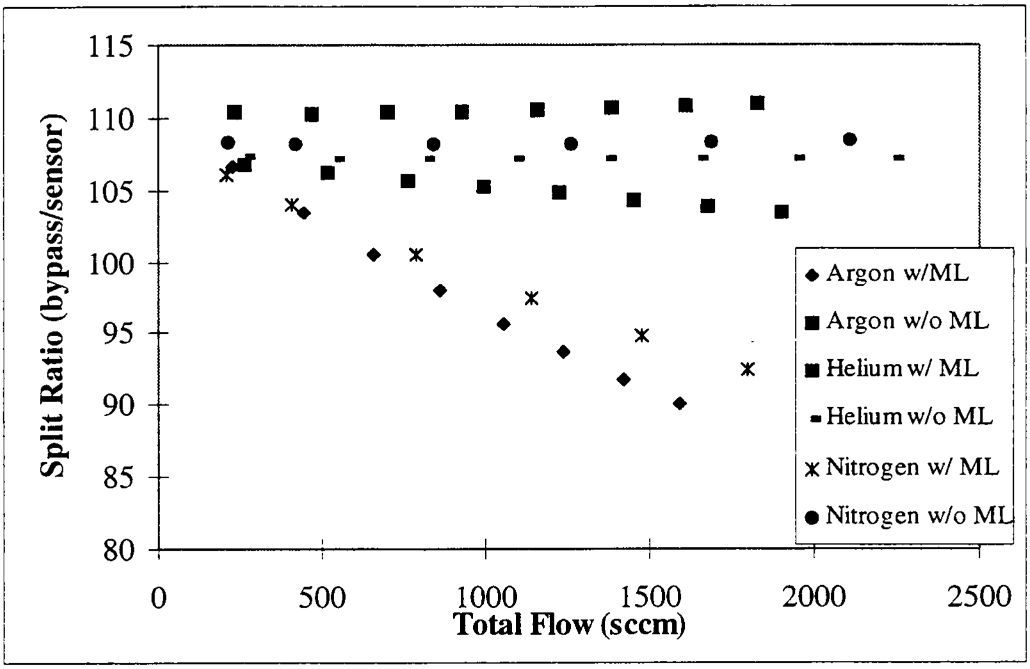

Figure 7-9. Bypass/Sensor Flow Split Ratio vs Total Flowrate for Various Gases.

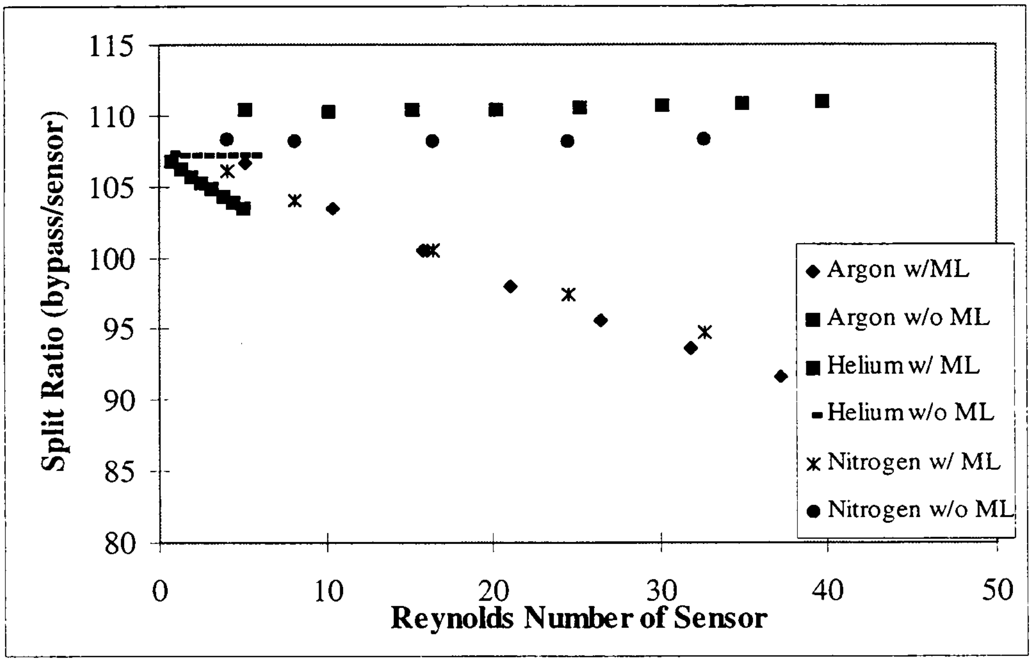

Figure 7-10. Bypass/Sensor Flow Split Ratio vs Reynolds Number for Various Gases.

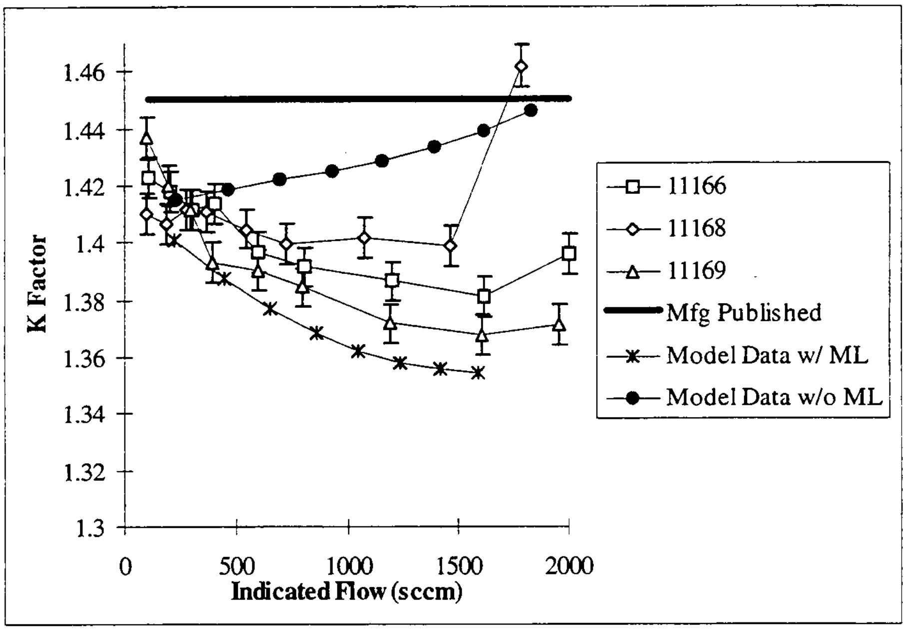

Figure 7-11. Argon Gas Correction Function Dependence on Minor Losses.

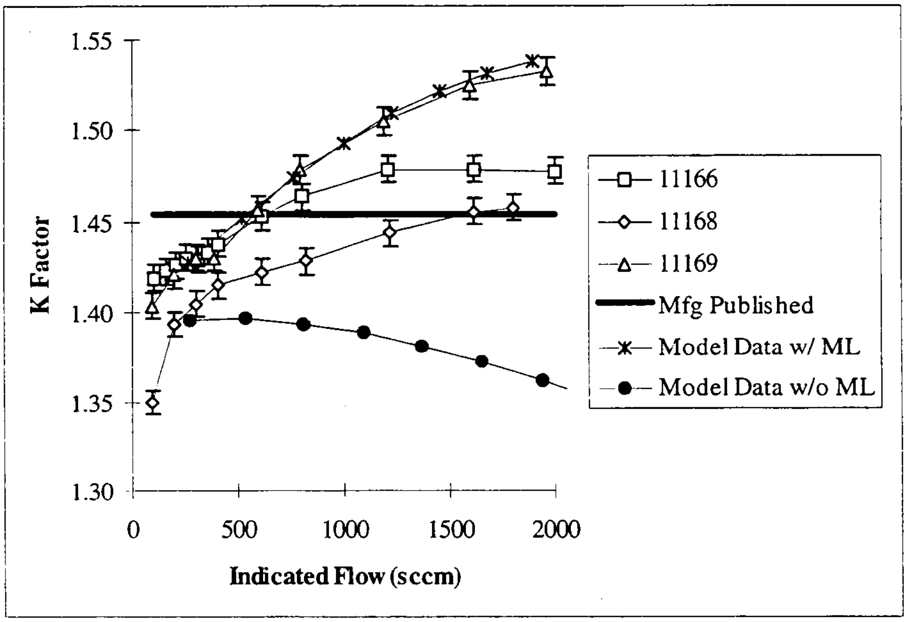

Figure 7-12. Helium Gas Correction Function Dependence on Minor Losses.

In contrast to the significant impact of minor loss effects in the annular bypass, it can be shown that minor loss effects in the capillary flowtube are almost negligible to the overall performance of an MFM. The capillary flow experiences significant contraction and expansion upon entering and exiting the restricted sensor flowpath from the larger upstream and downstream plenum areas. These effects were not incorporated into the finite element model of the capillary flowpath. Further, in order to perform axisymmetric two-dimensional modeling of the capillary flowpath, the 90 degree elbows of the flowpath were also disregarded. However, using the methodology of White previously presented in Section 5.9, it can be shown that each of these minor loss contributions to the overall pressure drop may be treated as negligible.

White presents relationships for the minor loss coefficient with respect to the ratio of the constricted diameter to the larger diameter, d/D, for sudden contraction and sudden expansion effects[20]. For the geometries involved with the transition from the plenum areas to the capillary flow sensor, the d/D ratio falls at the low end of White's relationships, and thus maximize the minor loss coefficient. White presents a maximul sudden contraction coefficient of 1.0, and a sudden contraction coefficient of 0.4. Similar relations are developed for minor loss effects due to the resistance of bends in a flowstream, as experienced in the upstream and downstream portions of the capillary flowpath. These relations are dependent on the curve ratio, R/d, where R represents the radius of the bend, and d the inner diameter of the flowpath. The relations are also dependent on the smoothness of the flowpath, which for our electropolished capillary tube may evaluated as approaching zero. For these conditions, the minor loss coefficient for bends is very small, approximately 0.15.

Based on the velocities obtained in the finite element model of the capillary sensor, the minor loss coefficients as presented by White, and the geometries of the capillary sensor flowpath, the overall minor pressure losses may be evaluated and compared against the total pressure drop of the capillary sensor flowpath. Table 7-1 presents this data for nitrogen. As demonstrated, the minor loss effects of the sensor contribute very little to the overall pressure drop of this flowpath, and therefore do not have a substantial effect on gas correction functionality.

Table 7-1. Capillary Minor Loss Effects for Nitrogen.

Total Flow (sccm)	*ΔPtotal (Pa)*	*ΔPcontract (Pa)*	*ΔPbend (Pa)*	*ΔPexpand (Pa)*	*ΔPminor Total (Pa)*	*Minor/Total % Effect*
204	5.00	2.03E-06	7.34E-07	4.79E-06	7.56E-06	0.0002
408	10.00	8.15E-06	2.94E-06	1.92E-05	3.03E-05	0.0003
812	20.00	3.26E-05	1.18E-05	7.69E-05	1.21E-04	0.0006
1210	30.00	7.33E-05	2.64E-05	1.73E-04	2.72E-04	0.0009
1604	40.00	1.30E-04	4.69E-05	3.06E-04	4.83E-04	0.0012
1999	50.00	2.03E-04	7.31E-05	4.77E-04	7.53E-04	0.0015

8. CONCLUSION AND RECOMMENDATIONS

The results presented in this thesis indicate that the developed combination of finite element analysis and analytical modeling of the MFM is indeed an effective means of determining gas correction functions throughout the flow range of an MFM. Several considerations have emerged in the course of this study, including the realization that MFM performance, and the resulting gas correction functions, remain particularly sensitive to the geometries of the annular flow bypass. Unfortunately, these exact geometries are difficult to assess without some degree of uncertainty. Indeed, sensitivity of the gas correction function to the outer diameter of the annular flow bypass is great enough to promote significant error in gas flow measurement using modeled gas correction functions based on erroneous dimensional measurements.

This limitation to using modeled data, however, is not a "show stopper". All the gases employed in this thesis were gases which do not present significant hazards to operators or equipment in the calibration process. These gases may be employed, just as nitrogen is employed, to calibrate the MFM. By experimental validation of the performance of the MFM with various gases, the uncertainties of the model, particularly those associated with geometry, may be, to a large extent, corrected out. For example, by calibrating the MFM on nitrogen and on helium, the model may be back corrected and its dimensional variables modified such that the helium gas correction function of the model matches the helium gas correction which is determined experimentally through calibration. The model may then be further verified on other benign gases, such as argon, carbon dioxide, neon, etc., to insure that the model matches other gases of diverse properties as well. The model may then be used with more confidence for other hazardous gases, for which an actual calibration is difficult or impossible to perform.

Towards the understanding of hazardous and toxic gas calibration functions, the methodology employed in this thesis may be extended to further validate the model in the hazardous gas regime. Chapter 6 presented a hazardous gas calibration methodology, the gravimetric calibrator, which may be used to validate process gas correction functions, just as helium and argon were validated for this study. This capability is currently available at the Oak Ridge National Laboratory, and is already being employed successfully for the determination of gas correction functions for such hazardous gases as chlorine, and boron trichloride. Together with an effective model of MFM performance, the procedure developed in this study can contribute to accurate determination of gas correction factors throughout the spectrum of toxic and corrosive process gases. This procedure should thus lead to an overall better understanding of the thermal and hydrodynamics of the MFM and MFC, such that these devices may continue to be modified and improved to address the ever changing needs of the semiconductor community.

REFERENCES

---

[1] SEMATECH, *Mass Flow Control in a Semiconductor Process: 93021493A-TRG*, August 12, 1993.

[2] Gray, D.E., et. al., "Mass-Flow-Controller Real-Time Process-Gas Delivery", *Microelectronics Manufacturing Technology*, August 1991.

[3] Olin, J., President, Sierra Instruments, Personal Communication, March 10, 1996.

[4] Hinkle, L., "MFC Accuracy: Is Simple Gas Correction Enough?", *Semiconductor International*, March, 1991.

[5] Sierra Instruments, Inc., *Instruction Manual 830/840/860 Mass Flow Meters and Controllers*, 1992.

[6] Nelson, D., "Non-Linear Mass Flow Controller Response Phenomenon", *SEMATECH Technology Transfer Document 91100730A-TR*, October 25, 1991.

[7] Hinkle, L. and Mariano, C.F., "Toward Understanding the Fundamental Mechanisms and Properties of the Thermal Mass Flow Controller", *Journal of Vacuum Science and Technology*, May/June 1991.

[8] Bird, Stewart, and Lightfoot, *Transport Phenomena*, New York: John Wiley and Sons, 1960.

[9] Shapiro, A., *The Dynamics and Thermodynamics of Compressible Fluid Flow*, New York: The Ronald Press Company, 1953.

[10] Kays, W.M., *Convective Heat and Mass Transfer*, New York: McGraw Hill, 1966.

[11] Langhaar, H.L., *Journal of Applied Mechanics*, Vol 9, June, 1942.

[12] Trent, D.S., and Eyler, L.L, *Tempest: A Computer Program for Three-Dimensional Time-Dependent Hydrothermal Analysis*, Battelle Memorial Institute, 1991.

[13] Wendel, M., Personal Communication, March 5, 1996.

[14] Structural Research and Analysis Corporation, *COSMOS/M Advanced Modules User Guide*, Version 1.71, 1993.

[15] Quinn, T.J., *Physical Measurements: Temperature*, London: Academic Press, 1990.

[16] Selover, T.B. Jr., et. al, *Thermodynamic Properties of Nitrogen*, Washington: Hemisphere Publishing Corporation, 1987.

[17] Selover, T.B. Jr., et. al., *Thermodynamic Properties of Neon, Argon, Krypton, and Xenon*, Washington: Hemisphere Publishing Corporation, 1987.

[18] Selover, T.B. Jr., *Thermodynamic Properties of Helium*, Washington: Hemisphere Publishing Corporation, 1987.

[19] Baker, A.J., and Pepper, D.W., *Finite Elements 1-2-3*, New York: McGraw-Hill, 1991.

[20] White, F.M., *Fluid Mechanics*, Second Edition, New York: McGraw-Hill, 1986.

[21] Mattingly, G.E., "Gas Flow Measurement: Calibration Facilities and Fluid Metering Traceability at the National Bureau of Standards", *Proceedings Inst. for Gas Technology Conference on Natural Gas Energy Measurement*, Chicago, IL, Apr. 30 - May 2, 1986.

[22] Hylton, J.O., Program Director, Metrology Research and Development Laboratory, The Oak Ridge National Laboratory, Personal Communication, May 15, 1996.

[23] Remenyik, C.J., "An Instrument for Gravimetric Calibration of Flow Devices with Corrosive Gases", *Proceedings of the 41st International Instrumentation Symposium*, Aurora, CO, May 7-11, 1995.

APPENDICES

APPENDIX A - COSMOS/M BATCH FILE CODE FOR ANNULAR BYPASS MODEL.

```
C*
C* COSMOS/M      Geostar V1.75
C* Problem : test1        Date : 3-24-96  Time : 14:51:58
C*
C* FILE,2D.IN,1,1,1,1,
VIEW,0,0,1,0,
PLANE,Z,0,1,
C*
C*
PT,1,0,0,0,
PT,2,.00395,0,0,
PT,3,.00445,0,0,
PT,4,.00585,0,0,
PT,5,.00635,0,0,
PT,6,.01270,0,0,
C*
PT,11,0,.00375,0,
PT,12,.00395,.00375,0,
PT,13,.00445,.00375,0,
PT,14,.00585,.00375,0,
PT,15,.00635,.00375,0,
PT,16,.01270,.00375,0,
c*
PT,21,0,.00425,0,
PT,22,.00395,.00425,0,
PT,23,.00445,.00425,0,
PT,24,.00585,.00425,0,
PT,25,.00635,.00425,0,
PT,26,.01270,.00425,0,
C*
PT,31,0,.03625,0,
PT,32,.00395,.03625,0,
PT,33,.00445,.03625,0,
PT,34,.00585,.03625,0,
PT,35,.00635,.03625,0,
PT,36,.01270,.03625,0,
C*
PT,41,0,.03675,0,
PT,42,.00395,.03675,0,
PT,43,.00445,.03675,0,
PT,44,.00585,.03675,0,
PT,45,.00635,.03675,0,
PT,46,.01270,.03675,0,
C*
PT,51,0,.05116,0,
PT,52,.00395,.05116,0,
PT,53,.00445,.05116,0,
PT,54,.00585,.05116,0,
PT,55,.00635,.05116,0,
```

```
PT,56,.01270,.05116,0,
SCALE,0,
C*
CRLINE,1,1,2,
CRLINE,2,2,3,
CRLINE,3,3,4,
CRLINE,4,4,5,
CRLINE,5,5,6,
CRLINE,11,11,12,
CRLINE,12,12,13,
CRLINE,13,13,14,
CRLINE,14,14,15,
CRLINE,15,15,16,
CRLINE,21,21,22,
CRLINE,22,22,23,
CRLINE,23,23,24,
CRLINE,24,24,25,
CRLINE,25,25,26,
CRLINE,31,31,32,
CRLINE,32,32,33,
CRLINE,33,33,34,
CRLINE,34,34,35,
CRLINE,35,35,36,
CRLINE,41,41,42,
CRLINE,42,42,43,
CRLINE,43,43,44,
CRLINE,44,44,45,
CRLINE,45,45,46,
CRLINE,51,51,52,
CRLINE,52,52,53,
CRLINE,53,53,54,
CRLINE,54,54,55,
CRLINE,55,55,56,
C*
SF2CR,1,1,11,0,
SF2CR,2,2,12,0,
SF2CR,3,3,13,0,
SF2CR,4,4,14,0,
SF2CR,5,5,15,0,
c*
SF2CR,6,11,21,0,
SF2CR,7,12,22,0,
SF2CR,8,13,23,0,
SF2CR,9,14,24,0,
SF2CR,10,15,25,0,
c*
SF2CR,11,21,31,0,
SF2CR,12,22,32,0,
SF2CR,13,23,33,0,
SF2CR,14,24,34,0,
SF2CR,15,25,35,0,
c*
SF2CR,16,31,41,0,
```

```
SF2CR,17,32,42,0,
SF2CR,18,33,43,0,
SF2CR,19,34,44,0,
SF2CR,20,35,45,0,
c*
SF2CR,21,41,51,0,
SF2CR,22,42,52,0,
SF2CR,23,43,53,0,
SF2CR,24,44,54,0,
SF2CR,25,45,55,0,
c*
crcompress;
c*
C* DEFINE 2D FLOW ELEMENT FOR MESHING
EGROUP,1,FLOW2D,1,0,0,0,0,0,0,0,
ACTSET,MP,1,
ACTSET,TP,1,
CURDEF,TEMP,1,1,270,1.25,280,1.20,290,1.16,300,1.12,350,.96,400,.84,450,.75,
MPROP,1,DENS,1,
ACTSET,TP,2,
CURDEF,TEMP,2,1,270,1041,280,1041,290,1041,300,1041,350,1042,400,1045,450,1050,
MPROP,1,C,1,
ACTSET,TP,3,
CURDEF,TEMP,3,1,270,.00001652,280,.00001697,290,.00001742,300,.00001788,350,.0000201
5,400,.00002242,450,.00002469,
MPROP,1,VISC,1,
ACTSET,TP,4,
CURDEF,TEMP,4,1,223.15,.02052,273.15,.02386,293.15,.02554,323.15,.02763,373.15,.03056,4
23.15,.03315,
MPROP,1,KX,1,
ACTSET,TP,5,
CURDEF,TEMP,5,1,270,.004,280,.003,290,.003,300,.003,350,.002,400,.001,450,.001,
MPROP,1,BETA,1,
ACTSET,TP,0,
MPROP,1,GAMMA,1.4,
C*
C* MESH SURFACES
C*
M_SF,2,2,1,4,6,10,1,1,
M_SF,3,3,1,4,10,10,1,1,
M_SF,4,4,1,4,0000016,10,1,1,
M_SF,7,7,1,4,6,6,1,1,
M_SF,8,8,1,4,10,6,1,1,
M_SF,9,9,1,4,0000016,6,1,1,
M_SF,14,14,1,4,0000016,40,1,1,
M_sf,16,16,1,4,20,6,1,1,
M_sf,17,17.1,4,6,6,1,1,
M_sf,18,18,1,4,10,6,1,1,
m_sf,19,19,1,4,0000016,6,1,1,
M_sf,21,21,1,4,20,30,1,1,
M_sf,22,22,1,4,6,30,1,1,
M_sf,23,23,1,4,10,30,1,1,
m_sf,24,24,1,4,0000016,30,1,1,
```

```
C*
ACTSET,MP,2,
PICK_MAT,2,ST_ST,SI,
C* MATL:ST_ST      : STEEL STAINLESS
C* EX      0.20E+12  Pascals
C* NUXY     0.28
C* GXY      0.77E+11  Pascals
C* ALPX     0.11E-04  /Kelvin
C* DENS     0.78E+04  Kgm/m**3
C* KX       18.       W/m/K
C* C (Cp)   0.46E+03  J/kgm/K
M_sf,1,1,1,4,20,10,1,1,
m_sf,6,6,1,4,20,6,1,1,
m_sf,11,11,1,4,20,40,1,1,
m_sf,12,12,1,4,6,40,1,1,
m_sf,13,13,1,4,10,40,1,1,
c*
m_sf,5,5,1,4,5,10,1,1,
m_sf,10,10,1,4,5,6,1,1,
m_sf,15,15,1,4,5,40,1,1,
m_sf,20,20,1,4,5,6,1,1,
m_sf,25,25,1,4,5,30,1,1,
c*
C* OPTIMIZE NODES,ELEMENTS,AND COMPRESS
NCOMPRESS,1,64000,
NMERGE,1,64000,1,.00001,0,0,0,
C*
C* APPLY PRESSURE BOUNDARY CONDITIONS
C*
PCR,2,101010,4,1,101010,2,
PCR,26,101000,29,1,101000,2,
C*
C* APPLY VELOCITY BOUNDARY CONDITIONS
C*
Vsf,1,AL,0,1,1,
vsf,6,al,0,6,1,
vsf,11,al,0,13,1,
vsf,5,al,0,5,1,
vsf,10,al,0,10,1,
vsf,15,al,0,15,1,
vsf,20,al,0,20,1,
vsf,25,al,0,25,1,
c*
c* fluid symmetry
VCR,49,VX,0,49,1,VZ,,
VCR,55,VX,0,55,1,VZ,,
C*
C* APPLY TEMPERATURE BOUNDARY CONDITIONS
C* FLOW INLET AT 293.15 DEG C
C*
NTCR,2,293.15,4;
C*
C* WALLS AT 303.15 DEG C
```

```
C*
ntcr,36,303.15,36;
ntcr,42,303.15,42;
ntcr,48,303.15,48;
ntcr,54,303.15,54;
ntcr,60,303.15,60;
C*
c* temperature symmetry
HXCR,31,0,31,1,
HXCR,37,0,37,1,
HXCR,43,0,43,1,
HXCR,49,0,49,1,
HXCR,55,0,55,1,
C* SET UP SOLUTION CONDITIONS
C*
FL_SOLN,0,0,100,1,1,0.01,
A_FLOW,S,1,0,0,0,0,0,
R_FLOW;
```

APPENDIX B - COSMOS/M BATCH FILE CODE FOR CAPILLARY SENSOR MODEL.

```
VIEW,0,0,1,0,
PLANE,Z,0,1,
pttol,.00001,
C*  Keypoint must be specified
C* UPSTREAM FEEDTHROUGH
PT,1,0,0,0,
PT,2,.000381,0,0,
PT,4,.000425,0,0,
pt,5,.0005,0,0,
PT,6,.00086,0,0,
PT,8,.005,0,0,
C* UPSTREAM TRANSITION
PT,11,0,0.014,0,
PT,12,.000381,0.014,0,
PT,14,.000425,0.014,0,
pt,15,.0005,0.014,0,
PT,16,.00086,0.014,0,
PT,18,.005,0.014,0,
C* UPSTREAM TUBE
PT,21,0,0.019,0,
PT,22,.000381,0.019,0,
PT,24,.000425,0.019,0,
pt,25,.0005,0.019,0,
PT,26,.00086,0.019,0,
PT,28,.005,0.019,0,
C* UPSTREAM SENSOR
PT,31,0,0.0383,0,
PT,32,.000381,0.0383,0,
PT,34,.000425,0.0383,0,
pt,35,.0005,0.0383,0,
PT,36,.00086,0.0383,0,
PT,38,.005,0.0383,0,
C* SENSOR GAP
PT,41,0,0.0459,0,
PT,42,.000381,0.0459,0,
PT,44,.000425,0.0459,0,
pt,45,.0005,0.0459,0,
PT,46,.00086,0.0459,0,
PT,48,.005,0.0459,0,
C* DOWNSTREAM SENSOR
PT,51,0,0.0461,0,
PT,52,.000381,0.0461,0,
PT,54,.000425,0.0461,0,
pt,55,.0005,0.0461,0,
PT,56,.00086,0.0461,0,
PT,58,.005,0.0461,0,
C* DOWNSTREAM TUBE
PT,61,0,0.0537,0,
```

```
PT,62,.000381,0.0537,0,
PT,64,.000425,0.0537,0,
pt,65,.0005,0.0537,0,
PT,66,.00086,0.0537,0,
PT,68,.005,0.0537,0,
C* DOWNSTREAM TRANSITION
PT,71,0,0.07218,0,
PT,72,.000381,0.07218,0,
PT,74,.000425,0.07218,0,
pt,75,.0005,0.07218,0,
PT,76,.00086,0.07218,0,
PT,78,.005,0.07218,0,
C* DOWNSTREAM FEED
PT,81,0,0.07718,0,
PT,82,.000381,0.07718,0,
PT,84,.000425,0.07718,0,
pt,85,.0005,0.07718,0,
PT,86,.00086,0.07718,0,
PT,88,.005,0.07718,0,
C* END
PT,91,0,0.09118,0,
PT,92,.000381,0.09118,0,
PT,94,.000425,0.09118,0,
pt,95,.0005,0.09118,0,
PT,96,.00086,0.09118,0,
PT,98,.005,0.09118,0,
C* CURVE UP FEED
CRLINE,1,1,2,
CRLINE,2,2,4,
crline,3,4,5,
CRLINE,4,5,6,
CRLINE,5,6,8,
C* CURVE UP TRANS
CRLINE,11,11,12,
CRLINE,12,12,14,
CRLINE,13,14,15,
CRLINE,14,15,16,
crline,15,16,18,
C* CURVE UP tube
CRLINE,21,21,22,
CRLINE,22,22,24,
CRLINE,23,24,25,
CRLINE,24,25,26,
crline,25,26,28,
C* CURVE UP SENSOR
CRLINE,31,31,32,
CRLINE,32,32,34,
CRLINE,33,34,35,
CRLINE,34,35,36,
crline,35,36,38,
C* CURVE GAP
CRLINE,41,41,42,
CRLINE,42,42,44,
```

```
CRLINE,43,44,45,
CRLINE,44,45,46,
crline,45,46,48,
C* CURVE DOWN SENSOR
CRLINE,51,51,52,
CRLINE,52,52,54,
CRLINE,53,54,55,
CRLINE,54,55,56,
crline,55,56,58,
C* CURVE DOWN TUBE
CRLINE,61,61,62,
CRLINE,62,62,64,
CRLINE,63,64,65,
CRLINE,64,65,66,
crline,65,66,68,
C* CURVE DOWN TRANS
CRLINE,71,71,72,
CRLINE,72,72,74,
CRLINE,73,74,75,
CRLINE,74,75,76,
crline,75,76,78,
C* CURVE DOWN FEED
CRLINE,81,81,82,
CRLINE,82,82,84,
CRLINE,83,84,85,
CRLINE,84,85,86,
crline,85,86,88,
C* CURVE DOWN END
CRLINE,91,91,92,
CRLINE,92,92,94,
CRLINE,93,94,95,
CRLINE,94,95,96,
crline,95,96,98,
VIEW;
SCALE;
C* UPSTREAM FEED
SF2CR,1,1,11,0,
SF2CR,2,2,12,0,
SF2CR,3,3,13,0,
SF2CR,4,4,14,0,
SF2CR,5,5,15,0,
C* UPSTREAM TRANS
SF2CR,6,11,21,0,
SF2CR,7,12,22,0,
SF2CR,8,13,23,0,
SF2CR,9,14,24,0,
SF2CR,10,15,25,0,
C* UPSTREAM TUBE
SF2CR,11,21,31,0,
SF2CR,12,22,32,0,
SF2CR,13,23,33,0,
SF2CR,14,24,34,0,
SF2CR,15,25,35,0,
```

```
C* UPSTREAM SENSOR
SF2CR,16,31,41,0,
SF2CR,17,32,42,0,
SF2CR,18,33,43,0,
SF2CR,19,34,44,0,
SF2CR,20,35,45,0,
C* SENSOR GAP
SF2CR,21,41,51,0,
SF2CR,22,42,52,0,
SF2CR,23,43,53,0,
SF2CR,24,44,54,0,
SF2CR,25,45,55,0,
C* DOWNSTREAM SENSOR
SF2CR,26,51,61,0,
SF2CR,27,52,62,0,
SF2CR,28,53,63,0,
SF2CR,29,54,64,0,
SF2CR,30,55,65,0,
C* DOWNSTREAM TUBE
SF2CR,31,61,71,0,
SF2CR,32,62,72,0,
SF2CR,33,63,73,0,
SF2CR,34,64,74,0,
SF2CR,35,65,75,0,
C* DOWNSTREAM TRANS
SF2CR,36,71,81,0,
SF2CR,37,72,82,0,
SF2CR,38,73,83,0,
SF2CR,39,74,84,0,
SF2CR,40,75,85,0,
C* DOWNSTREAM FEED
SF2CR,41,81,91,0,
SF2CR,42,82,92,0,
SF2CR,43,83,93,0,
SF2CR,44,84,94,0,
SF2CR,45,85,95,0,
CRCOMPRESS;
C* DEFINE 3D FLOW ELEMENT FOR MESHING
EGROUP,1,FLOW2D,1,0,0,0,0,0,0,0,
ACTSET,MP,1,
ACTSET,TP,1,
CURDEF,TEMP,1,1,270,1.25,280,1.20,290,1.16,300,1.12,350,.96,400,.84,450,.75,
MPROP,1,DENS,1,
ACTSET,TP,2,
CURDEF,TEMP,2,1,270,1041,280,1041,290,1041,300,1041,350,1042,400,1045,450,1050,
MPROP,1,C,1,
ACTSET,TP,3,
CURDEF,TEMP,3,1,270,.00001652,280,.00001697,290,.00001742,300,.00001788,350,.0000201
5,400,.00002242,450,.00002469,
MPROP,1,VISC,1,
ACTSET,TP,4,
CURDEF,TEMP,4,1,223.15,.02052,273.15,.02386,293.15,.02554,323.15,.02763,373.15,.03056,4
23.15,.03315,
```

```
MPROP,1,KX,1,
ACTSET,TP,5,
CURDEF,TEMP,5,1,270,.004,280,.003,290,.003,300,.003,350,.002,400,.001,450,.001,
MPROP,1,BETA,.003,
ACTSET,TP,0,
MPROP,1,GAMMA,1.4,
C* MESH FLUID SURFACES
M_SF,1,1,1,4,0000016,12,1,1,
M_SF,2,2,1,4,6,12,1,1,
m_sf,3,3,1,4,4,12,1,1,
M_SF,4,4,1,4,6,12,1,1,
M_SF,6,6,1,4,0000016,5,1,1,
M_SF,11,11,1,4,000016,12,1,1,
M_SF,16,16,1,4,000016,12,1,1,
M_SF,21,21,1,4,000016,3,1,1,
M_SF,26,26,1,4,000016,12,1,1,
M_SF,31,31,1,4,000016,12,1,1,
M_SF,36,36,1,4,000016,5,1,1,
M_SF,41,41,1,4,000016,12,1,1,
M_SF,42,42,1,4,6,12,1,1,
M_sf,43,43,1,4,4,12,1,1,
M_SF,44,44,1,4,6,12,1,1,
C*EGROUP,2,FLOW2D,1,0,0,0,0,0,0,0,
ACTSET,MP,2,
PICK_MAT,2,ST_ST,SI,
C* MATL:ST_ST       : STEEL STAINLESS
C* EX       0.20E+12  Pascals
C* NUXY     0.28
C* GXY      0.77E+11  Pascals
C* ALPX     0.11E-04  /Kelvin
C* DENS     0.78E+04  Kgm/m**3
C* KX       18.       W/m/K
C* C (Cp)   0.46E+03  J/kgm/K
M_SF,5,5,1,4,6,12,1,1,
M_SF,7,7,1,4,6,5,1,1,
M_SF,8,8,1,4,6,5,1,1,
m_sf,9,9,1,4,4,5,1,1,
M_SF,10,10,1,4,6,5,1,1,
M_SF,12,12,1,4,6,12,1,1,
M_SF,17,17,1,4,6,12,1,1,
m_sf,18,18,1,4,4,12,1,1,
M_SF,22,22,1,4,6,3,1,1,
M_SF,27,27,1,4,6,12,1,1,
m_sf,28,28,1,4,4,12,1,1,
M_SF,32,32,1,4,6,12,1,1,
M_SF,37,37,1,4,6,5,1,1,
M_SF,38,38,1,4,6,5,1,1,
m_sf,39,39,1,4,4,5,1,1,
M_SF,40,40,1,4,6,5,1,1,
M_SF,45,45,1,4,6,12,1,1,
C* DEFINE INSULATION MESHING
C*EGROUP,3,FLOW2D,1,0,0,0,0,0,0,0,
ACTSET,MP,3,
```

```
PICK_MAT,3,AIR,SI,
MPROP,3,KX,.05,
m_sf,13,13,1,4,4,12,1,1,
M_SF,14,15,1,4,6,12,1,1,
M_SF,19,20,1,4,6,12,1,1,
m_sf,23,23,1,4,4,3,1,1,
M_SF,24,25,1,4,6,3,1,1,
M_SF,29,30,1,4,6,12,1,1,
m_sf,33,33,1,4,4,12,1,1,
M_SF,34,35,1,4,6,12,1,1,
C*
C* OPTIMIZE NODES,ELEMENTS,AND COMPRESS
NCOMPRESS,1,64000,
NMERGE,1,64000,1,.000005,0,0,0,
C*
C* APPLY PRESSURE BOUNDARY CONDITIONS
C*
PCR,1,101010,4,1,101010,2,
PCR,46,101000,49,1,101000,2,
C*
C* APPLY VELOCITY BOUNDARY CONDITIONS
C*
C* NON FLUID SURFACES
VSF,5,AL,0,5,1,
VSF,7,AL,0,10,1,
VSF,12,AL,0,15,1,
VSF,17,AL,0,20,1,
VSF,22,AL,0,25,1,
VSF,27,AL,0,30,1,
VSF,32,AL,0,35,1,
VSF,37,AL,0,40,1,
VSF,45,AL,0,45,1,
C*
C* FLUID SYMMETRY
C* FLUID SYMMETRY
VCR,51,VX,0,51,1,VZ,,
VCR,57,VX,0,57,1,VZ,,
VCR,63,VX,0,63,1,VZ,,
VCR,69,VX,0,69,1,VZ,,
VCR,75,VX,0,75,1,VZ,,
VCR,81,VX,0,81,1,VZ,,
VCR,87,VX,0,87,1,VZ,,
VCR,93,VX,0,93,1,VZ,,
VCR,99,VX,0,99,1,VZ,,
C*
C* TEMPERATURE SYMMETRY
HXCR,51,0,51,1,
HXCR,57,0,57,1,
HXCR,63,0,63,1,
HXCR,69,0,69,1,
HXCR,75,0,75,1,
HXCR,81,0,81,1,
HXCR,87,0,87,1,
```

```
HXCR,93,0,93,1,
HXCR,99,0,99,1,
C*
C* APPLY TEMPERATURE BOUNDARY CONDITIONS
C* FLOW INLET AT 293.15 DEG C
C*
NTCR,1,293.15,4;
C*
C* WALLS AT 303.15 DEG C
C*
NTCR,5,303.15,5;
NTCR,56,303.15,56;
NTCR,62,303.15,62;
NTCR,68,303.15,68;
NTCR,74,303.15,74;
NTCR,80,303.15,80;
NTCR,86,303.15,86;
NTCR,92,303.15,92;
NTCR,98,303.15,98;
NTCR,104,303.15,104;
NTCR,50,303.15,50;
C*
C* HEAT GENERATION IN SENSORS
QESF,18,110000000,18,1;
QESF,28,110000000,28,1;
C*
C*
C* SET UP SOLUTION CONDITIONS
C*
FL_SOLN,0,0,100,1,1,0.01,
A_FLOW,S,1,0,0,0,0,0,
R_FLOW;
```

VITA

Timothy Eric McKnight was born in Midland, Michigan on June 22, 1967. His primary education began in the Midland Public School system, to which he is ever grateful for the positive impact that this excellent school system had on his academic career. Undergraduate studies were conducted at the University of Michigan, Ann Arbor, from whence he graduated with a Bachelor of Science Degree in Engineering Science in May of 1989. He then pursued a Masters in Engineering Science from the University of Tennessee, through the Evening School Program.

Mr. McKnight has been involved with the Dow Chemical Company through cooperative educational programs, as a computer programmer and molecular toxicology internist. He is currently working as a staff research engineer at the Oak Ridge National Laboratory. He is facility manager of the SEMATECH/ORNL Mass Flow Controller Development Laboratory, a test facility constructed to promote the development of flow measurement and control in the semiconductor industry. He is also involved in the Laboratory's measurement traceability program, assisting in the engineering support of physical metrology, including the precision measurement of temperature, pressure, moisture, and flow.